

NUREG/CR-2646

SAND82-0765


R7

Printed June 1982

A Model for Boiling and Dryout in Particle Beds

Ronald J. Lipinski

Prepared by
Sandia National Laboratories
Albuquerque, New Mexico 87185 and Livermore, California 94550
for the United States Department of Energy
under Contract DE-AC04-76DF00789



8209210433 820831
PDR NUREG
CR-2646 R PDR

Prepared for

U. S. NUCLEAR REGULATORY COMMISSION

SF29000(18-81)

NOTICE

This report was prepared as an account of work sponsored by an agency of the United States Government. Neither the United States Government nor any agency thereof, or any of their employees, makes any warranty, expressed or implied, or assumes any legal liability or responsibility for any third party's use, or the results of such use, of any information, apparatus product or process disclosed in this report, or represents that its use by such third party would not infringe privately owned rights.

Available from
GPO Sales Program
Division of Technical Information and Document Control
U.S. Nuclear Regulatory Commission
Washington, D.C. 20555

and
National Technical Information Service
Springfield, Virginia 22161

NUREG/CR-2646
SAND82-0765
R-7

A Model for Boiling and Dryout
in Particle Beds*

Ronald J. Lipinski

Date Published:

Sandia National Laboratories
Albuquerque, New Mexico 87185
Operated by
Sandia Corporation
for the
U.S. Department of Energy

Prepared for
Division of Reactor Safety Research
Office of Nuclear Regulatory Research
U.S. Nuclear Regulatory Commission
Washington, D.C. 20555
Under Memorandum of Understanding DOE 40-550-75
NRC Fin. No. A1181

*Work supported by the U.S. Nuclear Regulatory Commission

ABSTRACT

Over the last ten years experiments and modeling of dryout in particle beds have produced over fifty papers. Considering only volume-heated beds, over 250 dryout measurements have been made, and are listed in this work. In addition, fifteen models to predict dryout have been produced and are discussed.

A model is developed in this report for one-dimensional boiling and dryout in a porous medium. It is based on conservation laws for mass, momentum, and energy. The initial coupled differential equations are reduced to a single first-order differential equation with an algebraic equation for the upper boundary condition. The model includes the effects of both laminar and turbulent flow, two-phase friction, and capillary force. The boundary condition at the bed bottom includes the possibility of inflowing liquid and either an adiabatic or a bottom-cooled support structure. The top of the bed may be either channeled or subcooled. In the first case the channel length and the saturation at the base of the channels are predicted. In the latter case, a criterion for penetration of the subcooled zone by channels is obtained.

The model is able to predict saturation (liquid fraction) within the bed (as a function of elevation), and incipient dryout power. It can be applied to either uniform beds or stratified beds, with either large or small particles. The heat flux at dryout in a uniform bed is predicted to increase with increasing particle diameter, with decreasing bed thickness, and with increasing porosity. The dependency on all these parameters changes depending on whether the bed is channeled, moderately deep, or very deep. The dryout fluxes observed in the literature range from channeled to very deep, from laminar to turbulent, and span a factor of 270 in dryout flux. The 260 dryout data points are correlated by the model with an average error of 60 percent.

For powers above incipient dryout, the model predicts a stable dry zone (up to incipient melt) at the base of the bed which increases with increasing power. The dry zone is generally thicker with deeper beds or larger particles.

Downward heat removal by boiling ("downward boiling") is predicted for a bottom-cooled bed. In this process liquid is drawn up into the bed by capillary force, vapor is driven downward by the resulting pressure gradient, and the vapor is condensed at the cooled base of the bed to be recycled upward. The amount of heat removed downward by boiling is predicted as a function of power and bed condition. The process has been observed experimentally and could influence design of core retention devices.

With a permeable support plate, flow entry into the bed bottom is possible. The model predicts significant increases in the dryout flux by this process with moderate increase in the flow resistance through the bed. In addition, the dry zone is predicted to occur at the top of the bed rather than the bottom. In this case the zone is cooled by vapor flow and the temperature in the dry zone is significantly cooler than in a zone without inlet flow at the bed bottom. The pressure gradients predicted by the model agree with experimental data.

With a stratified bed (in which the smallest particles are at the top), the dryout flux is predicted to be lower than with the same bed uniformly mixed. The reason for this is twofold: First, the top layer (where the liquid and vapor flows are largest) contains the smallest particles. Second, capillary force tends to draw the liquid to the region with the smallest particles, which is at the top of the bed. For very deep beds (in which capillary force is negligible) the model predicts that the dryout flux is the same as in a uniform bed composed entirely of the smallest particles.

The model is directly applicable to debris of non-spherical particles and a spectrum of sizes simply by using an effective particle diameter. An explicit formula for such a diameter is given and has been partially verified experimentally. Similar application to damaged pin bundles is also possible, and formulae for effective diameters are suggested.

ACKNOWLEDGEMENTS

The author would like to thank E. D. Gorham-Bergeron and J. E. Kelly for their many helpful comments in reviewing this manuscript, and W. J. Camp, R. L. Coats, and J. V. Walker for their continued support. The author would also like to thank H. Werle and L. Barleon for their many helpful discussions and the opportunity to observe their experiments, from which many important insights were obtained.

TABLE OF CONTENTS

	<u>Page</u>
NOMENCLATURE.....	ix
LIST OF FIGURE CAPTIONS.....	xii
1. INTRODUCTION.....	1
2. PREVIOUS RESEARCH.....	4
2.1 Experimental Research.....	6
2.2 Analytical Research.....	11
2.2.1 Dryout Models.....	11
2.2.2 Channel Length Models.....	24
2.3 Summary of Previous Research.....	25
3. ONE-DIMENSIONAL MODEL DEVELOPMENT.....	30
3.1 Basic Phenomena and Equations.....	30
3.2 Bed Bottom Boundary Condition.....	41
3.3 Bed Top Boundary Condition.....	43
3.3.1 Channel Length Determination.....	43
3.3.2 Channel Suppression in a Subcooled Bed.....	48
3.4 Summary of the One-D Model Basis and Final Equations.....	50
4. MODEL FEATURES FOR A UNIFORM BED ON AN ADIABATIC IMPERMEABLE PLATE.....	55
4.1 Channel Length.....	55
4.2 Liquid Fraction in the Bed.....	58
4.3 Incipient Dryout.....	61
4.3.1 Dryout Flux vs. Particle Diameter....	63
4.3.2 Dryout Flux vs. Bed Thickness.....	74
4.3.3 Dryout Flux vs. Pressure.....	83
4.3.4 Dryout Flux vs. Bed Porosity.....	83
4.3.5 Comparison With Dryout Measurements..	87
4.4 Dry zone Thickness.....	99
4.5 Summary of Model Features for a Uniform Bed on a Plate.....	102

	<u>Page</u>
5. MODEL FEATURES FOR OTHER BED TYPES.....	104
5.1 Very Deep Bed.....	104
5.2 Uniform Bed on a Cooled Plate (Downward Boiling).....	108
5.3 Uniform Bed on a Permeable Support.....	112
5.4 Stratified Bed.....	118
5.5 Uniform Bed With Bottom Heating.....	123
5.6 Non-Spherical Particles and Damaged Pin Bundles.....	123
5.7 Subcooled Sodium-UO ₂ Bed.....	127
5.8 Summary of Model Features for Other Bed Types.....	132
6. ZERO-DIMENSIONAL MODEL.....	135
6.1 Zero-D Model Development.....	135
6.2 Features of the Zero-D Model Compared With the One-D Model.....	140
6.3 Mathematical Relation Between the Zero-D and One-D Models.....	141
6.4 Zero-D Model With Small Particles and Bottom-Cooling (Downward Boiling).....	147
6.5 Summary of the Zero-D Model.....	150
7. SUMMARY.....	151
REFERENCES.....	157
APPENDIX A -- PUBLISHED DRYOUT HEAT FLUX MEASUREMENTS.....	A-1

NOMENCLATURE

c	bed loading (kg/m^2)
$C_{p,l}, C_{p,v}$	specific heat of the coolant liquid or vapor ($\text{J}/\text{kg}\cdot\text{K}$)
d	particle diameter (m)
d_e	effective spherical diameter for a distribution of rough particle sizes (m)
d_m, d_M	minimum or maximum particle diameter in a distribution
f	average error fraction between predicted and measured dryout flux
f_L, f_T	ratio of dryout fluxes predicted by the one-D and zero-D models for dominant capillary force and laminar or turbulent flow
g	gravitational acceleration (m/s^2)
h_{lv}	heat of vaporization (J/kg)
J	Leverett function: dimensionless measure of the capillary pressure as a function of saturation in a bed
k_b	thermal conductivity of a liquid-filled bed ($\text{W}/\text{m}\cdot\text{K}$)
L	total thickness of the bed (m)
L_b	boiling zone thickness in a subcooled bed (m)
L_C, L_{JB}	channel length, characteristic channel length predicted by the Jones-Baker model [31] (m)
L_{up}, L_{down}	thickness of the upward boiling or downward boiling zones in a bottom-cooled bed
N	number of dryout measurements in the data set
P_l, P_v	pressure in the liquid or vapor ($\text{kg}/\text{m}\cdot\text{s}^2$ or Pa)

q	heat flux as a function of elevation in a bed (W/m^2)
q_c	heat flux at the base of a channel
q_d	incipient dryout heat flux: the heat flux at the top of a bed at conditions just sufficient to cause part of the bed to become dry (W/m^2)
q_L, q_T	heat flux at a given elevation in the bed predicted by the present zero-D model in the laminar and turbulent limits (W/m^2)
$q_{L,e}$	laminar heat flux with the Lipinski early zero-D model [27] (W/m^2)
q_o	characteristic heat flux (Equation 6-29) (W/m^2)
q_{up}, q_{down}	upward or downward heat flux at dryout with bottom cooling and downward boiling
q_z	Zuber's critical heat flux for a flat plate (Equation 2-5) (W/m^2)
r	ratio of dryout heat flux in a bed with downward boiling to without
s	effective saturation: liquid fraction at a given elevation in a bed, normalized to the liquid at that level which is easily drained out by gravity (varies from zero to one)
s_t	true saturation: actual liquid fraction at a given elevation in a bed
s_r	residual saturation: liquid fraction left in a bed after draining (Equation 3-3)
s_L, s_T	effective saturation at dryout at the top of the bed for the zero-D model in the laminar or turbulent limit
$s_{L,e}$	effective saturation in the Lipinski early zero-D model [27]

S	volumetric heat source (W/m^3)
T_p, T_s, T_t	temperature of the overlying pool, boiling point, or top of the bed (K)
v_l, v_v	superficial velocity (i.e., average fluid velocity times porosity) of the liquid or vapor (m/s)
w	inlet mass flux at the base of the bed (equal to net mass flux through the bed) ($\text{kg}/\text{m}\cdot\text{s}$)
z	elevation in the bed; zero occurs at the location of zero heat flux
λ	empirical factor in a proposed Leverett function
ϵ	free porosity in a bed (does not include the porous space trapped within individual particles)
θ	contact angle between liquid and solid (zero signifies a wetting condition)
κ	bed permeability (m^2)
κ_l, κ_v	relative permeability for liquid or vapor: dimensionless attenuation factors for permeability which are functions of bed saturation
λ_c	capillary head: distance a liquid will be drawn up into a uniform dry bed (Equations 4-1 and 6-10) (m)
μ_l, μ_v	dynamic viscosity of the liquid or vapor ($\text{kg}/\text{m}\cdot\text{s}$)
ρ_l, ρ_p, ρ_v	density of the liquid, particle, and vapor (kg/m^3)
σ	surface tension (kg/s^2)

LIST OF FIGURE CAPTIONS

<u>Figure</u>		<u>Page</u>
2-1	Boiling and Dryout in a Debris Bed.....	4
3-1	Stylized View of Liquid and Vapor Flow Through a Particle Bed Demonstrating the Influence of Capillary Force. The cir- cles are separated because the vertical cutting plane misses the points of con- tact between the spheres. (The bed is <u>not</u> fluidized.).....	29
3-2	A Typical Example of Relative Permeabil- ities (From Wyckoff and Botset [69]). Solid curves correspond to Equations (3-4) and (3-5). Dotted lines represent linear relative permeabilities.....	31
3-3	Typical Examples of Some Leverett Functions (From Leverett [57,61]). The curve is Equation (3-13).....	37
3-4	Channel Penetrating the Top of a Particle Bed (See also Figure.3-2.).....	43
3-5	Effective Saturation vs. Elevation in a Packed Sodium-UO ₂ Boiling Zone 100-mm Thick With 40% Porosity and 0.3-mm Particle Diameter. The power is 50 W/kg-UO ₂ (0.30 MW/m ³). Saturations of 0.2, 0.4, 0.6, 0.8, and 1.0 at the zone top are considered.....	47
3-6	Pressure in the Vapor, Liquid, and Bed Particles for a 150-mm Thick Subcooled Bed With 67 W/kg-UO ₂ . Zero pressure is at the top of an overlying subcooled zone assumed to be 54-mm thick.....	49
4-1	Channel Length vs. Particle Diameter for a Sodium-UO ₂ Bed 150-mm Thick With 40% Porosity and 330 W/kg-UO ₂ (2.00 MW/m ³)....	53
4-2	Channel Length vs. Power for Previous Bed With 0.3-mm Particle Diameter.....	54

<u>Figure</u>	<u>Page</u>	
4-3a	Effective Saturation vs. Elevation for Various Powers in a Non-Subcooled Sodium-UO ₂ Bed 150-mm Thick With 40% Porosity and 0.3-mm Diameter Particles....	56
4-3b	Effective Saturation in a Bed With 3.0-mm Diameter Particle.....	57
4-4	Predicted and Measured Vapor Fraction....	59
4-5(a-g)	Dryout Flux vs. Particle Diameter for Beds With 40% Porosity and Various Thickness. The beds are (a) sodium-UO ₂ , (b) water-UO ₂ , (c) water-steel, (d) acetone-steel, (e) methanol-steel, (f) freon-113-steel, and (g) isopropanol-steel.....	62-68
4-6(a,b)	Dryout Fluxes for Several Models: (a) as in 4-5a but With a 100-mm Thick Bed, and (b) as in 4-5b but With a 500-mm Thick Bed.....	69,70
4-7	Predicted and Measured Dryout Fluxes for Beds With Bronze Particles and Water, 40% Porosity and 100-mm Thick. Various models and the data of Barleon and Werle [33,52] are shown.....	72
4-8	A Plot Similar to Figure 4-7, but With Freon-113.....	73
4-9(a,b)	Dryout Flux vs. Bed Thickness for Various Models With a Water-Steel Bed With 40% Porosity and 0.68-mm Particle Diameter. The data of several references are shown in 4-9b.....	75,76
4-10	Dryout Flux vs. Bed Thickness for Acetone-Steel Beds Compared With Data.....	77
4-11	Dryout Flux vs. Bed Thickness for Sodium-UO ₂ Beds Compared With the Data of Gabor et al. [3].....	79

<u>Figure</u>		<u>Page</u>
4-12	Dryout Flux vs. Pressure for a 500-mm Thick Water-UO ₂ Bed With 40% Porosity and Various Particle Diameters.....	81
4-13	Dryout Flux vs. Pressure for Various Models With a Water-UO ₂ Bed 500-mm Thick With 40% Porosity and 1-mm Diameter Particles.....	82
4-14	Dryout Flux vs. Porosity for a Water-UO ₂ Bed 500-mm Thick With Various Particle Diameters.....	83
4-15(a-h)	Comparison of Volume-Heated Bed Dryout Data for Single-Sized Spheres With Dryout Models of (a) the Present Work, (b) Sowa et al. [1], (c) Dhir and Catton [5,7] (Combined Deep and "Shallow"), (d) Hardee and Nilson [8], (e) Shires and Stevens [20], (f) Lipinski [27] (Early Zero-D), (g) Jones et al. [29], and (h) Gabor et al. [32].....	85-88
4-16(a-h)	Comparison of Barleon-Werle [33,52] Dryout Data With the Models in Figures 4-15a Through 4-15h.....	91-95
4-17(a,b)	Dry Zone Thickness vs. Power for Sodium-UO ₂ Beds 150-mm Thick With 40% Porosity. Particle diameters are (a) 0.3 mm and (b) 3.0 mm.....	98
5-1	Saturation Profile in a Very Deep Water-Filled Bed 1 Meter Thick With 40% Porosity and 1-mm Diameter Particles. Several powers are considered.....	102
5-2	Downward Boiling in a Bottom-Cooled Bed..	105
5-3	Effective Saturation in a Sodium-UO ₂ Bed 150-mm Thick With 300°C Top Subcooling and a Fixed Downward Flux of 100 kW/M ² . The division between upward and downward boiling is marked by ticks.....	107

<u>Figure</u>		<u>Page</u>
5-4	Situation for Inlet Flow Through a Bed Resting on a Permeable Plate.....	109
5-5	Dryout Power vs. Pressure Drop Across a Bed With Inlet Flow for a Water-UO ₂ Bed 500-mm Thick With 40% Porosity, 1-mm Diameter Particles, and Various Flows.....	111
5-6	Measured Pressure Drop Across a Bed With Inlet Flow Compared With the Model.....	113
5-7	Saturation vs. Elevation in a Stra- tified Bed of Constant 40% Porosity and Four 25-mm Layers of Particle Diameters 0.86, 0.61, 0.45, and 0.26 mm (Bottom to Top).....	115
5-8	Dryout Flux vs. Average Particle Size in a Stratified Bed and Corresponding Mixed Bed of Sodium and UO ₂ , 100-mm Thick With 40% Porosity.....	118
5-9	Dryout Model Predictions and Data for Subcooled Sodium-UO ₂ Data.....	127
6-1	Dryout Flux vs. Particle Diameter for Water-UO ₂ Beds With 40% Porosity and Various Thicknesses as Predicted by the One-D and Zero-D Models.....	141

1. INTRODUCTION

In the event of a severe accident in a nuclear reactor, restructuring of the core geometry may occur, leading to increased flow resistance in the core. In a severe case melting may occur and molten core materials may contact the coolant resulting in rapid quenching, freezing, and fragmentation of the core debris. Particulated fuel and steel may subsequently settle on available surfaces within the reactor vessel, forming debris beds. The fuel in these debris beds will be heated by radioactive decay of retained fission products and actinides. The hazard level which should be assigned to the resulting post-accident condition depends on the extent to which natural cooling of the debris may be relied upon.

The cooling of a degraded core or debris bed may proceed by conduction, single-phase convection, boiling, or radiation. With serious core degradation, conduction and single-phase convection (by natural circulation only) may be inadequate to remove the decay heat from the debris. In such a case, boiling of the coolant will occur. As long as boiling is adequate to remove the heat from all portions of the debris, the temperature in the debris will remain at or below the boiling point of the coolant. At such low temperatures there is no thermal attack on supporting structures. With water-cooled reactors there is also no hydrogen generation from metal oxidation (either in-vessel or ex-vessel), no hydrogen generation and breakup in the concrete below the debris bed, and no debris melting. However, these benign conditions are not maintained if boiling is inadequate to remove the decay heat.

If the decay power level is large enough to evaporate all the liquid flowing into the bed before it reaches all parts of the debris, local dryout of the debris will occur. For debris resting on a blockage or a plate, the liquid must enter the bed from an overlying pool against the upward-flowing vapor and dryout can occur readily. Heat removal from the dry portion of a debris bed is much reduced relative to the boiling zone. The primary modes are by conduction, radiation, and convection by vapor. Because of the low thermal conductivity of dry debris, the low efficiency of radiation at low temperatures and the low vapor flow rates expected, high temperature

gradients can be achieved over small distances. Thus dryout marks a sharp change in the coolability of debris and indicates the potential for failure of containment boundaries.

This report contains the development of a new model to describe boiling and dryout in particle beds as well as a description of the predictions of the model in various circumstances, comparison with published data, and a review of all recent work in the field. Because the report is lengthy, it is recommended that the summary (Chapter 7) be read first so that an overview of the report can be obtained. The Table of Contents may then be used to direct readers to areas of particular interest for more detail.

The importance of boiling in particle beds to the safety assessment of nuclear reactors is first briefly described. Previous experimental and analytical work is presented. The full model is then developed. Because of the generality and complexity of the model equation, the features of the model in various limiting cases are explored. The model predictions are then compared with published measurements and observations. In addition, a simpler form of the model is derived which gives very similar predictions (with some loss of detailed information) as the full model. This simpler model is much easier and faster to use. Finally, a summary of the report is made.

2. PREVIOUS RESEARCH

Figure 2-1 depicts boiling and dryout in a volume-heated particle bed. Heat is removed from the bed solely by vaporization of the coolant (i.e., the coolant is initially at the boiling point). Thus, the vapor flows upward out of the bed while the liquid flows downward into the bed. The vapor is driven from the bed by the pressure developed as it boils. The liquid is pulled into the bed both by gravity and by capillary force. If these two forces are sufficient to overcome the pressure developed in the vapor, steady state boiling can occur throughout the bed. However, for high bed powers, the pressure developed by the vapor retards the inflowing liquid enough so that all of the liquid vaporizes before it reaches the bed bottom. In such a case (as shown in the figure), the bottom of the bed becomes dry. The bed power at which some part of the bed just becomes dry is called the "incipient dryout power" (or just "dryout power").

The heat generated in the dry zone may be removed by conduction and radiation to the overlying boiling zone. Because of the low conductivity of dry debris, very high temperatures can be achieved even with thin dry zones. These high temperatures may attack support structures or containment boundaries, or may allow debris melting and reconfiguration. Thus, incipient dryout marks one limit in the coolability of debris. For this reason the onset of dryout is of interest.

Bed characteristics which can affect the dryout power include particle diameter, bed thickness, and bed porosity, as well as fluid material properties. The particle diameter influences the fluid flow regime (laminar vs. turbulent) as well as the flow amount. In addition, the particles may be a mixture of sizes either uniformly mixed or stratified so that the particle diameter is a function of elevation in the bed. Another important influence on dryout is channeling at the top of the bed. In a channel the particles are pushed aside by the vapor. This leaves a low-resistance vapor path several particle diameters across. These low-resistance paths allow a higher dryout flux.

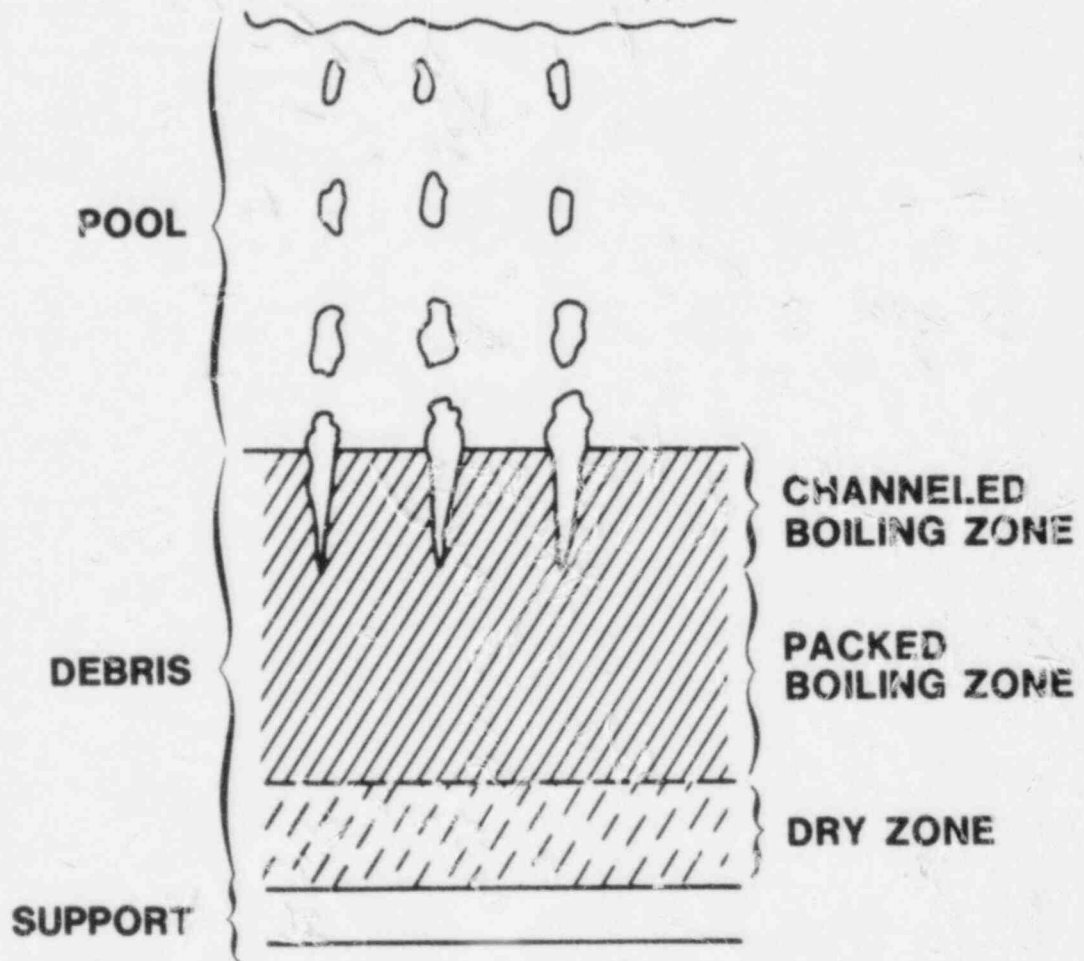


Figure 2-1. Boiling Dryout in a Debris Bed

Considerable research has been performed investigating the boiling and dryout behavior of particle beds [1-54]. Most of the research has involved particle beds resting on an adiabatic impermeable support plate and cooled only by natural circulation from an overlying pool at the boiling temperature. These conditions are usually conservative in that the bed requires less heat to dry out than with subcooling at the bed top or bottom. In addition, these conditions are phenomenologically the simplest to analyze. In this chapter, the previous research into bed behavior will be presented. The research will be divided into two sections (experimental and analytical), and each section will be presented chronologically.

2.1 Experimental Research

Sowa, Hesson, Gebner, and Goldfuss [1] performed some of the earliest research in the field. They used sodium-filled UO_2 beds with bottom heating but did not achieve dryout. They also noted a large porosity in beds of fine particles (0.025-0.100 mm). Gabor, Hesson, Baker, and Cassulo [2] used water- UO_2 beds with heat generation in the water. The water had an electrolyte dissolved in it and was heated by electrical current. They were the first to note channels at the top of the bed and observed a decrease in dryout flux as the bed thickness increased. They attributed this effect to the limited depth of the channels. They also noted that the dryout flux for bottom-heated beds was less than in volume-heated beds.

Gabor, Sowa, Baker, and Cassulo [3] continued the investigation of bottom-heated dryout in UO_2 particle beds with water and with sodium. Additional studies of sodium- UO_2 beds with electrically-heated sodium were made to simulate the volume-heating of decay heat. The UO_2 particles were nominally 0.1 mm to 1.0 mm in diameter and well mixed in the bed. When very fine particles were added to the size distribution, the total power from the system at dryout increased slightly. This suggests the fines were removed from the bed into the overlying pool where the heat from them could be removed independently of the heat in the bed. When subcooled sodium was used in the overlying pool (with bottom-heating in the bed) no major effect on dryout was noted relative to non-subcooled sodium.

Keowin [4] studied inductively-heated steel beds and lead beds in water and characterized the bed as fluidized. Dhir and Catton [5,7] used inductive heating with steel beds and lead beds in water, acetone, and methanol. They noted that the dryout heat flux was independent of bed thickness in deep beds (greater than about 50 mm, depending on the fluid). They again characterized the top channeled section of the bed as fluidized. (This characterization was subsequently questioned [16,26].)

Sowa, Gabor, Baker, Pavlick, Cassulo, and Holloway [6] reported on steel beds in water with inductive-heating in the particles, direct electrical (Joule) heating in the liquid, and bottom-heating. They noted similar dryout fluxes with liquid-heating and particle-heating in deep beds only.

Hardee and Nilson [8] studied convection and boiling (but not dryout) in sand beds in microwave-heated water. The overlying water pool was subcooled and only minor effects of subcooling were noted. They suggested that subcooling the overlying pool would increase the dryout flux by the ratio of the sensible heat of the subcooling to the latent heat of vaporization.

Rivard [9,10,12] studied dryout in fission-heated UO_2 beds in sodium with subcooled overlying pools. The heating of the particles by fission was more prototypic of decay heat than the liquid heating by Gabor et al. [3], and the beds were better instrumented. Rivard noted that boiling in the subcooled sodium-filled bed was restricted to a zone in the bottom portion of the bed. The top fraction of the bed remained subcooled. During the course of the experiment a disturbance occurred in which a large vapor flow in the bed occurred suddenly. Following the disturbance and a simultaneous reduction in subcooling, the bed dryout flux was increased by over 50 percent. (Actual dryout was not achieved due to power limitations.) Rivard was the first to note stable steady-state dry zones at powers slightly above those required to initiate dryout. The dry zones occurred at the bed bottom, were fairly thin (several millimeters) and increased in thickness as the power increased. This led to the possibility that a significant power above the incipient dryout power would be required to achieve bed melting.

Dhir [17] investigated dryout in beds with particle size distributions. LeRigoleur [11] had proposed using a formula to determine an effective particle diameter for a distribution of particles sizes. This formula had been

studied by Fair and Hatch with respect to permeability of soils. The effective diameter is

$$d_e = f_s \left(\sum_i \frac{w_i}{d_i} \right)^{-1} \quad (2-1)$$

where w_i is the weight fraction of particles with sieve diameter d_i , and f_s is a shape factor which is 1 for spheres and 0.78 for rough particles. Dhir found that the effect of changing particle size distribution agreed with the Fair-Hatch formula, with the caveat that particles smaller than 0.1 mm diameter be neglected. This caveat agreed with earlier observations by Gabor, Sowa, Baker, and Cassulo [3].

Dhir and Catton [19] studied heat removal from steel particles in acetone with both a subcooled overlying pool and with a subcooled base. They noted only a minor influence of subcooling the pool, about the amount suggested by Hardee and Nilson [8]. They interpreted the downward heat removal to be by conduction only (as proposed earlier by Rivard [12]).

Squarer and Peoples [21] studied dryout in inductively-heated beds with forced inlet flow (at the bed bottom through a porous support). Inlet flow considerably increased the dryout flux. Unfortunately they did not measure the corresponding increase in pressure drop through the bed, so the change in dryout flux could not be related to natural circulation loops in a reactor with a known driving head. Naik, Le, and Dhir [22] also studied boiling in a bed with inlet flow. They measured the pressure drop across the bed as a function of exit quality for various inlet flow rates, but did not report dryout powers.

Squarer and Peoples [21] also studied dryout in beds of different diameters. They initially reported that the dryout flux decreased with increasing bed diameter. However, later studies [34] showed that this conclusion was due to calibration errors and that no dependence of dryout flux on bed diameter had been observed.

Barleon and Werle [23] were the first to study dryout with particles larger than one millimeter in diameter (with inductive heating). The dryout fluxes they obtained were much smaller than predicted by most models. This was the first data to indicate that the dryout flux does not depend strongly on particle diameter with large particles.

Trenberth and Stevens [24] heated their beds by passing an alternating current through the touching particles. They observed decreasing dryout flux with bed thickness (as first noted by Gabor et al. [2]) and related it to the influence of capillary force (as suggested by a model by Shires and Stevens [20]). In addition, they noted that the dry zone first occurred at an elevation in the bed which, while subject to much scatter, generally increased as the bed thickness increased. This is in contrast to the dry zones observed by Rivard [9,12] which occurred only at the bed bottom.

Gabor, Epstein, Jones, and Cassulo [26,29] studied both bottom-heated and inductively-heated beds involving copper and steel particles with water, acetone, methanol, isopropanol, and freon-113. They noted that the dryout flux from a volume-heated bed was generally two or three times that from a similiar bottom-heated bed.

Dhir and Catton [27] studied the dryout flux in in "very deep" acetone-steel beds and noted no change in the dryout flux in beds from 50-mm to 400-mm thick.

Gronager, Schwarz, and Lipinski [30,54] continued the study of heat removal in subcooled sodium-UO₂ beds begun by Rivard [9,10,12]. They observed the same bed disturbances noted by Rivard in which a large flow of sodium vapor was noted. They interpreted the disturbance to be caused by the flashing of superheated liquid sodium. The flashing did not occur on the first heating and boiling cycle due to the presence of trapped gas in the bed. However, flashing did occur on all subsequent initiations of boiling. This raises the question of whether flashing will occur in bed produced during an accident in an sodium-cooled reactor. The authors also noted a large increase in dryout power (by a factor of 4.5) following the flashing and a reduction in subcooling. Contrary to Rivard's interpretation that the increase was due to the disturbance, the authors concluded that the increase was

primarily due to the reduction in subcooling. Analysis showed that with large subcooling the dryout flux in the boiling zone agreed with packed bed models. But with small subcooling the dryout flux agreed with channeled-bed data by Gabor et al. [3]. The interpretation was that the thick subcooled zone induced by large subcooling suppressed the channel formation normally expected at the top of the bed and greatly reduced the dryout flux expected in a bed as shallow (83 mm) as the one used. (Earlier bottom-heated subcooled experiments reported by Gabor et al. [3] did not reveal this effect of subcooling.) This led to the possibility that previous sodium-UO₂ dryout correlations [3] might be greatly non-conservative for shallow subcooled beds.

Jones and Baker [31] and Gabor and Cassulo [32] continued the study of Gabor, Epstein, Jones, and Cassulo [26] using water, acetone, methanol, isopropanol, and freon-113 with deeper beds and different bed diameters. They found that the dryout flux is independent of bed diameter, confirming the corrected work of Squarer and Peoples [21]. They noted that the dryout flux from a volume-heated bed is about twice that from a bottom-heated bed. Subcooled tests with the low thermal conductivity fluids used did not reveal the channel suppression noted by Gronager, Schwarz, and Lipinski [30] with sodium. Reduction in dryout flux with increasing bed thickness was observed with water-copper beds up to 250-mm thick.

Barleon and Werle [33,45] extended their earlier work [23] on beds with large particles and noted that the dryout flux varied with the square root of particle diameter. (Squarer, Pieczynski, and Hochreiter [37] also reported the same effect.) Their data also demonstrated that the dryout flux from a volume-heated particle bed could exceed the critical heat flux for a bottom-heated flat plate (by as much as a factor of five).

Naik and Dhir [39] reported more measurements of the pressure drop across beds with boiling and forced inlet flow. They expressed their results in terms of the quality of the exit vapor. Somerton, Catton, and Thompson [44] reported on deep bed dryout and noted that the thickness of the overlying pool can have an effect on the dryout power.

Mitchell, Lipinski, and Schwarz [47,51] were the first to study the dryout flux in a stratified bed in which the particle size decreased monotonically with

elevation. The bed was a subcooled sodium-UO₂ bed. A substantial decrease in the dryout flux was noted compared with a similar bed which was uniformly mixed (studied by Rivard [12]). The reasons for the decrease were threefold. First, stratification reduced the amount of single-phase convection, thus decreasing the benefits of subcooling. Second, stratification decreased the efficiency of heat removal in the boiling zone (as will be described in Section 5.4 of this report). Third, because of the low dryout powers induced by the first two items, channel penetration of the subcooled zone required very small subcoolings and thus the bed remained packed. These results indicate that correlations based on uniform beds are non-conservative with respect to stratified beds.

2.2 Analytical Research

Concurrent with the experimental research, efforts have been made to model the behavior of boiling in particle beds. Most of the models have attempted to predict the heat flux from the bed at the power just sufficient to cause dryout somewhere in the bed. (Rivard [12] called this the "incipient" dryout heat flux.) Recently, models to predict the length of channels at the top of a bed have been developed. Again, the research in each section will be presented chronologically.

2.2.1 Dryout Models

Sowa, Hesson, Gebner, and Goldfuss [1] presented the first dryout model in the field. It was based on a flooding correlation from the chemical industry by Sherwood, Shipley, and Holloway [56]. The flooding correlation was based primarily on large particles (about 10-mm diameter) and thus was not very applicable to their data (with 0.025 to 1-mm diameter particles). The model was forgotten for nearly a decade, and then rederived in several forms. The predicted "incipient" dryout flux is

$$q_d = 0.463 h_{1v} \left[\frac{\rho_v \rho_l g d \epsilon^3 f}{(1 - \epsilon)} \right]^{1/2} \left(\frac{\mu_w}{\mu_l} \right)^{0.1} \quad (2-1)$$

where h_{1v} is heat of vaporization, ρ_v is vapor density, ρ_l is liquid density, g is gravitational acceleration, d is particle diameter, ϵ is bed porosity (or coolant fraction in the bed), μ_w is the dynamic viscosity for saturated liquid water at one atmosphere pressure, and μ_l is dynamic viscosity of the liquid coolant.

The parameter f is a function of the density ratio of the coolant liquid and vapor phases and is given in graphical form in Reference 56. A fairly good fit of the curve in the region of relevance ($\rho_v < \rho_l$) is

$$f = 0.03(\rho_l/\rho_v)^{1/4} \quad (2-2)$$

and this relation will be used in this paper. With this relation, Equation (2-1) becomes

$$q_d = .0802 h_{1v} \left[\frac{\rho_v \rho_l g d \epsilon^3}{(1 - \epsilon)(\rho_v/\rho_l)^{1/4}} \right]^{1/2} \left(\frac{\mu_w}{\mu_l} \right)^{0.1} \quad (2-3)$$

Equation (2-1) indicates that the dryout flux increases with the square root of particle diameter and is independent of the bed thickness. It should also increase appreciably with pressure since the vapor density increases with pressure. The influence of viscosity is very small.

Gabor, Sowa, Baker, and Cassulo [3] correlated their dryout data for sodium-UO₂ beds in terms of bed loading (mass per unit area). In SI units their correlation (without the 10 percent reduction they inserted for conservatism) is

$$q_d = 1,050,000 \quad \text{for } c < 433 \quad (2-4)$$

$$q_d = 3,460,000 - 7310 c + 4.02 c^2 \quad \text{for } c > 433 \quad (2-5)$$

where q_d is the dryout heat flux in W/m² and c is the bed loading in kg/m². This equation is valid only for non-subcooled sodium-UO₂ beds with the same particle size

distribution (0.1 mm to 1.0 mm) and bed porosity (about 50 to 55 percent) as used in their experiment. Thus it is not a very general expression. But it is very dependent on loading (or bed thickness), in contrast to Equation (2-1).

Dhir and Catton [5] developed a model based on their dryout experiments. For packed beds they considered resistance to liquid flow based on Darcy's law and Kozeny's [57] permeability. They obtained an expression for dryout based on an empirical constant fit to their deep-bed data. The expression fit their deep-bed data well. The model was published in terms of dimensionless groupings, but is presented here in terms of physical properties for greater clarity:

$$q_d = \frac{0.0177 \rho_l (\rho_l - \rho_v) g d^2 \epsilon^3 h_{lv}}{180 (1 - \epsilon)^2 \mu_l} \quad (2-6)$$

The heat flux varies with the square of diameter, in contrast with the square root dependence in Equation (2-1). In addition, little pressure dependence is predicted because of the lack of dependence on vapor density. The dryout flux is independent of bed thickness, as the authors noted experimentally for deep beds.

Dhir and Catton also developed a dryout model for channeled beds (which they called shallow beds). The model assumed that dryout was caused by Helmholtz instabilities in the vapor jets leaving the bed and entering the overlying pool. However, this condition depends only on the heat flux at the top of the bed and not the bed thickness. Thus, it by itself does not predict the strong dependence of heat flux on bed thickness which is so characteristic of channeled beds. Therefore additional phenomena were needed to explain bed thickness effects. Dhir and Catton assumed that channeled beds were fluidized, based on observations by themselves and by Keowin [4]. With this assumption and an additional remark that fluidized beds maintained a maximum potential energy ("consistent with the minimum irreversibility principle" [5,7]), a correlation for the dryout flux as a linear function of the bed thickness was obtained. It used two empirical constants fit to their channeled (shallow) bed data:

$$q_d = 1.84 \left(1 - \frac{0.092 (1 - \epsilon)L}{\sqrt{\sigma / ((\rho_l - \rho_v)g)}} \right) q_z \quad (2-7)$$

where L is the bed thickness, σ is surface tension and q_z is Zuber's critical heat flux for a flat plate [58]:

$$q_z = \frac{\pi}{24} h_{lv} (\rho_v^2 (\rho_l - \rho_v)g\sigma)^{1/4} \quad (2-8)$$

The model fits their shallow-bed data well. The two equations (2-6 and 2-7) apply to the full range of bed depths if the larger heat flux is taken for the dryout flux.

The claim that the channeled region of a bed is fluidized has caused some controversy. In their descriptive figure [5,7], Dhir and Catton show all of the particles in the channeled region of a bed subjected to downward flowing liquid, with all of the vapor in the channels. Lipinski and Rivard [16] questioned how particles subjected to only downward flowing liquid could fluidize. Even with vapor flowing between the particles instead of isolated in the channels Lipinski and Rivard doubt that shallow beds are fluidized. They develop conservation equations which yield a fluidization criterion and conclude that fluidization will not occur in UO_2 or steel beds with boiling sodium or water resting on impermeable plates [16]. Cho [34] later makes a similar conclusion. The fluidization question is important to the Dhir-Catton shallow bed model since the bed thickness dependence of the heat flux depends on the fluidization assumption.

Hardee and Nilson [8] developed a model based on conservation laws for mass, momentum, and energy. They considered the combined resistances of liquid and vapor flow, and developed a dryout criterion by maximizing the bed heat flux as a function of liquid fraction. Thus they required no empirical constant fit to dryout data. In addition, they assumed that the effect of subcooling could be accounted for by the amount of energy required to heat the subcooled liquid to the boiling point. Their criterion for dryout is

$$q_d = \frac{\rho_l g d^2 \epsilon^3 h_{lv} (1 + C_{p,l} \Delta T/h_{lv})}{180(1 - \epsilon)^2 (\sqrt{\mu_v/\rho_v} + \sqrt{\mu_l/\rho_l})^2} \quad (2-9)$$

where ν is the vapor viscosity, $C_{p,l}$ is the liquid specific heat, T is the subcooling, and the 180 comes from the Kozeny-Carman permeability [55]. The equation is similar to equation (2-6). However, it predicts a stronger pressure dependence due to the dominant role of vapor density in the equation. The dependence of dryout flux on pressure has not yet been well tested for deep beds. (However, Dhir and Catton [17] studied the effect in shallow beds about 50 mm thick and found very little pressure dependence.)

Rivard [9,12,16] noted that the Hardee-Nilson relation for the effect of subcooling was not appropriate with sodium and proposed the series conduction model. In that model the boiling in the bed takes place below a subcooled layer in the bed. The heat generated in the subcooled zone is removed in series with the heat generated in the boiling zone. This implies that the vapor produced by boiling is all condensed at the base of the subcooled zone. The length of the boiling zone determined by Rivard from the heat conduction equation is

$$L_b = \sqrt{L^2 - 2k_b(T_s - T_t)/S} \quad (2-10)$$

where L is the total bed thickness, k_b is the bed thermal conductivity, T_t is the temperature at the top of the bed, and S is the volumetric power in the bed. Rivard suggested that the temperature difference between the bed top and the bulk sodium may be determined by the McDonald-Connolly relation [59]. For sodium near saturation and beds near 100 mm in diameter, this becomes

$$T_t - T_p = \left(\frac{q}{2400} \right)^{0.758} \quad (2-11)$$

where T_p is the temperature of the overlying pool, q is the bed heat flux in W/m^2 and temperatures are in Kelvin or Centigrade. The dryout models developed for non-subcooled beds could then be applied to the boiling zone rather than the entire bed.

Ostensen [13] (also reported in [25]) developed a dryout model (unaware of the model by Sowa, et al.) based on the flooding correlation of Wallis [57] fit to the data of Sherwood, et al. [56]. The original derivation was missing a factor of ϵ due to a misinterpretation of one of Wallis' terms. The final model equation (as corrected in a subsequent publication [41]) is

$$q_d = 0.245 h_{lv} \left[\frac{\rho_v \rho_l g d \epsilon^3}{(1 - \epsilon)(1 + (\rho_v / \rho_l)^{1/4})^4} \right]^{1/2} \quad (2-12)$$

(The curve from the erroneous equation was unfortunately used in references 27 and 33. The correct curve would be lower.)

This model is similar to the flooding model of Sowa, et al. [1] (equation 2-1)). The dependence on the density ratio is different because Wallis used different dimensional groups in fitting the flooding data of Sherwood, et al. [56]. The flooding models are different from the Dhir-Catton and Hardee-Nilson models in that they predict that the dryout flux depends on the square root of particle diameter (instead of the square) and on approximately the square of porosity (instead of approximately fifth power). Since flooding correlations are based on data with very large particles and turbulent flow, the flooding dryout models should also apply to those regimes. The models predict a much lower dryout flux for large particles than laminar-flow models. In addition, they probably are more appropriate for bottom-heated beds since flooding experiments involve bottom-injected gases. Squarer [48] later rederived the Ostensen model and concluded that Equation (2-13) would agree better with the volume-heated data of Squarer, Pieczynski, and Hochreiter [37] if the empirical constant were 0.342 instead of 0.245.

Lipinski and Rivard [16] extended the Hardee-Nilson model to one dimension and found that the dryout flux was unchanged by this process. The one-D model predicted that the dryout flux in a very deep stratified bed would be determined by the particle diameter and porosity in the top layers of the bed. (Physically, this is because both the liquid flow and vapor flow are largest there.) The authors also developed the first (very crude) model to predict the dry zone thickness for powers above the

incipient dryout power. The model was based on the channeled bed dryout correlation of Gabor, Sowa, Baker, and Cassulo [3] for volume-heated and bottom-heated beds. The model assumed that the boiling zone above the dry zone could be treated as a cross between a volume-heated and bottom-heated bed at incipient dryout. Complete bed dryout was predicted for deep beds.

Shires and Stevens [20] extended the Hardee-Nilson model to include the effect of capillary force:

$$q_d = \frac{C \rho_l g d^2 \epsilon^3 \rho_v h_{lv}}{180 (1 - \epsilon)^2 \mu_v} \left(1 + \frac{4.29 \sigma (1 - \epsilon)}{\epsilon d \rho_l g L} \right) \quad (2-13)$$

Both C and 4.29 are empirical constants; C has not yet been chosen, but C = 0.211 fits the experimental data of Trenberth and Stevens [24] well, and will be used throughout this report.

The addition of capillary force by Shires and Stevens to the modeling of Hardee and Nilson was an extremely important step. For most beds of interest to LMFBR research, capillary force is predicted by the model to be two to ten times stronger than gravity and thus increases the dryout flux by three to eleven times. Without capillary force the Hardee-Nilson model, which is phenomenologically based and contains no empirical constants fit to dryout data, predicts dryout fluxes an order of magnitude too low. With capillary force the predicted fluxes are about right, indicating that a solid understanding of dryout is much nearer than before.

Lipinski [25,27] extended the modeling of Hardee and Nilson [8] and of Shires and Stevens [20] by explicitly combining the effects of laminar and turbulent flow, assuming a capillary force without an empirical constant, and refining the two-phase friction factor ("relative permeability" [57]). Much of the derivation and many consequences of this model will be presented more fully in this report (in Chapter 6) since Reference 27 is only a brief summary. Some improvements will be made. The dryout criterion may be rearranged algebraically to

$$q = \left(\frac{q_T^4}{4q_{L,e}} + q_T^2 \right)^{1/2} - \frac{q_T^2}{2q_{L,e}} \quad (2-14)$$

where

$$q_{L,e} = \frac{\frac{(\rho_1 - \rho_v) g d^2 \epsilon^3 h_{1v}}{180 (1 - \epsilon)^2} \left(1 + \frac{6 \sigma (1 - \epsilon)}{\epsilon d (\rho_1 - \rho_v) g L} \right)}{\left(\frac{\mu_v}{\rho_v (1 - 1.11 s)} + \frac{\mu_1}{\rho_1 s^3} \right)} \quad (2-15)$$

and

$$q_T = \left[\frac{\frac{(\rho_1 - \rho_v) g d \epsilon^3 h_{1v}^2}{1.75 (1 - \epsilon)} \left(1 + \frac{6 \sigma (1 - \epsilon)}{\epsilon d (\rho_1 - \rho_v) g L} \right)^{1/2}}{\left(\frac{1}{\rho_v (1 - s)^3} + \frac{1}{\rho_1 s^3} \right)} \right]^{1/2} \quad (2-16)$$

and where s is the effective saturation (or liquid fraction between the particles) at dryout. The dryout flux is determined by maximizing q in Equation (2-14) as s is varied between

$$S_{L,e} = \left(0.833 \frac{\mu_1 \rho_v}{\mu_v \rho_1} + \left(2.70 \frac{\mu_1 \rho_v}{\mu_v \rho_1} \right)^{1/2} \right)^{1/2} - \left(0.833 \frac{\mu_1 \rho_v}{\mu_v \rho_1} \right)^{1/2} \quad (2-17)$$

and

$$s_T = \left(1 + (\rho_l / \rho_v)^{1/4} \right)^{-1} \quad (2-18)$$

Although somewhat cumbersome, the equations are algebraic and easily solved.

In the laminar (small-particle) limit, Equation (2-14) reduces to Equation (2-15) with s defined by Equation (2-17). The laminar limit is somewhat similar to the Shires-Stevens model except for their empirical constants, dependence on viscosity, and lack of dependence on vapor density. In the turbulent (large-particle) limit without capillary force, Equation (2-14) reduces to Equation (2-16) with s defined by Equation (2-18). This in turn reduces to

$$q_d = 0.756 h_{1v} \left[\frac{\rho_v (\rho_l - \rho_v) g d \epsilon^3}{(1 - \epsilon) (1 + (\rho_v / \rho_l)^{1/4})^4} \right]^{1/2} \quad (2-19)$$

The turbulent limit is almost exactly the same as the Ostensen model, except for a constant factor. This similarity is interesting considering that the Ostensen model is based on flooding correlations and the Lipinski model is based on solution of four conservation equations with a variational maximizing of the heat flux.

Equation (2-14) indicates that the dependence of the heat flux on particle diameter changes from square to square root near one millimeter, which is near the diameter used by early experiments for which the laminar-flow models were developed.

A novel feature of debris cooling raised by Lipinski [27] is the possibility of downward streaming vapor in bottom-cooled beds. The vapor would condense on the cooled support plate and the liquid would be drawn back up into the bed by capillary force. This proposed cyclic process would thus deliver heat flow downward via boiling and was called "downward boiling." The process could enhance the total heat removal from a bed and could impact the design of core retention devices.

Jones, Epstein, Gabor, Cassulo, and Bankoff [26,29] developed a model to include the shear between the liquid and the vapor, but did not include the effects of turbulent flow or capillary force. The model was specified for bottom-heated (rather than volume-heated) beds:

$$q_d = \frac{(\rho_l - \rho_v) g d^2 \epsilon^3 h_{lv}}{150 (1 - \epsilon)^2} \left(\frac{\mu_v}{\rho_v s^2 (1 - s)} + \frac{\mu_l}{\rho_l (1 - s)^3} \right)^{-1} \quad (2-20)$$

where s is determined by

$$2 - 7s + 8s^2 - 3 \left(1 + \frac{\mu_l \rho_v}{\mu_v \rho_l} \right) s^3 = 0 \quad (2-21)$$

The equation is essentially the same as the Hardee-Nilson model [8] except for the different dependence on the ratio of kinematic viscosities. The proper choice of the viscosity dependence is important to make a model applicable to all fluids, as will be shown in Section 4.3.5.

Gabor and Cassulo [32,46] produced a dryout model based on bubble release from the narrowest point between adjacent particles. They derived slightly different models for the dryout flux in volume-heated and bottom-heated beds:

$$(\rho_l - \rho_v)g = A_1 \frac{180 \mu_v (1 - \epsilon)^2}{d^2 \epsilon^3} \left(\frac{C q_d}{\rho_v h_{lv}} \right) + A_2 \frac{1.75 \rho_v (1 - \epsilon)}{d \epsilon^3} \left(\frac{C q_d}{\rho_v h_{lv}} \right)^2 \quad (2-22)$$

where

$$C = 0.0157 \left(\frac{\rho_l - \rho_v}{d\sigma} \right)^{1/3} \quad (2-23)$$

This quadratic equation is solved for the dryout flux q_d . C is an empirical constant fit to their data and has units of $m^{4/3} s^{-2/3}$. A_1 and A_2 are not empirical constants, but rather are derived from integrating over the bed. They are both 1 for bottom-heated beds, and are 1/2 and 1/3, respectively, for volume-heated beds. The model successfully predicts the factor of two difference observed between bottom-heated and volume-heated bed data. However, to do so, the pressure in the bed from vapor flow must be integrated over the length of the bed. This, in essence, assumes that the pressure in the vapor at a particular elevation does not equal the pressure in the liquid. Thus a mechanism to keep the vapor from flowing horizontally and balancing this pressure difference must be found in order to make this model more physically meaningful. (Barleon and Werle [33] make a similar comment on the problem of rectifying the difference between bottom-heated and volume-heated beds.)

The Gabor-Cassulo model does not include capillary force, but does include both laminar and turbulent flow. In the turbulent limit, the dryout flux is proportional to the five-sixths power of particle diameter. This is different than the square root dependence predicted by Sowa, et al. [1], Ostensen [13,41], and Lipinski [25,27].

Lipinski [36] extended his zero-dimensional model [27] to one-dimension and obtained a single first-order differential equation for the saturation (liquid fraction between the particles). This report will describe more fully the derivation and consequences of that model since Reference 23 is only a summary. Improvements will also be made to the model. The equation reported in Reference 33 is:

$$\begin{aligned}
\frac{\sqrt{180} \sigma (1 - \epsilon) dJ ds}{\epsilon d ds dz} &= \sqrt{180} \sigma J \frac{d}{dz} \left(\frac{1 - \epsilon}{\epsilon d} \right) - (\rho_l - \rho_v) g \\
&+ \frac{1.75 (1 - \epsilon) S^2 z^2}{d \epsilon^3 h_{lv}^2} \left(\frac{1}{\rho_v (1 - s)^3} + \frac{1}{\rho_l s^3} \right) \\
&+ \frac{180 (1 - \epsilon)^2 S z}{d^2 \epsilon^3 h_{lv}} \left(\frac{\mu_v}{\rho_v (1 - 1.11 s)} + \frac{\mu_l}{\rho_l s^3} \right)
\end{aligned}
\tag{2-24}$$

where s is the saturation at elevation z , S is the volumetric power and J is a dimensionless relation between capillary pressure and saturation, called the Leverett function [57,61]. In Reference 36 a crude form for J is suggested to be

$$J = \frac{1 - s}{\sqrt{5}}
\tag{2-25}$$

In addition to the dryout flux, the one-D model predicts a stable dry zone for powers above the dryout power and defines the thickness. Contrary to the crude model of Lipinski and Rivard [16], stable dry zones are predicted for non-channeled beds. The one-dimensional model also predicts the dryout flux for stratified beds. In agreement with the earlier one-D model by Lipinski and Rivard [16], the model predicts that the dryout flux in a very deep bed is determined by a zero-D model (in this case, of Reference 26) using the particle diameter and porosity at the top of the bed. However, for non-deep beds the model predicts that capillary force will reduce the dryout flux considerably. (This will be described more fully in Section 5.4.)

Following the lead of Ostensen [13], (and apparently unaware of the model by Sowa, et al.) several other researchers developed dryout models based on flooding. Dhir and Barleon [35] produced

$$q_d = 0.135 h_{1v} \left[\frac{\rho_v (\rho_1 - \rho_v) g d \epsilon^3}{(1 - \epsilon) (0.69 + \rho_v / \rho_1)} \right]^{1/2} \quad (2-26)$$

Only the constant and dependence on density ratio is different from the Ostensen model (Equation 2-12) and the turbulent limit of the Lipinski model (Equation 2-19). This model applies to turbulent flow with no capillary force and is for bottom-heated beds. The authors suggest using a larger empirical constant for volume-heated beds.

Theofanous and Saito [38] derived a model very similar to that of Sowa, et al., (Equation (2-1)), using the same fit for the function f as Equation (2-2). Removing gravitational acceleration (with units cm/s^2) from their empirical constant, and setting $F = 1$ for spheres, their equation becomes

$$q_d = 0.071 h_{1v} \left[\frac{\rho_v \rho_1 g d \epsilon^3}{(1 - \epsilon) (\rho_v / \rho_1)^{1/4}} \right]^{1/2} \left(\frac{\mu_w}{\mu_1} \right)^{0.1} \quad (2-27)$$

where μ_w is the viscosity of water.

This is identical to Equation (2-3) except for the constant. (The difference is due to slightly different treatment of the water viscosity term.)

Henry and Fauske [40] produced a refreshingly different flooding dryout model based on the criterion for fluidizing liquid droplets in the overlying pool which are the same diameter as the particles, and which are packed with a 40 percent porosity:

$$q_d = 0.140 h_{1v} \sqrt{\rho_v \rho_1 g d} \quad (2-28)$$

Note that there is no dependence on bed porosity in this equation since all the action takes place above the bed. In all the other flooding models the heat flux varies

roughly with the square of the porosity. In addition, the dependence on fluid material properties is much simpler.

2.2.2 Channel Length Models

After the observation of channels at the top of the bed by Gabor et al. [2] in 1972, a model to predict the length of the channels eluded researchers for nearly a decade. Finally, Jones and Baker [31] produced a model to predict channel length. They suggest that at the bottom of the channel the capillary pressure equals the bed pressure. This yields the following equation for a channel length:

$$L_C = \frac{6\sigma}{\epsilon d(\rho_p - \rho_l)g} \quad (2-29)$$

where ρ_p is the density of the particle material. This is a very significant step forward since it allows understanding of channeled beds. Although Jones and Baker did not pursue the matter, their channel length model leads directly to a dryout model for channel beds, as will be seen in Section 3.3.1.

Recently two more channel models have been proposed by Schwalm and Nijsing [43] and by Reed [49]. Both of these models were developed independently of each other and of the channel model by Jones and Baker [31]. The channel model in this report was developed with knowledge only of the Jones-Baker model. All four channel models give similar results, with varying degrees of complexity.

Schwalm and Nijsing [43] presented a channel length model very similar to that of Jones and Baker [31]. It uses the Leverett function [57,61] to better define the capillary force and uses the Lipinski one-dimensional model [36] to obtain an estimate of the saturation to use in the Leverett function. The channel length is

$$L_C = \frac{\sigma \sqrt{\epsilon/\kappa}}{\rho_p g (1 - \epsilon)} J \quad (2-30)$$

where κ is permeability. Schwalm and Nijsing suggest using Equation (2-23) for J with s equal to about 0.5. Note that the liquid density is omitted.

Reed [49] suggests a similar use of the Leverett function, but concludes it is acceptable to use it near $s = 1$ but before it begins to drop toward zero. He includes the liquid density as Jones and Baker did plus the effect of contact angles and obtains:

$$L_c = \frac{4.62 \sigma \cos \theta}{\epsilon d (\rho_p - \rho_l) g} \quad (2-31)$$

This is very similar to the formula of Jones and Baker [31] (Equation (2-29)). (Since Reference 49 came to the attention of the author only at the final stages of the preparation of this report, the other aspects of it will not be included in this report. But the reference is recommended reading.)

In all of the models described a single particle diameter d is used. Thus the models are ideally suited for uniform spheres, and most experimental research has been performed with spheres. The reason for this is to simplify the investigation process. However, all of the models can easily accommodate both rough particles and distributions of particle sizes by simply using the proper average diameter. They can even accommodate slightly degraded pin bundles, and in some circumstances, intact pin bundles. The challenge is to obtain the proper definition of average. This will be discussed in Section 5.6.

2.3 Summary of Previous Research

Over the last ten years experiments and modeling of dryout in particle beds have produced over fifty papers. Considering only volume-heated beds, dryout measurements have been made for over 260 different beds involving six different fluids (water, acetone, freon-113, methanol, isopropanol, and sodium) and five different solids (steel, bronze, copper, lead, and urania). Particle diameters have ranged from 0.26 mm to 16 mm, bed thickness from 15 mm to 450 mm, and resulting dryout heat flux from 16 kW/m² to 4300 kW/m². These volume-heated data are consolidated in Appendix A.

At least fifteen models to predict dryout have been produced and are summarized in Table 2-1. Six of them have been based on flooding and are nearly identical. The dependence of the dryout flux on particle diameter is predicted to range from square to square root, the dependence on bed thickness from strong to none, and on porosity from about fifth power to zero power. The most involved models include gravity and capillary force, and allow for laminar or turbulent flow. Models to predict channel length in a bed have also been developed. This report gives a more complete description of the derivation of some of that past modeling effort by the author, and introduces some extensions and improvements.

Table 2-1

Summary of Dryout Models for Particle Beds

<u>Dryout Model</u>	<u>Equation</u>	<u>Features and Application</u>
Sowa, et al. [1]	2-3	Flooding, large particles
Gabor, et al. [3]	2-4,5	Sodium-UO ₂ bed, 0.1-1.0 mm diameter particles
Dhir-Catton [5]		
Deep	2-6	Gravity, liquid drag, small particles, deep beds
Shallow	2-7	Bed fluidization, shallow beds
Hardee-Nilson [8]	2-9	Gravity, vapor and liquid drag, small particles, deep beds
Ostensen [13,41]	2-12	Flooding, large particles
Shires-Stevens [20]	2-13	Gravity and capillary force, vapor drag, small particles, medium and deep beds
Lipinski Zero-D [25,27]	2-14	Gravity and capillary force, vapor and liquid drag, small and large particles, medium and deep beds, downward boiling possible
Jones, et al. [26,29]	2-20	Gravity, vapor and liquid drag with shear, small particles, deep beds
Gabor-Cassulo [32,46]	2-22	Gravity, vapor drag and bubble release, small and big particles, volume and bottom-heating, deep beds
Lipinski One-D [36] (better described and extended in this work)	2-24	Gravity and capillary force, vapor and liquid drag, small and large particles, medium and deep beds, particle stratification, non-uniform heat source, downward boiling possible

Table 2-1 (Continued)

<u>Dryout Model</u>	<u>Equation</u>	<u>Features and Application</u>
Dhir-Barleon [35]	2-26	Flooding, large particles
Theofanous-Saito [38]	2-27	Flooding, large particles
Henry-Fauske [40]	2-28	Flooding, large particles
Squarer [48]	~2-12	Flooding, large particles

3. ONE-DIMENSIONAL MODEL DEVELOPMENT

There is need for a general boiling and dryout model to account for the diverse behavior observed experimentally in particle beds. Such a model should extend to a wide range of circumstances such as might be encountered in post-accident debris. The model should be based on physical phenomena and experimentally verified relations so that some confidence can be had in extrapolating it to regions where data is scarce and difficult to obtain. Ideally the model should not require empirical constants fit to the data it is trying to predict but rather should agree with observed behavior based on its initial assumptions alone. This aspect gives confidence that the important phenomena are understood and included in the model.

3.1 Basic Phenomena and Equations

Figure 3-1 shows a stylized view of the flow of liquid and vapor within a bed of particles. The bed has been made a rectangular array of uniform spheres for easier visualization. The arguments would still apply to a random array of rough particles. The circles are not touching because the vertical cutting plane has been chosen not to pass through the points of contact. Although it is difficult to show in two dimensions, the liquid is continuous in three dimensions. The saturation has been chosen to be less at the bottom of the figure. (Subsequent predictions of the model will show this sometimes to be the case. This simply implies that the local vapor velocity must increase with elevation.)

Dryout is shown occurring at the bed bottom where the liquid fraction reaches zero. Steady-state conditions are depicted, and the model to be developed will apply only to steady conditions. Elevation in the bed is designated as z and is measured from the plane of zero heat flow (bed bottom in a bottom-insulated bed).

The most important and difficult equation in modeling boiling in particle beds is the momentum conservation equation. Considerable research has been performed in the petroleum and chemical industries concerning fluid flow through a porous medium [55,56,57,59-68]. For single-phase flow, Ergun [62,67] has combined the pressure drop

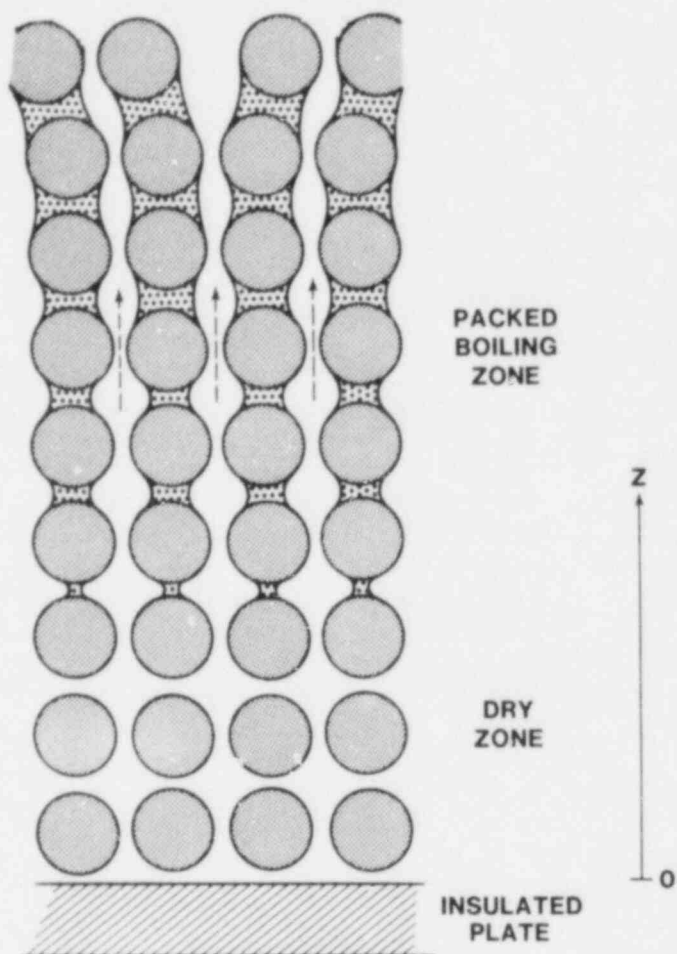


Figure 3-1. Stylized View of Liquid and Vapor Flow Through a Particle Bed. The circles are separated because the vertical cutting plane misses the points of contact between the spheres. (The bed is not fluidized.)

equation of Blake and Kozeny [67] for laminar flow and of Burke and Plummer [67] for turbulent flow to obtain the general equation:

$$-\frac{dP}{dz} = \frac{1.75 (1 - \epsilon) \rho v^2}{d \epsilon^3} + \frac{150 (1 - \epsilon)^2 \mu v}{d^2 \epsilon^3} \quad (3-1)$$

where P is pressure, z is elevation, ϵ is bed porosity, ρ is density, v is superficial velocity (i.e., average true fluid velocity times porosity), and μ is kinematic viscosity. The second and third terms are the turbulent and laminar components, respectively. The factor of 150 differs from the factor 180 used in previous presentations. The 180 was used previously to be consistent with early dryout modeling and was derived analytically by Kozeny and Carman [57]. However, Blake [67] subsequently showed (empirically) that 150 was a better factor for spheres and Ergun used this factor in his equation.

Dryout models and data have finally become accurate enough that such a small difference is no longer negligible. Thus 150 will be used. The factor of 1.75 is also empirical and was determined by Burke and Plummer [67] from early flow experiments. The Ergun equation is not the only one which has been proposed for flow through a porous medium, but it works quite well [67]. For velocities typical of dryout, the transition from laminar turbulent flow occurs with about 1 mm diameter particles.

The Ergun equation must be modified for two-phase flow. The flow area occupied by one phase will reduce that available for the other fluid. Much experimental and analytical work has been performed to determine the pressure drop in a bed with two-phase flow. Generally, it is assumed that the pressure drop determined by the single-phase equation can be modified by multiplying the bed permeability by dimensionless attenuation coefficient called relative permeability. (Relative permeability is similar to the inverse of a two-phase friction factor.) The relative permeability is a function of the liquid fraction in the flow area between the particles. This liquid fraction is called saturation. The relative permeability quantifies the effect of the reduced flow area to each of the phases. There is a separate relative permeability for the vapor and for the liquid phases,

designated κ_v and κ_l , respectively. As the saturation decreases, κ_l changes from one to zero and κ_v changes from zero to one. The two components need not, and generally do not, sum to one.

Figure 3-2 shows a plot of relative measured permeabilities vs. saturation in the bed [69]. This data was obtained from water and air co-current flow through sand. It is empirical and normalized to the pressure drop obtained from single-phase flow measurements in the same apparatus. Since the data is empirical, it includes all the physical sources of friction.

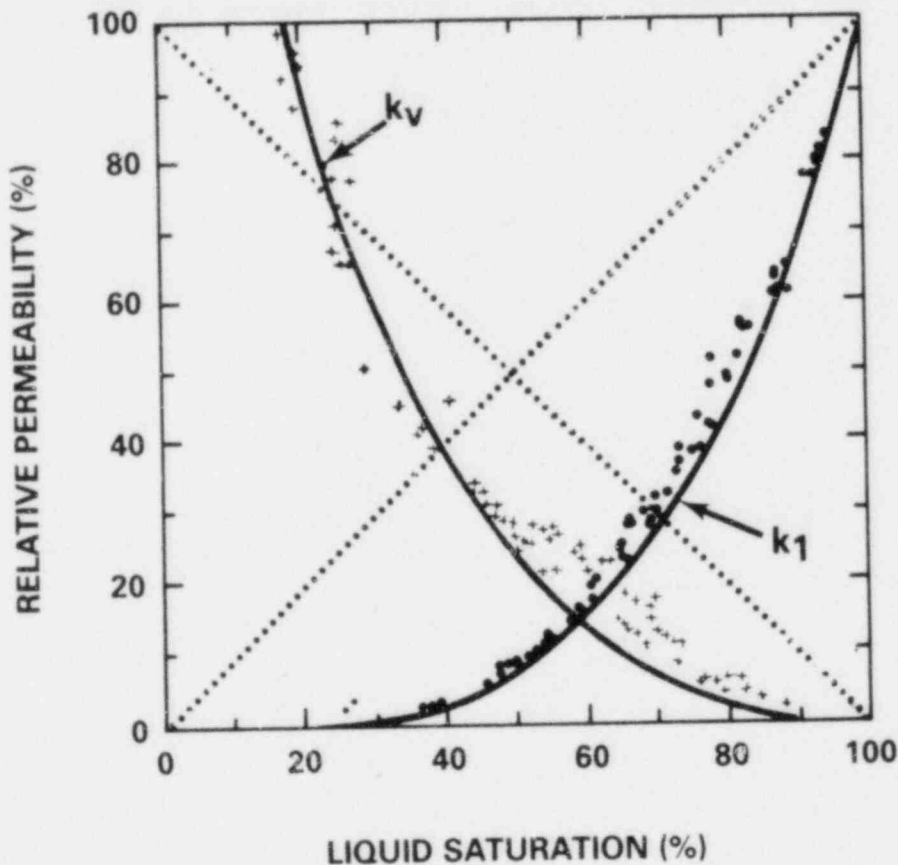


Figure 3-2. A Typical Example of Relative Permeabilities (From Wyckoff and Botset [59]). Solid curves correspond to Equations (3-4) and (3-5). Dotted lines represent linear relative permeabilities.

Burdine [63,68] has derived formulae for the relative permeabilities based on Poiseuille's law and Corey [64,65,67] has extended that derivation. Corey first defined an effective saturation s in terms of a residual saturation s_r :

$$s = \frac{s_t - s_r}{1 - s_r} \quad (3-2)$$

where s_t is the true saturation. The residual saturation is the liquid fraction which is bound between the particles by capillary force and which remains with a given pressure drop across the bed. Normally the residual saturation is removed by evaporation. Brown et al. [66] suggest a formula for residual saturation which for simple bed drainage becomes

$$s_r = \frac{1}{22} \left[\frac{(1 - \epsilon)^2 \sigma \cos \theta}{d^2 \epsilon^3 \rho_l g} \right]^{0.264} \quad (3-3)$$

where σ is surface tension, θ is the wetting contact angle between the liquid and particle, and g is gravitational acceleration. However, as shall be seen later, the value of the residual saturation is not important in dryout calculations. For uniform spheres, the relative permeability suggested functions developed by Corey [64,65,68] become

$$\kappa_v = (1 - s)^3 \quad (3-4)$$

$$\kappa_l = s^3 \quad (3-5)$$

Using a residual saturation of 0.17, Equations (3-4) and (3-5) are plotted in Figure 3-. The agreement with the data is reasonable. Also shown as dotted lines are the linear relative permeability used in the equations by Hardee and Nilson [8] and by Shires and Stevens [20]. The need for non-linear relative permeabilities is apparent.

The data in Figure 3-2 was obtained with co-current flow. However because of the large difference between the liquid and vapor velocities the difference between co-current and counter-current flow will be assumed negligible. This assumption is quite valid with respect to the vapor flow. But the liquid flow may be affected by the different flow directions if the interphase shear is large. The existence of possible error in the model introduced by this assumption that the effects of co-current and counter-current flow on the liquid are identical must be recognized. How well the model agrees with counter-current flow dryout data will reflect the validity of this assumption.

The relative permeabilities in Equations (3-4) and (3-5) are for laminar flow. It will be assumed that they also apply to turbulent flow. (Wallis [60] has shown that in pipe flow there is little difference between the laminar and turbulent two-phase friction factors.)

The two momentum conservation equations for flow in the bed may now be written as

$$\frac{1.75(1-\epsilon)\rho_v v_v |v_v|}{d\epsilon^3(1-s)^3} + \frac{150(1-\epsilon)^2 \mu_v v_v}{d^2\epsilon^3(1-s)^3} + \frac{dP_v}{dz} + \rho_v g = 0 \quad (3-6)$$

$$\frac{1.75(1-\epsilon)\rho_l v_l |v_l|}{d\epsilon^3 s^3} + \frac{150(1-\epsilon)^2 \mu_l v_l}{d^2\epsilon^3 s^3} + \frac{dP_l}{dz} + \rho_l g = 0 \quad (3-7)$$

The absolute value signs in the first terms of the equations are necessary to allow for positive or negative (up or down) flow. The effect of gravity has also been included.

The pressure in the liquid (P_l) is different from the pressure in the vapor (P_v) due to capillary force. This influence of capillary force was first introduced

into dryout modeling by Shires and Stevens [20]. Theirs was an important contribution because in many cases the effect of capillary force is several times that of gravity, and including it in the modeling is necessary to obtain even crude agreement with data. (Gabor et al. [3] also included capillary force in their early calculations, but never developed its effect in a dryout model.)

The influence of capillary force in a volume-heated particle bed with boiling needs some clarification. Referring back to Figure 3-1, one can see curvature in the liquid-vapor interface. At the bottom of the figure where the vapor fraction is large, the vapor forces the liquid into the small spaces between the particles. This creates a small radius of curvature on the liquid surface. This in turn means there is a large pressure difference between the liquid and vapor in that region, with the vapor being at the higher pressure. The radius of curvature on the liquid surface is not uniform throughout the local region and may even be reversed in some places. But the local pressure in the vapor is uniform. This can occur because the capillary pressure difference is

$$P_V - P_L = \Delta P = \sigma \left(\frac{1}{r_1} + \frac{1}{r_2} \right) \quad (3-8)$$

where r_1 and r_2 are the smallest and largest radii of curvature, and the smaller radius dominates, even if the largest radius is negative. At the top of the figure where the saturation is large, the vapor allows the liquid surface to become more straight and the pressure difference between the liquid and vapor is small.

Typically the liquid flow velocity is small since the liquid is much more dense than the vapor. Thus the liquid flow resistance is small and gravity can usually draw in as much liquid as is needed to maintain the vapor flow, and the pressure in the liquid at the bed bottom is only slightly less than hydrostatic (with respect to the top). Without capillary force, the nearly hydrostatic pressure gradient in the liquid would be the main force driving out the vapor. However, with capillary force there can be a greater pressure gradient driving out the vapor. With a large vapor production rate a large pressure develops in the vapor at the bed

bottom (due to the resistance to vapor flow). Normally this large pressure in the vapor would also be felt by the liquid and would prevent any more liquid from reaching the bed bottom. But with capillary force the vapor pushes the liquid surface between the particles and a large pressure difference across the interface develops. This allows the pressure in the liquid to remain small (near hydrostatic) while the pressure in the vapor is very large. In a sense, capillary force protects the liquid from the large pressures in the vapor developed by the large generation and flow rates. Thus vapor and heat removal can be larger without dryout occurring. (Note that for this condition to occur, the vapor fraction must be greatest at the bed bottom.)

The effect of capillary force is reduced if the contact angle between the particles and the liquid is greater than zero. This contact angle is very dependent on surface conditions and can vary significantly. The angle is theoretically zero between water and any high-energy surfaces such as metals, but it is very difficult to achieve this result in practice [70]. Stepanov, et al. [70] measured a contact angle of about 37° between water and stainless steel. Ponter, et al. [72] measured 66° between water and copper. But Fox, et al. [70] were able to attain near 0° with both stainless steel and brass. Quartz, on the other hand, wets more easily with a measured angle of about 3.5° [73]. Sodium on UO_2 will have a large contact angle at low temperatures, but at the boiling point the angle is zero [74]. These differences are compounded by the difference between advancing and receding angles (all angles quoted are receding angles) and surface roughness [75].

In view of these wide variations in contact angle, one really needs a direct measurement for effect of surface tension with the actual particles used in each dry-out measurement. Only Shires and Stevens [20] have done this. They measured the height water was drawn up into a dry bed of their steel particles and found that the height was about 71% of that suggested by models. This implies that $\cos \theta = 0.7$, which agrees generally with the measured contact angle of 37° by Stepanov. In view of the uncertainty in this area, it will be somewhat arbitrarily assumed for this report that $\cos \theta = 0.8$ with all particles except UO_2 . Because of the data for sodium on UO_2 and for water on SiO_2 , $\cos \theta = 1$ will be assumed for UO_2 particles. Hopefully, future data will help refine these assumptions.

The difference between the liquid and vapor pressures has been proposed by Leverett [57,61] to be

$$P_v - P_l = \sigma \cos \theta \sqrt{\frac{\epsilon}{K}} J \quad (3-9)$$

where ϵ is permeability, and J is a dimensionless function called the Leverett function which depends only on saturation. An example of the Leverett function for sand and water is shown in Figure 3-3. Note that the function (and capillary pressure) increases as the saturation decreases, as was described above. The function becomes very large near the residual saturation. In addition, there is a difference between the imbibition data and the drainage data. The drainage data is more appropriate for boiling in a debris bed. Brooks and Corey [65] have suggested that

$$P_v - P_l \propto \frac{1}{s^\gamma} \quad (3-10)$$

where γ is a positive number. This models the pressure increase near the residual saturation but fails to go to zero at $s = 1$. Therefore, an alternate form is suggested:

$$P_v - P_l \propto \left(\frac{1-s}{s}\right)^\gamma = (s^{-1} - 1) \quad (3-11)$$

Kozeny [57] has derived an analytical form for the total capillary pressure drop in a bed of spheres from wet to dry:

$$\Delta P = \sigma \cos \theta \sqrt{\frac{\epsilon}{5K}} \quad (3-12)$$

Following this lead, it is suggested that a semi-empirical Leverett function be

$$J = \frac{(s^{-1} - 1)^{0.175}}{\sqrt{5}} \quad (3-13)$$

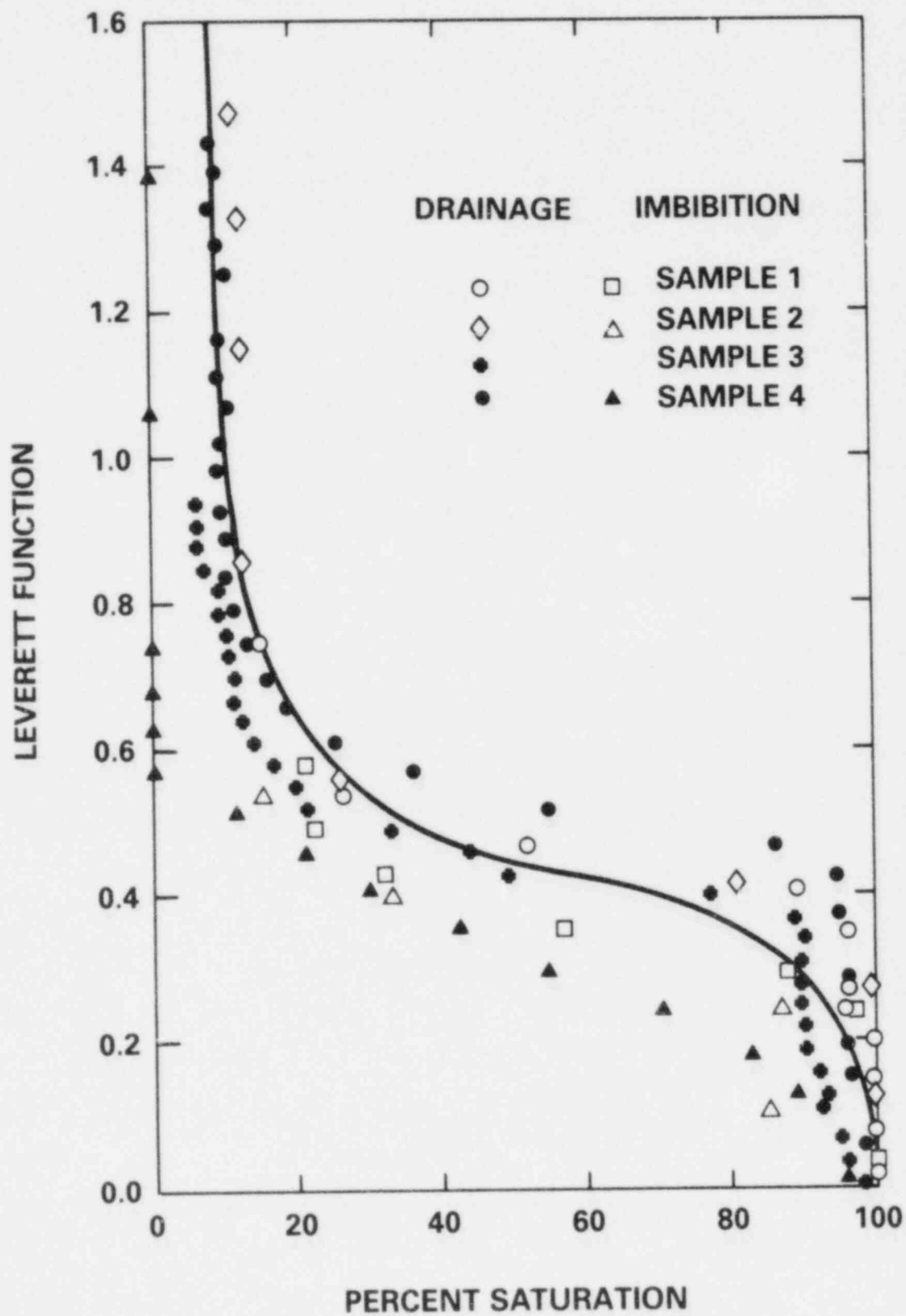


Figure 3-3. Typical Examples of Some Leverett Functions (From Leverett [57,61]). The curve is Equation (3-13)

The number for γ (0.175) was chosen so as to fit the data in Figure 3-3, as is shown in the figure. (Equation 3-2 was also used, with $s_r = 0.1$ and $\cos \theta$ was assumed equal to one since sand is quartz.) Other Leverett functions are possible, and hopefully future experiments will help determine the best form.

The energy conservation equation is straightforward:

$$\frac{d}{dz} (\rho_v v_v h_{1v}) = S \quad (3-14)$$

where S is the power per unit volume of bed as a function of elevation z . The mass conservation equation is also straightforward:

$$\frac{d}{dz} (\rho_v v_v + \rho_l v_l) = 0 \quad (3-15)$$

All of the basic equations for the behavior of dry-out in a volume-heated bed are brought together below for convenience. (Equation (3-16) came from (3-9) with the Blake-Kozeny permeability inserted.)

$$\frac{1.75(1 - \epsilon)\rho_v v_v |v_v|}{d\epsilon^3(1 - s)^3} + \frac{150(1 - \epsilon)^2 \mu_v v_v}{d^2\epsilon^3(1 - s)^3} + \frac{dp_v}{dz} + \rho_v g = 0 \quad (3-6)$$

$$\frac{1.75(1 - \epsilon)\rho_l v_l |v_l|}{d\epsilon^3 s^3} + \frac{150(1 - \epsilon)^2 \mu_l v_l}{d^2\epsilon^3 s^3} + \frac{dp_l}{dz} + \rho_l g = 0 \quad (3-7)$$

$$\frac{d}{dz} (\rho_v v_v h_{1v}) = s \quad (3-14)$$

$$\frac{d}{dz} (\rho_v v_v + \rho_l v_l) = 0 \quad (3-15)$$

$$P_l - P_v = \frac{\sqrt{150} \sigma (1 - \epsilon) \cos \theta J}{\epsilon d} \quad (3-16)$$

$$J = \frac{(s^{-1} - 1)^{0.175}}{\sqrt{5}} \quad (3-13)$$

3.2 Bed Bottom Boundary Condition

Reduction and solution of the above equations requires use of boundary conditions at the bottom and at the top of the bed. At the bed bottom the bed support structure can be either permeable (e.g., a grid) or impermeable (e.g., a plate). The former condition allows the possibility of flow into the bed from below, yielding a net flow through the bed. The latter condition implies no net flow through the bed. Furthermore, the bed support can be adiabatic or cooled. All of the above situations are allowed by the bed equations derived since the equations apply to flow conditions within the bed, regardless of the boundary conditions.

The condition of a net flow through the bed is introduced when Equation (3-15) is integrated to obtain

$$\rho_v v_v + \rho_l v_l = w \quad (3-17)$$

where w is the net mass flux through the bed (i.e., into the bed bottom from below). For a bed which rests on an impermeable plate, $w = 0$.

The condition of an adiabatic or cooled bed bottom is accommodated when Equation (3-14) is integrated to obtain

$$h_{1v} \rho_v v_v \Big|_0^z = \int_0^z S dz \quad (3-18)$$

The plane where $z = 0$ is defined as the location of zero heat flow. Thus, for example, with an insulated plate at the bed bottom, $z = 0$ would occur at the bed bottom and the vapor flow there would be zero. If the bed bottom were cooled, $z = 0$ would be defined at the plane dividing upward heat flow from downward heat flow (and again, the vapor flow there would be zero). Thus Equation (3-18) becomes

$$h_{1v} \rho_v v_v = q \quad (3-19)$$

where q is the heat flux at elevation z in the bed. For a uniform source,

$$q = Sz \quad (3-20)$$

Subtracting Equation (3-7) from (3-6), differentiating Equation (3-16), and inserting it with Equations (3-19) and (3-20) yields

$$\begin{aligned} & - \frac{\sqrt{150} \cos \theta \sigma (1 - \epsilon) dJ ds}{\epsilon d} - \sqrt{150} \cos \theta \sigma J \frac{d}{dz} \left(\frac{1 - \epsilon}{\epsilon d} \right) + (\rho_1 - \rho_v)g \\ & = \frac{1.75(1 - \epsilon)q^2}{\epsilon^3 d h_{1v}^2} \left(\frac{1}{\rho_v (1 - s)^3} + \frac{1}{\rho_1 s^3} \right) \\ & + \frac{150(1 - \epsilon)^2 q}{\epsilon^3 d^2 h_{1v}} \left(\frac{\mu_v}{\rho_v (1 - s)^3} + \frac{\mu_1}{\rho_1 s^3} \right) \\ & + \frac{(1 - \epsilon)w}{\epsilon^3 d \rho_1 s^3} \left(+ 1.75 w + \frac{3.5q}{h_{1v}} - \frac{150(1 - \epsilon)\mu_1}{d} \right) \end{aligned}$$

for $q > wh_{1v}$

(3-21)

(The upper sign applies for $q > wh_{1v}$, and the lower sign applies for $q < wh_{1v}$.) The first two terms in Equation (3-21) are the capillary pressure gradients due to variations in the saturation and particle diameter. The second term is operative only in stratified beds. The third term is the hydrostatic pressure gradient. The fourth and fifth terms are laminar and turbulent flow resistances, respectively, and the last term is the flow resistance from the inlet flow. Equation (3-21) is a first order differential equation and may be solved numerically once the bed characteristics are chosen. For negligible capillary force the equation becomes algebraic (see Section 5.1).

3.3 Bed Top Boundary Condition

Equation (3-21) requires a top boundary condition for solution. As described in Section 2.1, experiments have shown that there may be two possible boundary conditions at the top of the bed. With an overlying pool near the boiling temperature, channels occur in the top portion of the bed [2,3]. With a subcooled overlying pool and a highly conductive fluid (such as sodium) it is possible to have a suppression of channel formation [30,54] and have a non-boiling subcooled zone at the top of the bed [9,12]. The one-D model equations apply only to the packed boiling region in the bed, so the above observations must be formulated in terms of a boundary condition at the top of the packed boiling zone.

3.3.1 Channel Length Determination

As described in Section 2.1 models or explanations for the existence of channels at the top of a non-subcooled bed eluded researchers for many years. Jones and Baker [31] were the first to develop a model for channel length. It was based on the criterion that at the bottom of the channel capillary force just balanced the weight of the overlying bed. They used the full capillary force of Kozeny [57] to obtain a channel length of

$$L_{JB} = \frac{6\sigma}{\epsilon d (\rho_p - \rho_1)g} \quad (3-22)$$

One minor difficulty with the Jones-Baker channel length is that all of the capillary force (from fully wet to fully dry) is presumed to be used to support the channel. This leaves nothing but gravity for liquid and vapor transport in the packed portion of the bed. In actuality, some of the capillary force will be used for channel formation and some in the packed portion of the bed. For example, with very heavy particles (or a porous brick) most or all of the capillary force would be used within the packed region of the bed.

The amount of capillary pressure in the bed is a function of the saturation. Thus the channel length will be a function of saturation near the base of the channel. Schwalm and Nijsing [43] and Reed [49] accommodated this fact by using the Leverett function in their channel models but did not determine a physical criterion for the proper saturation to use in the Leverett function. Such a criterion is needed for a physical channel model.

Figure 3-4 shows a channel penetrating the top of a particle bed. Below the channel the liquid surface may be seen being forced between the particles by the pressure developed in the vapor as large amounts of vapor try to flow out of the bed. (This was described in Section 3.2.) The curvature in the liquid surface helps to contain this pressure via capillary force, but it can do so only if the bed particles remain in place to force curvature into the liquid surface. The particles will remain in place if there is enough pressure on them from the weight of the bed above them. Near the top of the bed there is not a sufficient pressure from the weight of the bed and the vapor may push back both the liquid and the particles. In this fashion channels are formed.

If all pressures are defined to be zero at the top of the bed, and if friction between the particles is assumed negligible, the pressure in the vapor at any location in the channel must be just sufficient to offset the weight of the overlying particles plus liquid. (Both particle weight and liquid weight must be considered because, in an infinitesimal movement of the channel wall, both particles and liquid must move. Jones and Baker [31] and Reed [49] included this aspect in

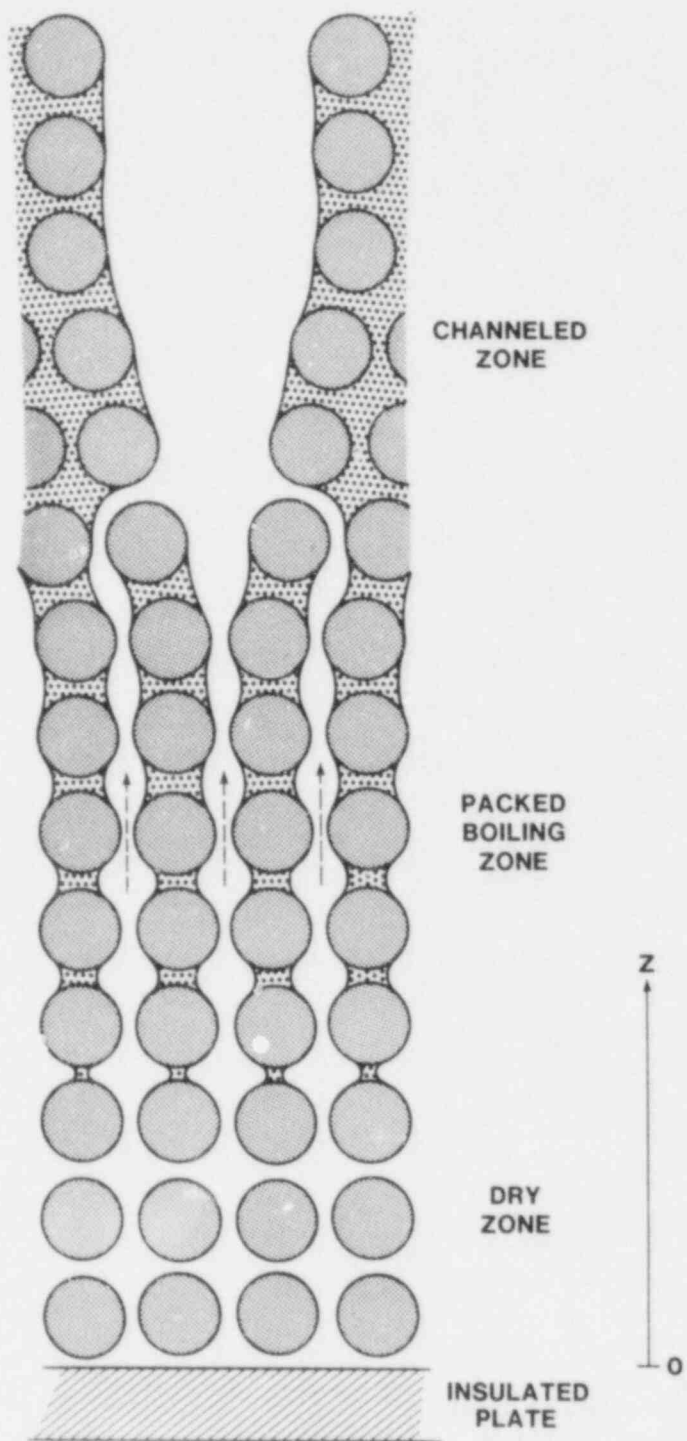


Figure 3-4. Channel Penetrating the Top of a Particle Bed. (See also Figure 3-2.)

their derivations but Schwalm and Nijsing [43] did not.) Thus

$$P_v = (\rho_p(1-\epsilon) + \rho_l\epsilon)g(L-z) \quad (3-23)$$

where ρ_p is the particle density and L is the bed thickness. The pressure in the liquid is simply hydrostatic minus flow resistance. Between the channels the vapor fraction is small and thus resistance to the fairly slow liquid flow is negligible. Thus, in the channeled region of the bed, the liquid pressure is

$$P_l = \rho_l g(L-z) \quad (3-24)$$

(Note that in this case the particle weight is neglected and the pressure is not multiplied by porosity since the particles support themselves and the liquid flows freely between the particles.)

The layer of particles below the base of the channels is packed and Equation (3-16) may be used to determine the pressure difference there. Continuity of pressure to the overlying channel then requires that

$$\frac{\sqrt{150} \cos \sigma (1 - \epsilon) J}{\epsilon d} = (\rho_p (1 - \epsilon) + \rho_l \epsilon) g L_c - \rho_l g L_c \quad (3-25)$$

where L_c is the channel length. Rearranging yields

$$L_c = \frac{\sqrt{150} \cos \theta \sigma J}{\epsilon d (\rho_p - \rho_l) g} \quad (3-26)$$

The similarity to the Jones-Baker channel length (Equation (3-22)) is apparent. However J is a function of saturation, so another condition is needed. That condition is continuity of pressure gradient.

The pressure gradient in the vapor may be determined by combining Equations (3-6) and (3-19) to obtain

$$\frac{dP_v}{dz} = - \frac{1.75(1 - \epsilon)q^2}{d \epsilon^3 \rho_v h_{1v}^2 (1 - s)^3} - \frac{150(1 - \epsilon)^2 \mu_v q}{d^2 \epsilon^3 \rho_v h_{1v} (1 - s)^3} - \rho_v g \quad (3-27)$$

Differentiating Equation (3-23) and combining with Equation (3-27) yields

$$\frac{(1 - \epsilon)q_c}{\epsilon^3 d \rho_v g h_{1v} (1 - s)^3} \left(\frac{1.75 q_c}{h_{1v}} + \frac{150(1 - \epsilon)\mu_v}{d} \right) = \rho_p(1 - \epsilon) + \rho_l \epsilon \quad (3-28)$$

where q_c is the heat flux at the base of the channeled region. For uniformly-heated beds,

$$q_c = S(L - L_c) \quad (3-29)$$

Since q_c is a function of L_c , Equations (3-26) and (3-28) are coupled. Together they yield both the channel length (which identifies the location of the top of the packed boiling zone) and the saturation at the top of the packed boiling zone.

The channel depicted in Figure 3-4 and in this model development is idealized. In practice channels can be twisted and irregular. In addition, Barleon and Werle [52] note a loosened region below a region of obvious channeling. Since the above channel length was based on the depth at which vapor could move particles, it corresponds to the combined thickness of the obvious channel region and the

loosened region. Since resistance to vapor flow is much reduced in both of these regions, the effect is the same if the combined region is simply designated as "channeled."

The flow behavior in the channeled region is not modeled explicitly. Rather, the flow resistance in that zone is assumed negligible. Clearly, as channels begin to dominate the bed, the resistances in that region become important. Therefore, the present model will be assumed inapplicable when the channel length exceeds half the bed thickness.

3.3.2 Channel Suppression in a Subcooled Bed

A subcooled bed is one in which the overlying liquid is cooled below the saturation temperature. With sodium, this results in a non-boiling zone (subcooled zone) overlying the boiling zone. If the subcooled zone is thick, the boiling zone is packed. If the subcooled zone is thin, channels may penetrate it and part of the boiling zone.

For subcooled beds in which channels are suppressed, the boundary condition at the top of the boiling zone is uncertain. One might believe that the saturation is one at that location because the vapor all condenses at that level. However, in the condensation process, the superficial vapor velocity decreases and Equation (3-14) is no longer valid. Thus the proper boundary condition for the top of the packed zone as it applies to Equation (3-21) should occur at the elevation just before condensation begins.

Figure 3-5 shows saturation as a function of elevation for a packed sodium-filled boiling zone 100 mm thick with a particle diameter of 0.3 mm, bed porosity of 40 percent, and volumetric power of 50 W/kg- UO_2 (0.30 MW/m³). Curves with various assumed saturations at the top of the zone are shown. The curves have similar shapes, and as the top boundary condition varies from $s = 0.2$ to $s = 1$, the average saturation in the bed increases. Most of the curves are close to the curve with $s = 1$ at the top. Since most of the curves are similar, and since $s = 1$ maximizes the saturation in the bed (thus minimizing the pressure) it will be assumed that $s = 1$ is a reasonable approximation for the top of a boiling zone in a subcooled bed without channel penetration. (However, caution must be used with this boundary condition since the resistance to vapor flow is singular at $s = 1$).

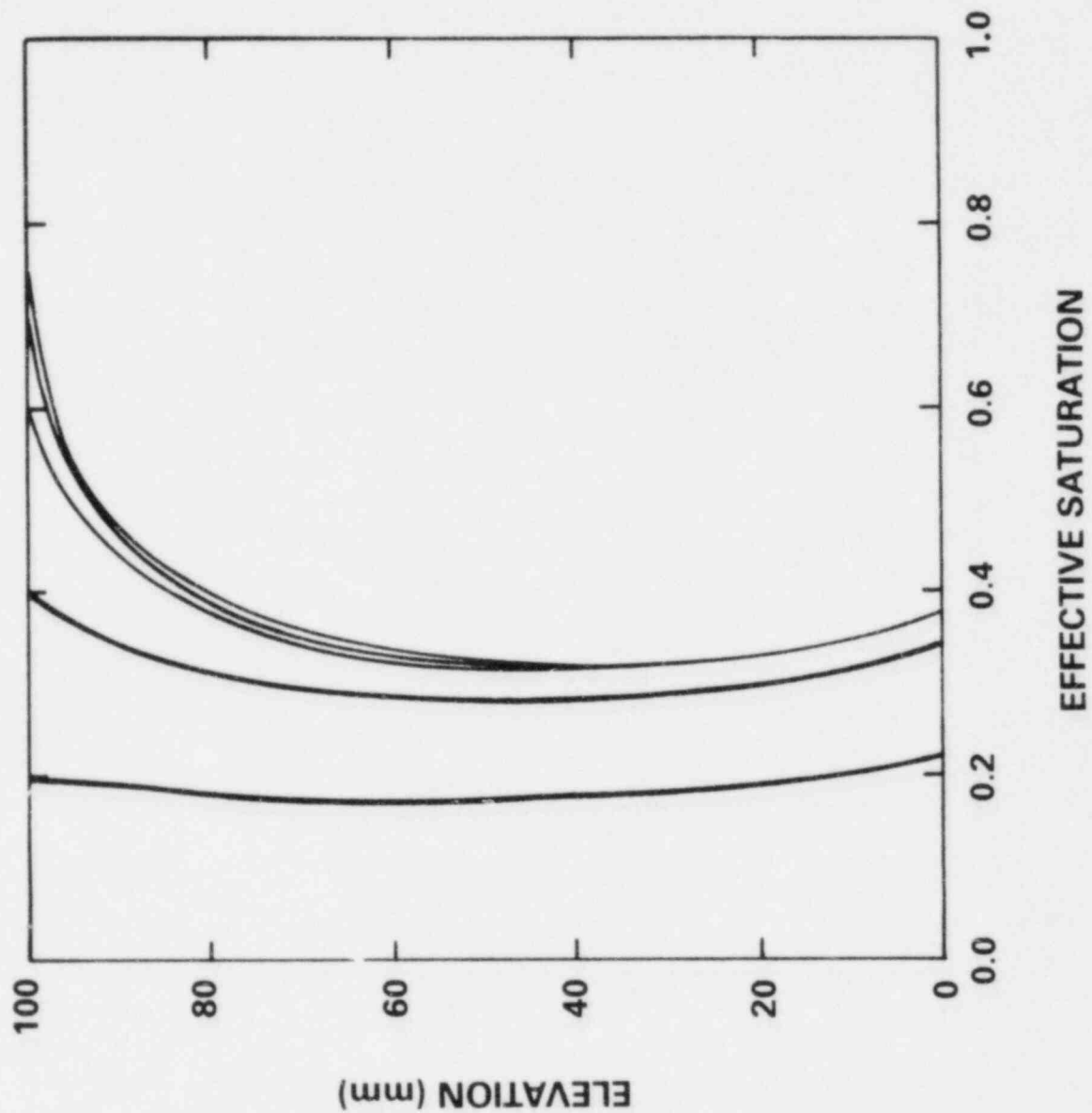


Figure 3-5. Effective Saturation vs. Elevation in a Packed Sodium-UO₂ Boiling Zone 100 mm Thick With 40% Porosity and 0.3 mm Particle Diameter. The power is 50 W/kg-UO₃ (0.30 MW/m³). Saturations of 0.2, 0.4, 0.6, 0.8, and 1.0 at the zone top are considered.

Figure 3-6 shows various pressures for a similar bed 150 mm thick with 67 W/kg-UO₂ and with the overlying sodium subcooled. Thus, a subcooled zone in the bed (54 mm thick) overlies a boiling zone. The vapor pressure is obtained by using Equation (3-27) after obtaining s from Equation (3-21) numerically. Also shown is the bed pressure, (which equals the right-hand side of Equation 3-23). (Zero pressure is at the top of the bed.) Note that at elevation 92 mm, the pressure in the vapor equals the bed pressure. If the subcooled zone thickness were slightly thinner the pressure in the vapor would exceed the bed pressure and a channel would form. If the subcooled zone thickness were greater, no channel would form. Thus, 54 mm is the subcooled zone thickness which yields incipient channel penetration of the subcooled zone. This process of comparing pressures can be used as a criterion for channel penetration of a subcooled zone.

Once channel penetration occurs, the channel length will be 58 mm, as determined by where the two curves touch in Figure 3-6. (The channel remains in place because the vapor flow in the channel is too rapid to allow significant vapor condensation.) This is exactly the same as using Equations (3-26) and (3-28) and ignoring the subcooled zone. Note that the subcooled zone thickness at incipient channel penetration is slightly less than the channel length which results. This effect has been noted experimentally by Barleon, et al. [53]. However, the model does not account for the shorter channels observed in subcooled beds [53]. That may require further analysis of the condensation process in the subcooled zone.

3.4 Summary of the One-D Model Basis and Final Equations

The one-dimensional model for boiling in a packed porous medium is based on conservation laws for mass, momentum, and energy with separate momentum equations for vapor and liquid flow. It includes the effects of both laminar and turbulent flow, two-phase friction, and capillary force. The boundary condition at the bed bottom includes the possibility of inflowing liquid and either an adiabatic or a bottom-cooled support structure. The top of the bed may be either channeled or subcooled. In the first case, a criterion for the channel length and the saturation at the base of the channels is obtained. In the latter case, a criterion for penetration of the subcooled zone by channels is obtained. With the different boundary conditions the model becomes very general and applicable to channeled or non-channeled beds, with

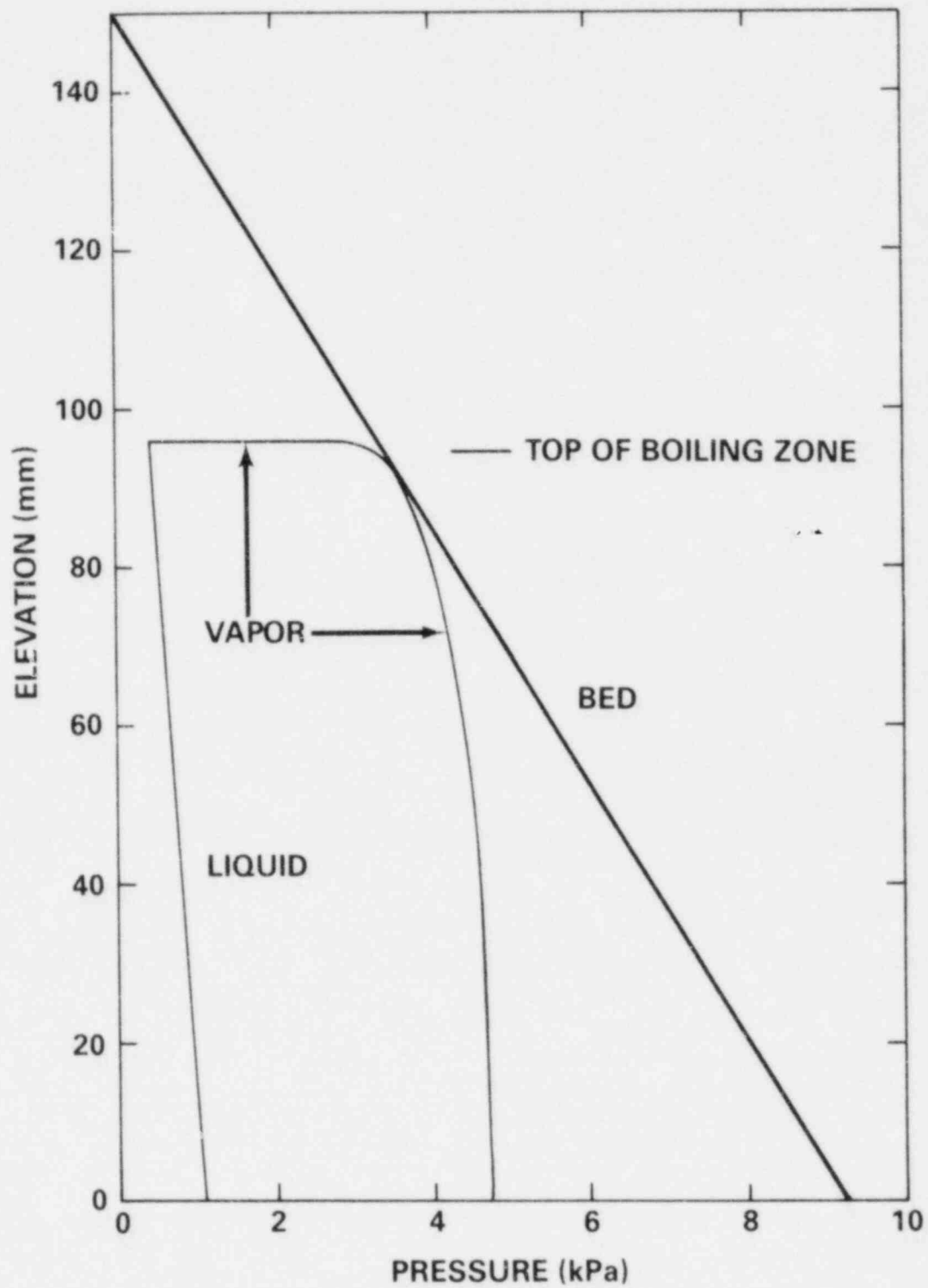


Figure 3-6. Pressure in the Vapor Liquid, and Bed Particles for a 150-mm thick Subcooled Bed With 67 W/kg- UO_2 . Zero pressure is at the top of an overlying subcooled zone assumed to be 54 mm thick.

large or small particles, with or without inlet flow, and with or without bottom cooling.

The basic equations for the model are Equations (3-21), (3-13), (3-26), and (3-28):

$$\begin{aligned}
 & - \frac{\sqrt{150} \cos \theta \sigma (1 - \epsilon) dJ ds}{\epsilon d} - \sqrt{150} \cos \theta \sigma J \frac{d}{dz} \left(\frac{1 - \epsilon}{\epsilon d} \right) + (\rho_l - \rho_v)g \\
 & = \frac{1.75(1 - \epsilon)q^2}{\epsilon^3 d h_{lv}^2} \left(\frac{1}{\rho_v(1 - s)^3} + \frac{1}{\rho_l s^3} \right) \\
 & + \frac{150(1 - \epsilon)^2 q}{\epsilon^3 d^2 h_{lv}} \left(\frac{\mu_v}{\rho_v(1 - s)^3} + \frac{\mu_l}{\rho_l s^3} \right) \\
 & + \frac{(1 - \epsilon)w}{\epsilon^3 d \rho_l s^3} \left(\frac{1.75 w}{h_{lv}} + \frac{3.5q}{h_{lv}} - \frac{150(1 - \epsilon)\mu_l}{d} \right)
 \end{aligned}$$

$$\text{for } q > wh_{lv} \quad (3-21)$$

where J is the Leverett function, and is suggested to be

$$J = \frac{(s-1 - 1)^{0.175}}{\sqrt{5}} \quad (3-13)$$

Equation (3-21) applies only to the packed boiling zone in the bed.

If the bed is channeled, the saturation at the top of the packed region is defined as

$$\frac{(1 - \epsilon)q_c}{\epsilon^3 d \rho_v g h_{1v}(1 - s)^3} \left(\frac{1.75 q_c}{h_{1v}} + \frac{150(1 - \epsilon)\mu_v}{d} \right) = \rho_p(1 - \epsilon) + \rho_l \epsilon \quad (3-28)$$

where q_c is the heat flux at the base of the channels, whose length is

$$L_c = \frac{\sqrt{150} \cos \theta \sigma J}{\epsilon d (\rho_p - \rho_l) g} \quad (3-26)$$

The model is assumed inapplicable if the channel length exceeds half the bed thickness. If the bed is subcooled, channel suppression may occur, as described in Section 3.3.2.

The predictions of the model (such as bed saturation, dryout power, dry zone thickness, downward boiling, etc.) and comparison with data will be discussed in the following two chapters. Simplification of the equations (with some loss of information) will be made in Chapter 6.

4. MODEL FEATURES FOR A UNIFORM BED ON AN ADIABATIC IMPERMEABLE PLATE

Numerical solution of Equation (3-21) under various conditions yields predictions of bed behavior. These predictions will be graphed in various formats to obtain a physical understanding of the consequences of the model. The predictions will also be compared with those of other models and with data.

The simplest case to consider is that of a uniform bed on an adiabatic impermeable plate. In this case the net flow through the bed is zero ($w = 0$) and zero heat flux ($z = 0$) occurs at the bottom of the bed. This case is more conservative (with respect to heat removal) than cases with a bottom-cooled plate or inlet flow at the bed bottom. In addition, nearly all of the heat removal experiments have been performed under these conditions. Thus only this case will be considered in this chapter. Other cases will be considered in Chapter 5.

4.1 Channel Length

The channel length at the top of the bed establishes the thickness of the remaining packed region, to which Equation (3-21) applies. Thus the channel length should be studied first. The channel length as a function of particle diameter is shown in Figure 4-1 for a sodium-UO₂ bed 150-mm thick with 40 percent porosity. The power is held constant at 330 W/kg-UO₂ (2.00 MW/m³). Also shown for comparison are the channel lengths predicted by Jones and Baker [31] (Equation 2-27), by Schwalm and Nijsing [43] (Equation 2-27, using $s = 0.5$) and by Reed [49] (Equation 2-31 with $\cos \theta = 1$). All yield similar results and vary inversely with the first power of particle diameter.

The channel length as a function of power is shown in Figure 4-2 for the same conditions but with particle diameter held at 0.3 mm. The other three models are also shown. Only the present model predicts a channel length dependent on bed power because of the increasing capillary force with increasing vapor fraction. However, the Jones-Baker model is a good approximation of the solution to Equations (3-26) and (3-28) for most powers.

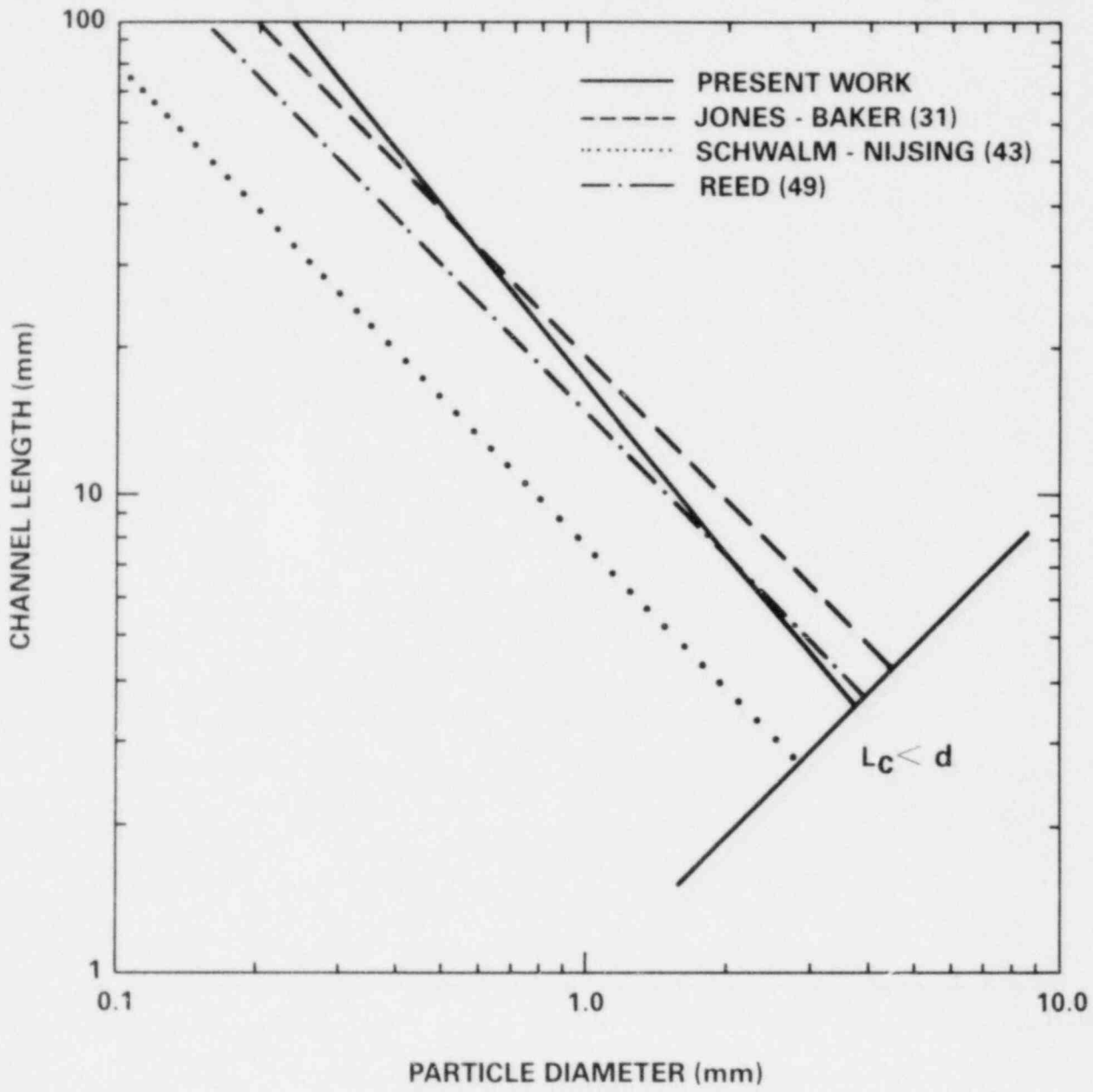


Figure 4-1. Channel Length vs. Particle Diameter for a Sodium- UO_2 Bed 150 mm Thick With 40% Porosity and 330 W/kg- UO_2 (2.00 MW/m^3).

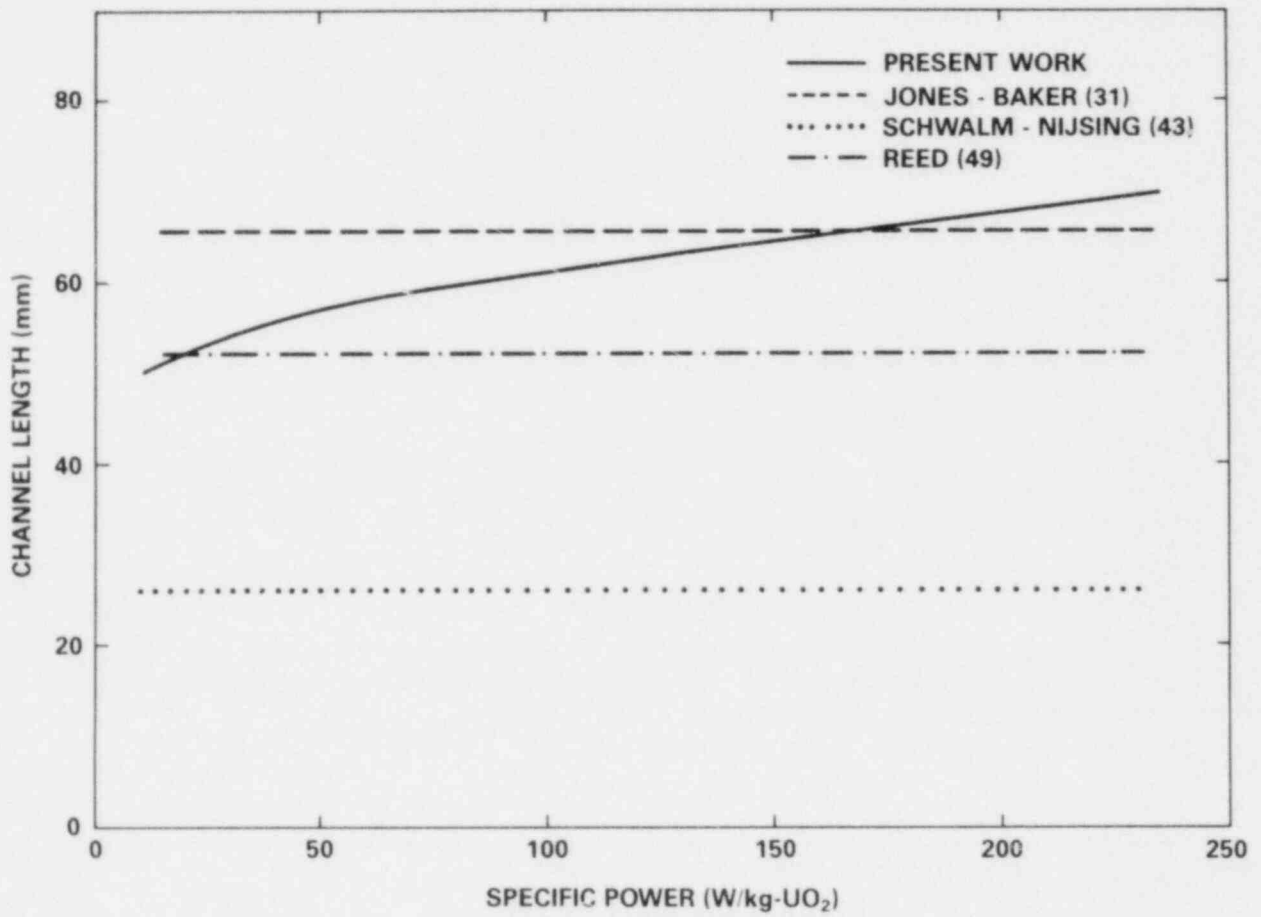


Figure 4-2. Channel Length vs. Power for Previous Bed With 0.3 mm Particle Diameter.

4.2 Liquid Fraction in the Bed

Figure 4-3 a shows the effective saturation in a bed for various powers, using Equations (3-20), (3-28), and (3-30). The bed is a non-subcooled uniform sodium-UO₂ bed 150-mm thick with 0.3-mm diameter particles and 40 percent porosity.

As the power increases, the average saturation decreases. However, note that the local saturation increases with increasing elevation. This is contrary to what occurs in a volume-heated boiling pool (in which the vapor fraction increases with elevation), and implies that the local vapor velocity increases with elevation. This effect is due to capillary force, as was described in Section 3.1.

Figure 4-3b shows the saturation in a bed similar to that in Figure 4-3a except with a particle diameter of 3.0 mm. Note that the saturation increases with elevation only in the top portion of the bed. Below about 130 mm, the trend is reversed, yielding a minimum in the saturation at that elevation. This is because capillary force is weaker with larger particles (see Equation 3-16). Thus below a certain elevation gravity overcomes capillary force and the bed behaves more like a volume-heated boiling pool. By this reasoning one would also expect a saturation minimum and trend reversal in a bed with small particles if the bed were thick enough. Indeed, the bed in Figure 4-3a shows a slight minimum and would show a distinct minimum if it were considerably thicker. Such a minimum may be easily looked for in an experiment.

The distance of the saturation minimum below the base of the channels is a function of bed and fluid parameters, as well as power. This distance depends on capillary force and is normally less than the "capillary head", defined as the distance liquid would be drawn up from below into a very thick dry bed. Using Kozeny's [5] value for total capillary pressure in a bed of spheres, the capillary head is

$$\lambda_c = \frac{6\sigma \cos \theta (1 - \epsilon)}{\epsilon d(\rho_l - \rho_v)g} \quad (4-1)$$

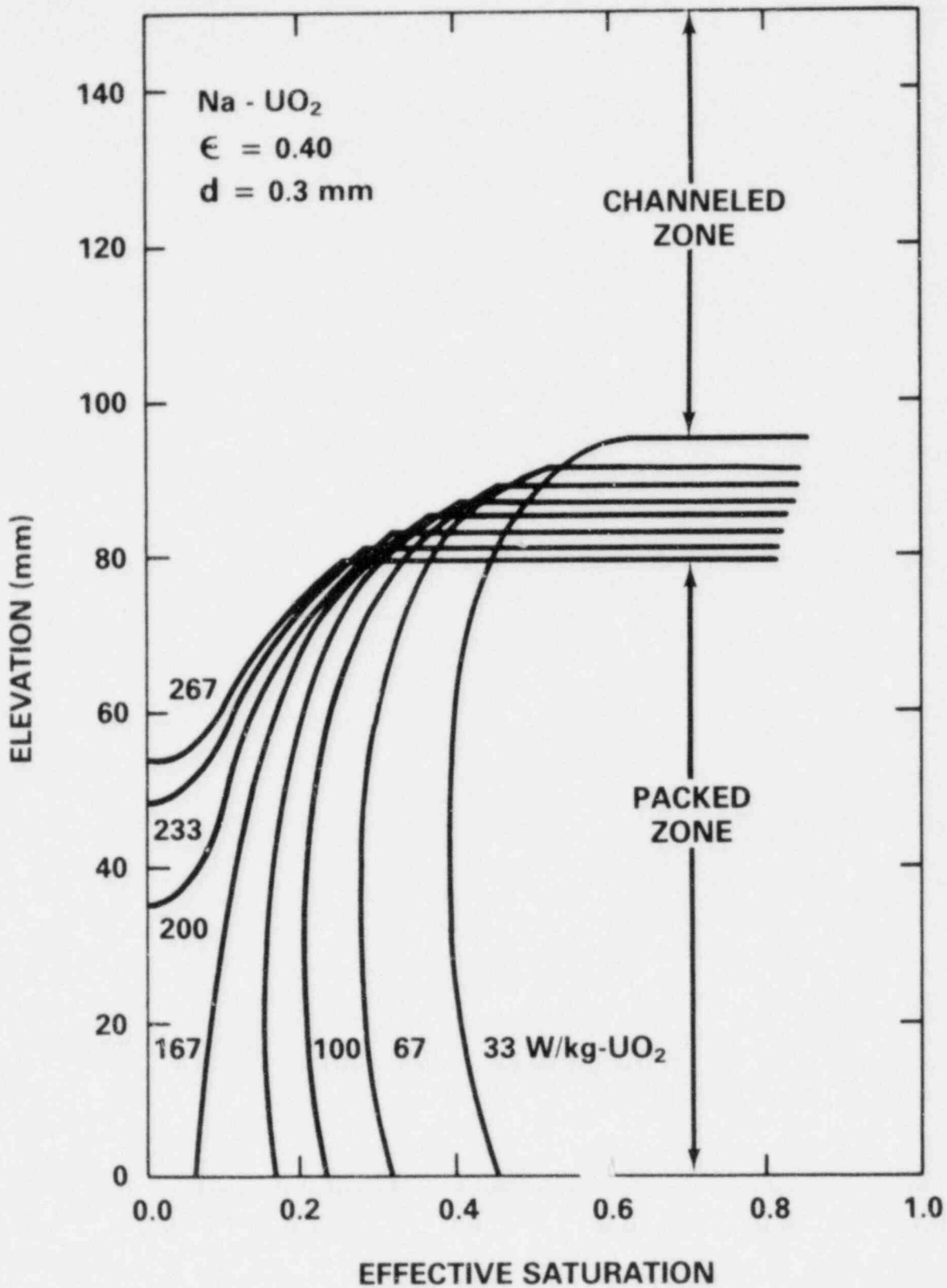


Figure 4-3a. Effective Saturation vs. Elevation for Various Powers in a Non-Subcooled Sodium-UO₂ Bed 150 mm Thick With 40% Porosity and 0.3 mm Diameter Particles

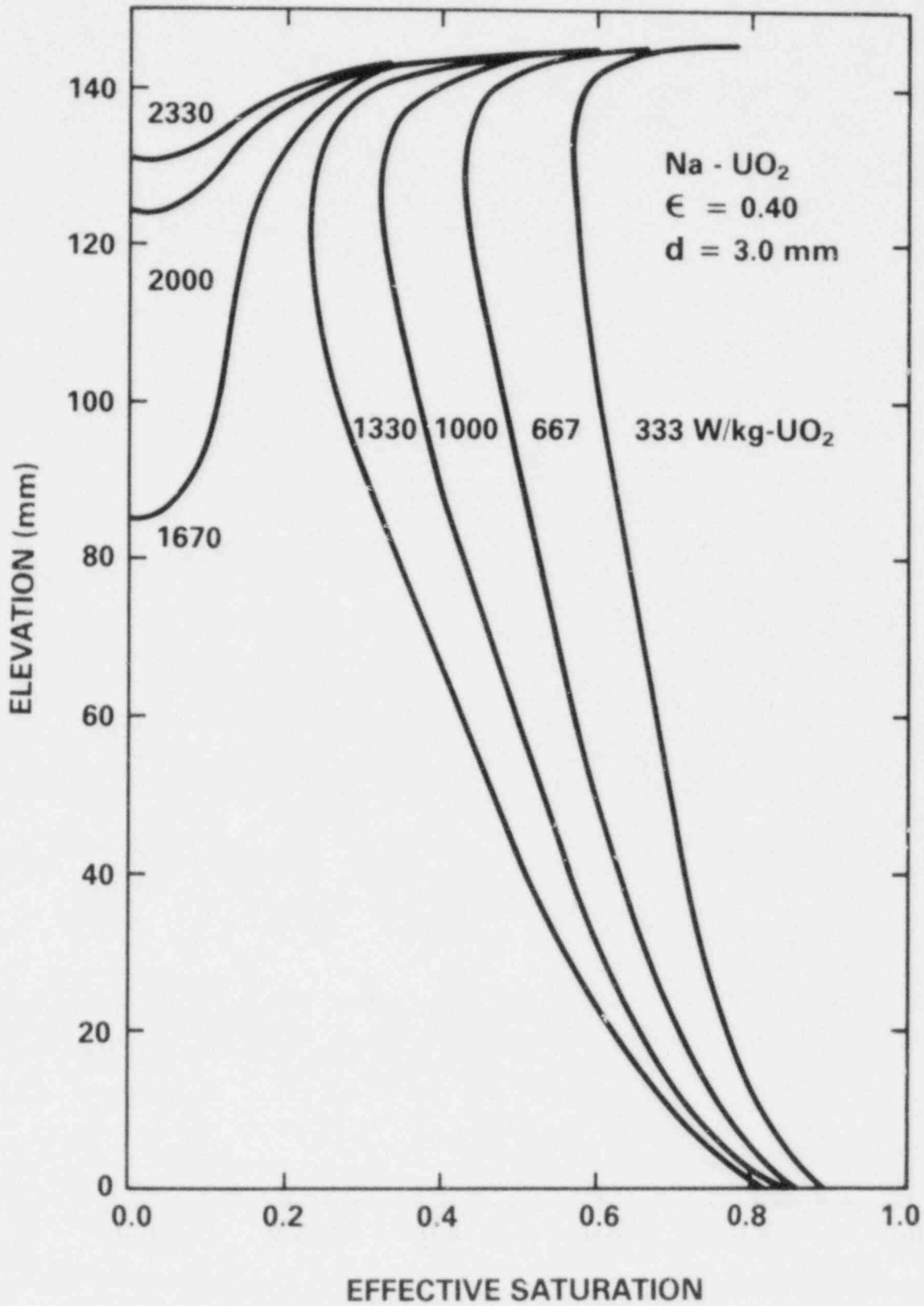


Figure 4-3b. Effective Saturation in a Bed With 3.0 mm Diameter Particle

For the beds in Figures 4-3a and 4-3b, the capillary heads are 492 mm and 49 mm, respectively. The observed minimums near dryout are about 80 mm and 20 mm, respectively, below the base of the channels.

One may integrate under the curve in Figures 4-3a and 4-3b and divide by the packed boiling length to obtain the average effective saturation s_{ave} . One may relate this to the average vapor fraction (in the packed region) by

$$\alpha_{ave} = (1 - s_r)(1 - s_{ave}) \quad (4-2)$$

where s_r is given by Equation (3-3).

A comparison between predicted and measured vapor fraction is shown in Figure 4-4 for a water-bronze bed from reference 53. The agreement is fairly good. The predicted vapor fraction with the linear relative permeability used in reference 27 is also shown (dashed line). This demonstrates the sensitivity of the vapor fraction to relative permeability.

4.3 Incipient Dryout

At a power of 200 W/kg-UO₂ in Figure 4-3a, the saturation reaches zero above the bed bottom. This indicates two things. First, the incipient dryout power is between 167 W/kg-UO₂ and 200 W/kg-UO₃. Thus the one-D model can predict the incipient dryout power. Secondly, there is a steady-state condition in which the bed bottom is dry but the rest of the bed is still boiling. In this state, the heat from the dry zone is assumed to be delivered by some means (most likely by conduction and radiation) to the base of the boiling zone. (This is demanded by Equation (3-19)). Thus the one-D model predicts existence of a steady dry zone and predicts the dry zone thickness as a function of power above dryout. It is presently the only physically-based model to do so. The characteristics of the conditions required for incipient dryout will now be considered.

The conditions required for dryout involve bed thickness, bed porosity, particle density, particle diameter, liquid and vapor densities and viscosity, heat of vaporization, surface tension, and bed power. It is

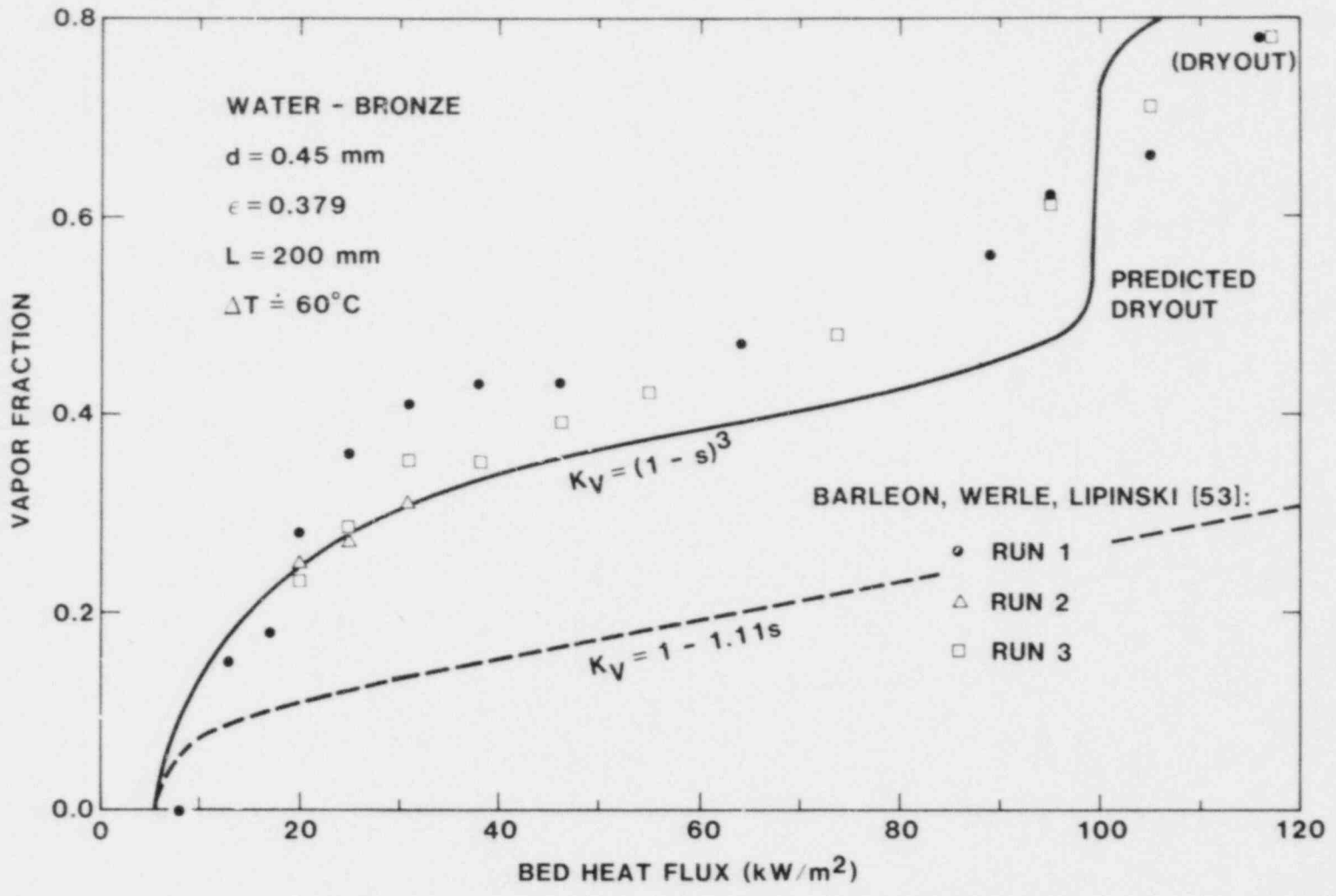


Figure 4-4. Predicted and Measured Vapor Fraction

customary to consider the heat flux leaving the surface of the bed as the dependent variable and everything else as independent variables. The dryout flux (or incipient dryout heat flux) is the bed heat flux at steady-state conditions just barely severe enough to cause part of the bed to become dry. The bed heat flux may be converted to average bed volumetric power by dividing by the bed thickness, or to specific power by dividing by the bed loading (kg/m^2). An advantage to using dryout flux instead of dryout power (or specific power (J/kg)) is that the dryout flux depends less strongly on bed thickness than dryout power does.

Determining the dryout flux with the present model requires solving the differential equation (3-21) several times until both the top channel boundary condition and the bottom dryout ($s=0$) condition are achieved. This makes the model somewhat cumbersome to use. An algebraic zero-D model will be developed in Chapter 6 as an alternative.

4.3.1 Dryout Flux vs. Particle Diameter

The characteristics of the dryout heat flux predicted by the one-D model may best be depicted by a series of graphs. Figure 4-5a displays the dryout flux vs. particle diameter with (non-subcooled) sodium at one atmosphere pressure for a bed porosity of 40 percent. (Although bed permeability is strongly dependent on particle diameter, bed porosity is usually independent of particle diameter, and is assumed constant in this figure.) Various bed thicknesses are considered. As throughout this chapter, the bed is uniform and on an adiabatic impermeable plate.

Various regions are apparent. For very small particles channels dominate in the bed and the slope in the curves is nearly zero. (When channels penetrate more than half the bed thickness, the model is assumed inapplicable.) For slightly larger particles the dryout flux varies with the first power of particle diameter. Typically this applies to beds thinner than the capillary head (Equation 4-1) but much greater than a channel length. For medium-sized particles and very deep beds the dryout flux varies with the square of the particle diameter. In this case, the capillary force is negligible and the flow is laminar. For large particles the slope is one-half and the dryout flux depends on the square root of particle diameter. All of these different particle diameter dependencies are included

in the model (Equation 3-21). Early models [1,7,8,20] included only the square (deep-bed laminar) dependence or square-root (turbulent) dependence and thus would be subject to large errors if used outside their ranges of applicability.

Figures 4-5b through 4-5g display similar plots for water, acetone, methanol, freon-113 and isopropanol (all at atmospheric pressure). The influence of capillary force in the last four fluids is small. Thus caution must be used in extending results obtained with those fluids to water or sodium.

Figure 4-6a compares the various dryout models in a plot similar to Figure 4-5a, but with a single bed thickness of 100 mm. (Only one flooding model, the one by Sowa, et al. [1], is shown. The others are very similar.) There are large differences in the predicted dryout fluxes, especially for very large and very small particles. None of the early models were made general enough to include both turbulence and laminar flow. The Shires-Stevens model was the first to include the capillary effect (for small particles). The present model is very close to the Lipinski early zero-D model with respect to dryout predictions.

Figure 4-6b is a similar plot, but with water and a bed thickness of 500 mm. In this case note that in the water plot nearly all the models intersect in the region from 0.3 mm to 2.0 mm diameter particles. This is partly due to the fact that at the time most of the early models were developed, all of the dryout measurements were for water with particles 0.3 mm to 1.0 mm in diameter, leading to a selection of models which fit the data (survival of the "fittest"). Even for moderately small particles of 3 mm (such as might be found after thermal fracture of fuel pellet), the difference between the predicted dryout flux of the laminar models and the present model is up to a factor of ten. Thus use of the proper model in these cases is important.

Figure 4-7 shows the dryout flux for water-bronze beds, 100-mm thick compared with the dryout data of Barleon and Werle [33,52]. The porosity in their beds varied with particle diameter:

$$\epsilon = 0.373 + 6.3 d \quad (4-3)$$

SODIUM

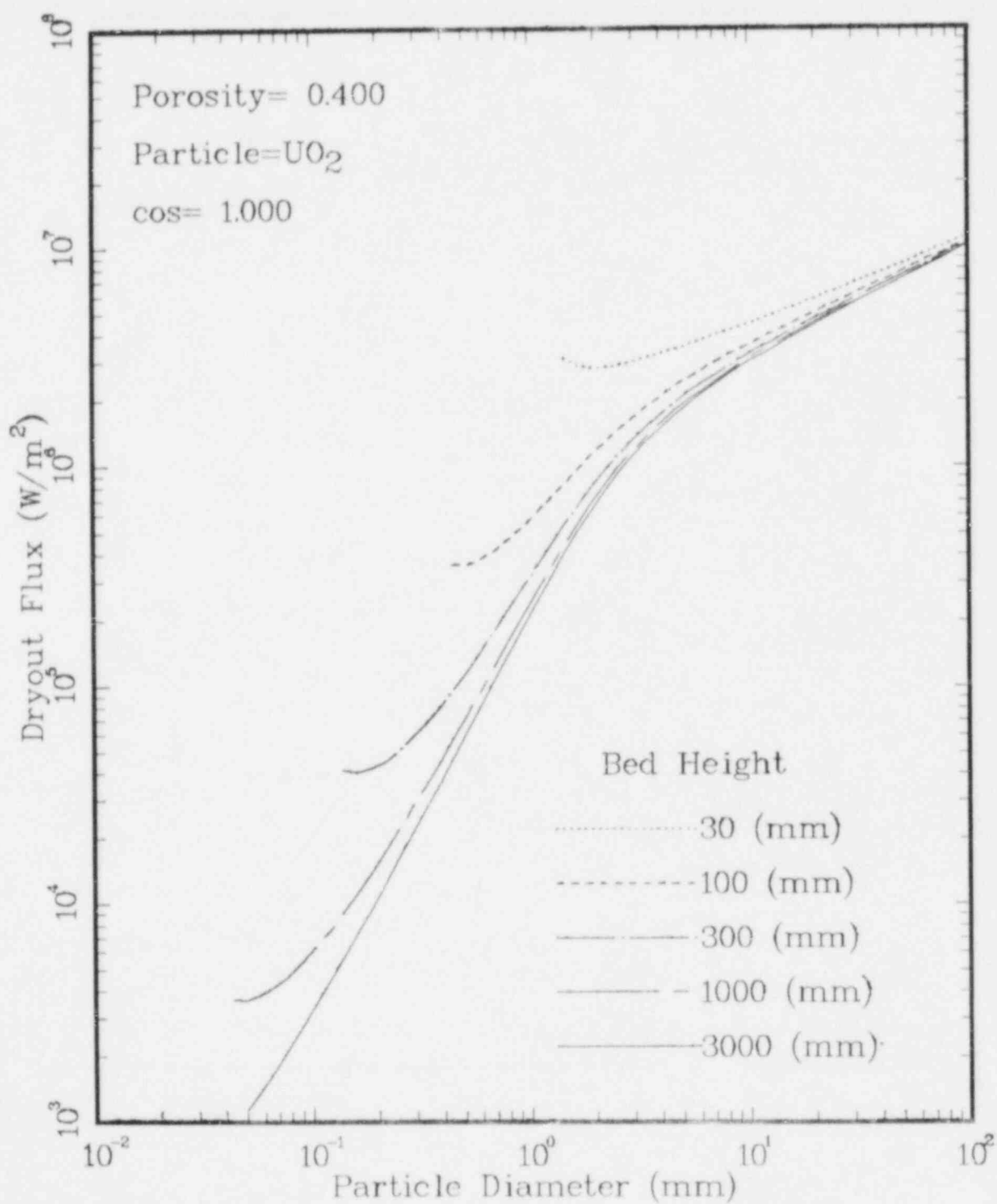


Figure 4-5a. Dryout Flux vs. Particle Diameter for Beds With 40% Porosity and Various Thickness. The beds are sodium-UO₂.

WATER

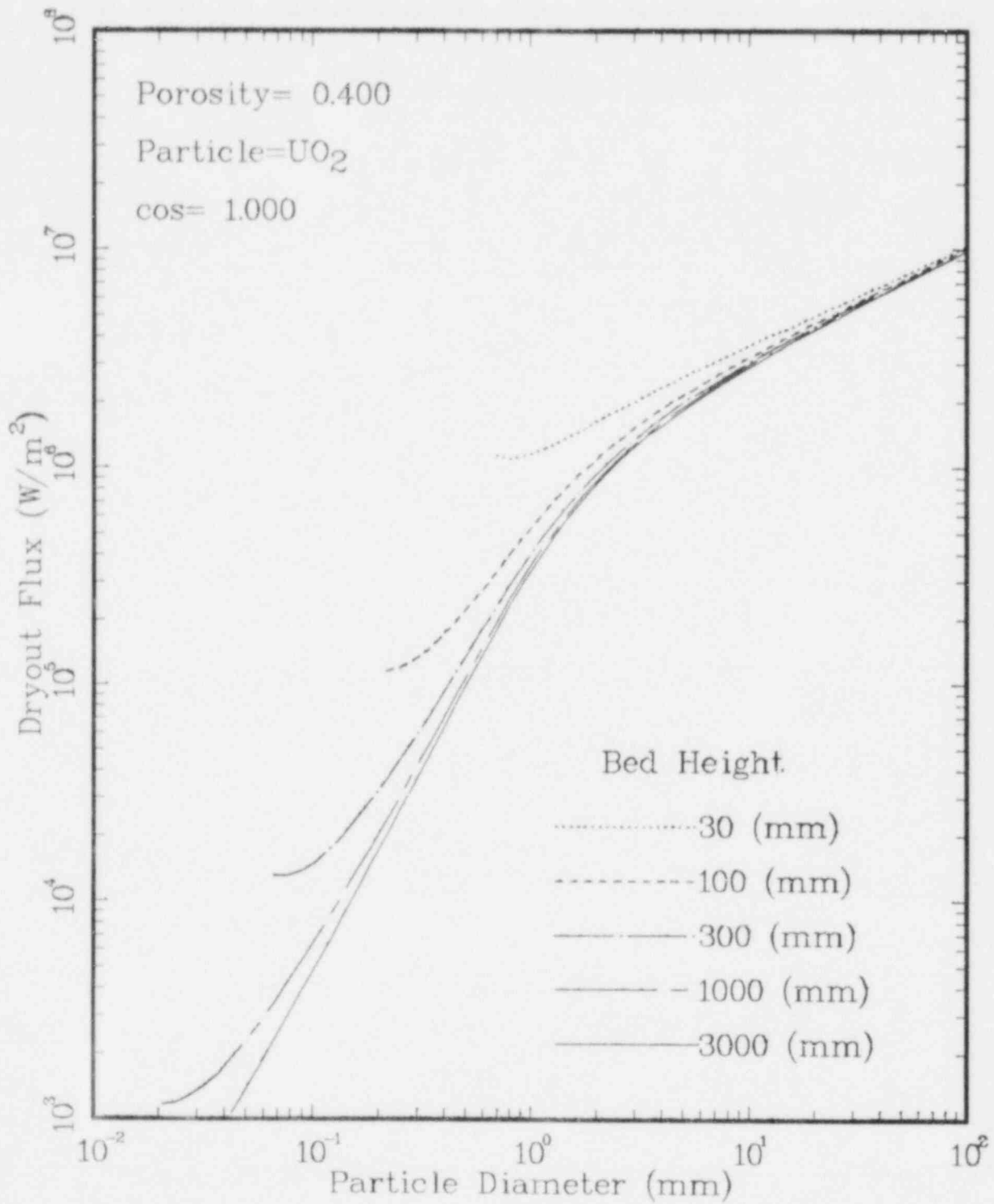


Figure 4-5b. Dryout Flux vs. Particle Diameter for Beds With 40% Porosity and Various Thickness. The beds are water-UO₂.

WATER

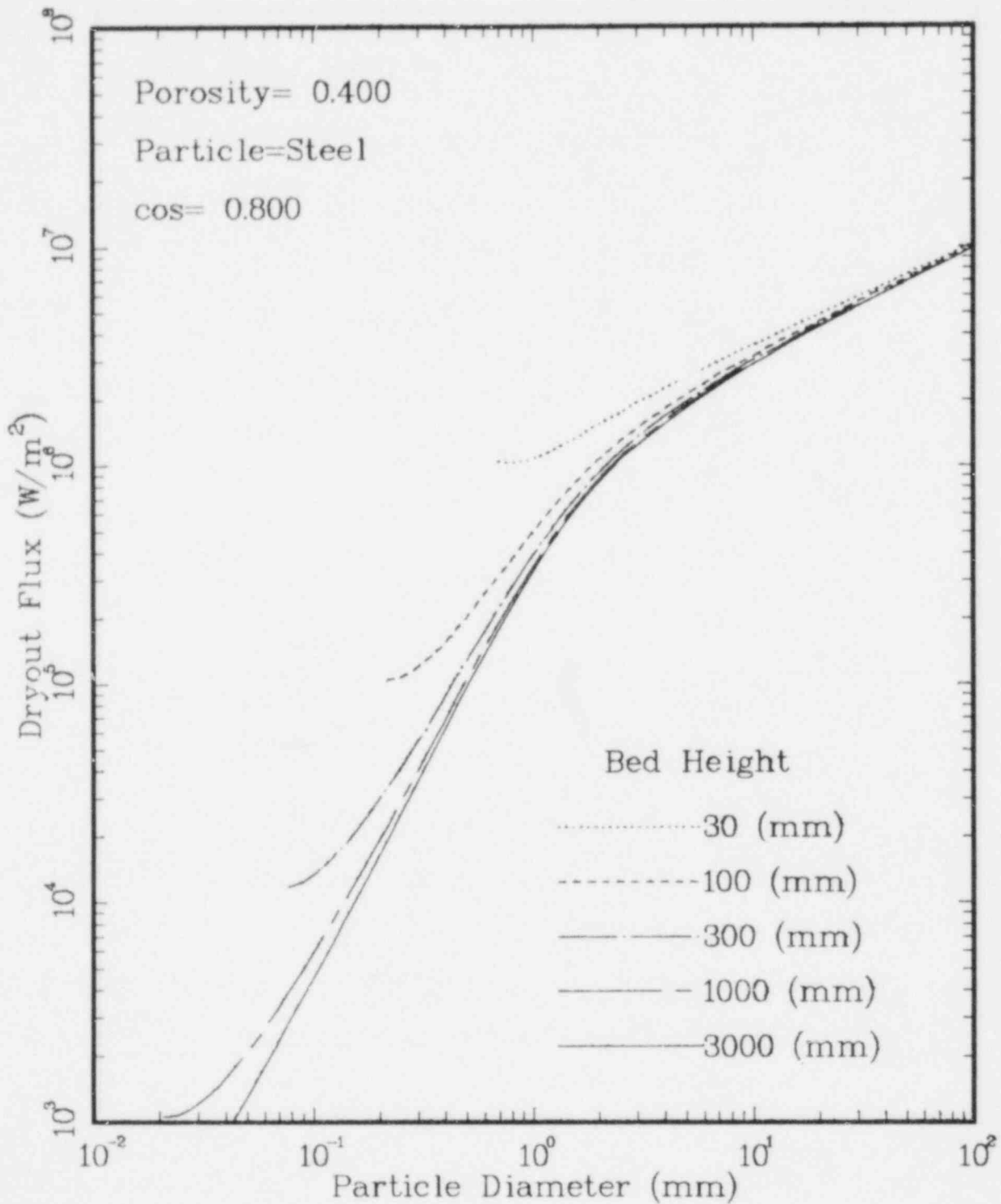


Figure 4-5c. Dryout Flux vs. Particle Diameter for Beds With 40% Porosity and Various Thickness. The beds are water-steel.

ACETONE

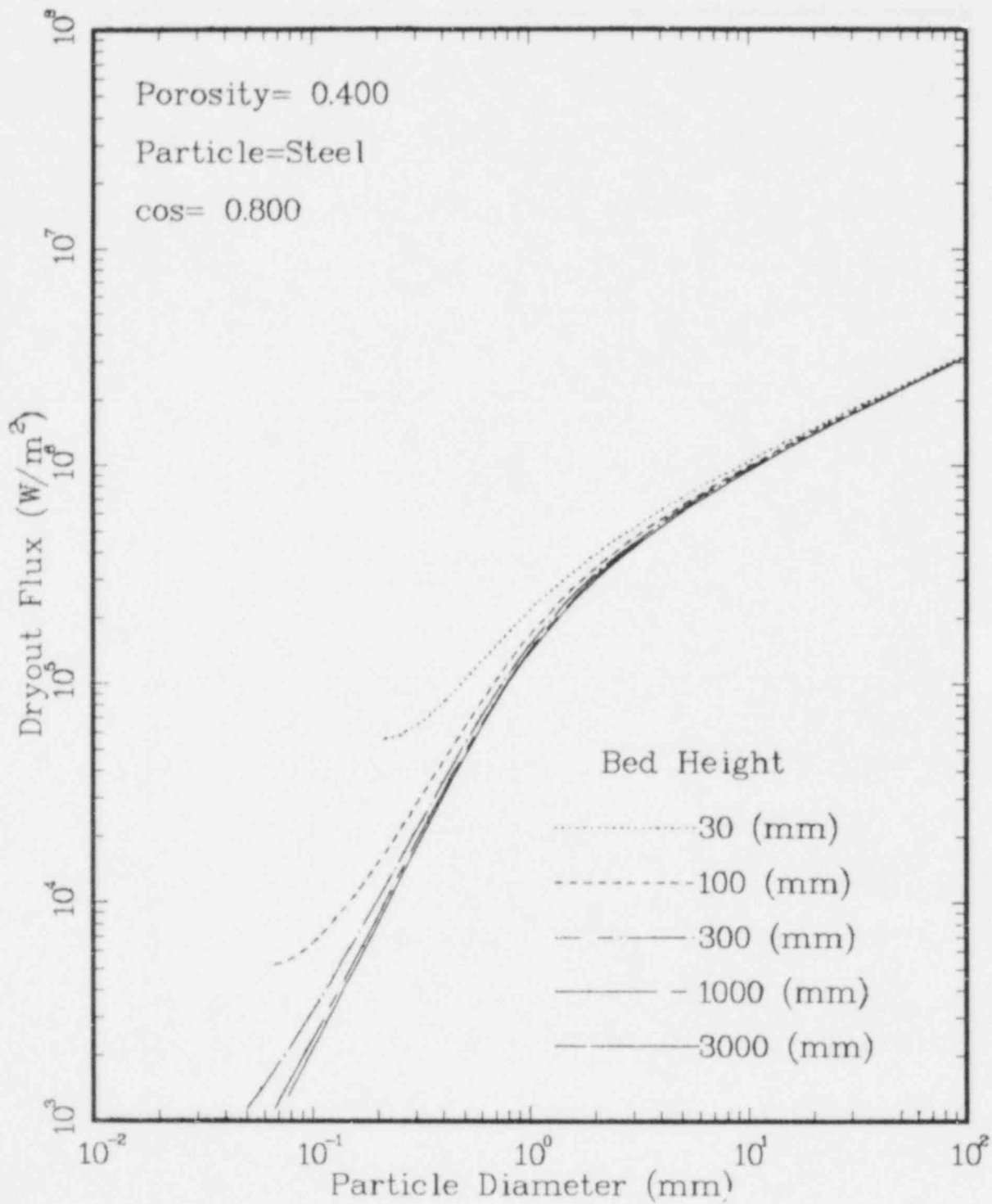


Figure 4-5d. Dryout Flux vs. Particle Diameter for Beds With 40% Porosity and Various Thickness. The beds are acetone-steel.

METHANOL

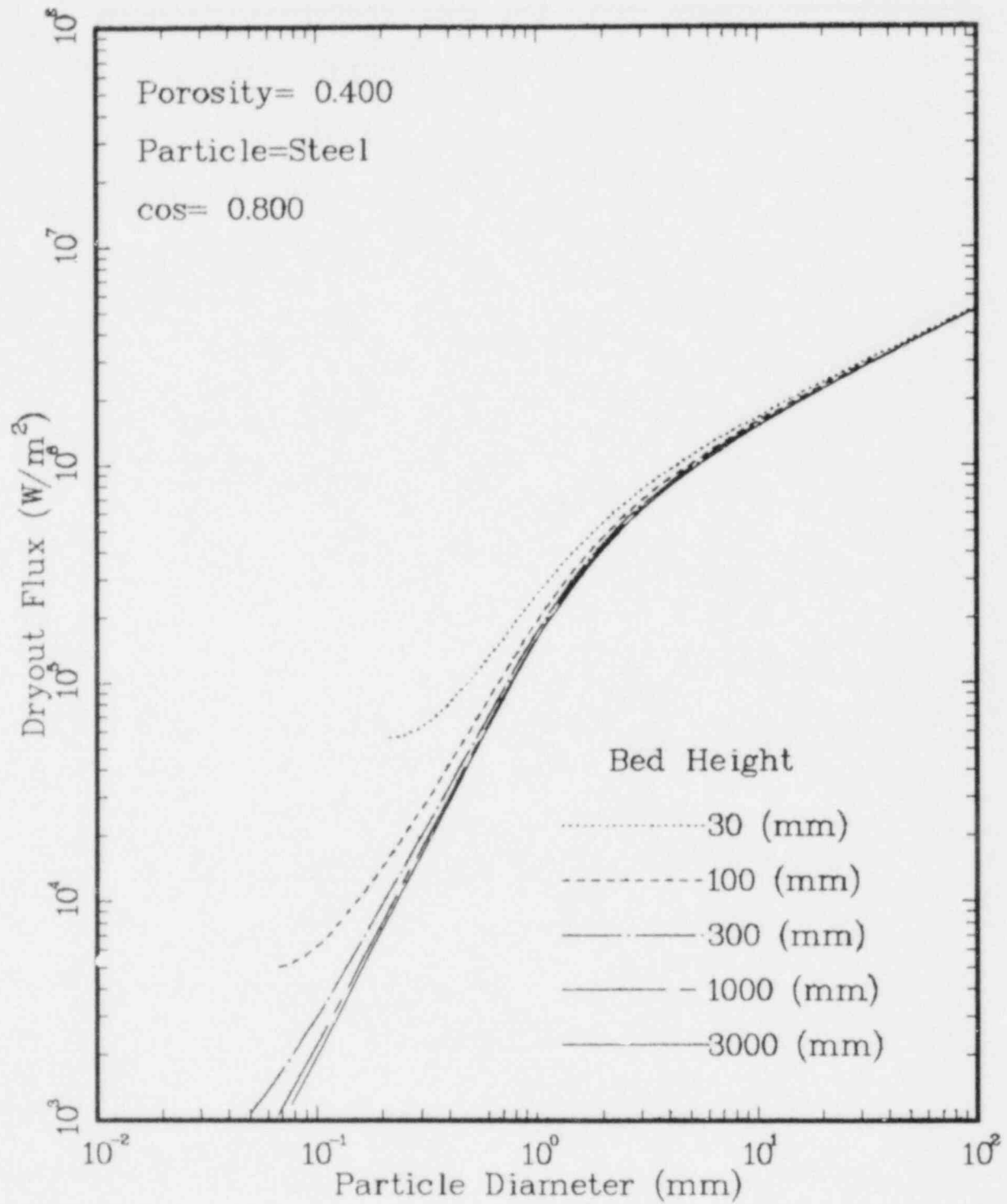


Figure 4-5e. Dryout Flux vs. Particle Diameter for Beds With 40% Porosity and Various Thickness. The beds are methanol-steel.

FREON-113

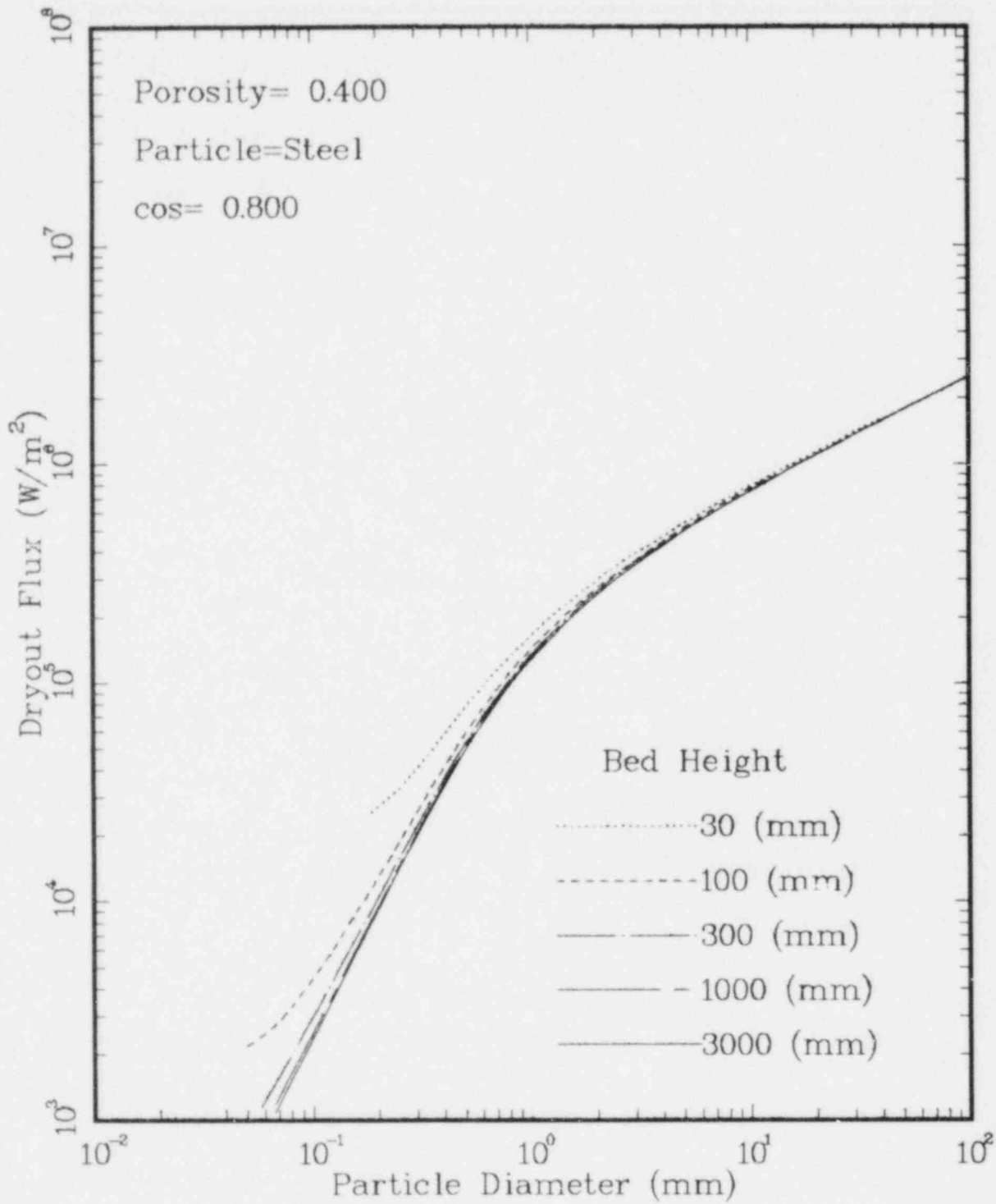


Figure 4-5f. Dryout Flux vs. Particle Diameter for Beds With 40% Porosity and Various Thickness. The beds are freon-113-steel.

ISOPROPANOL

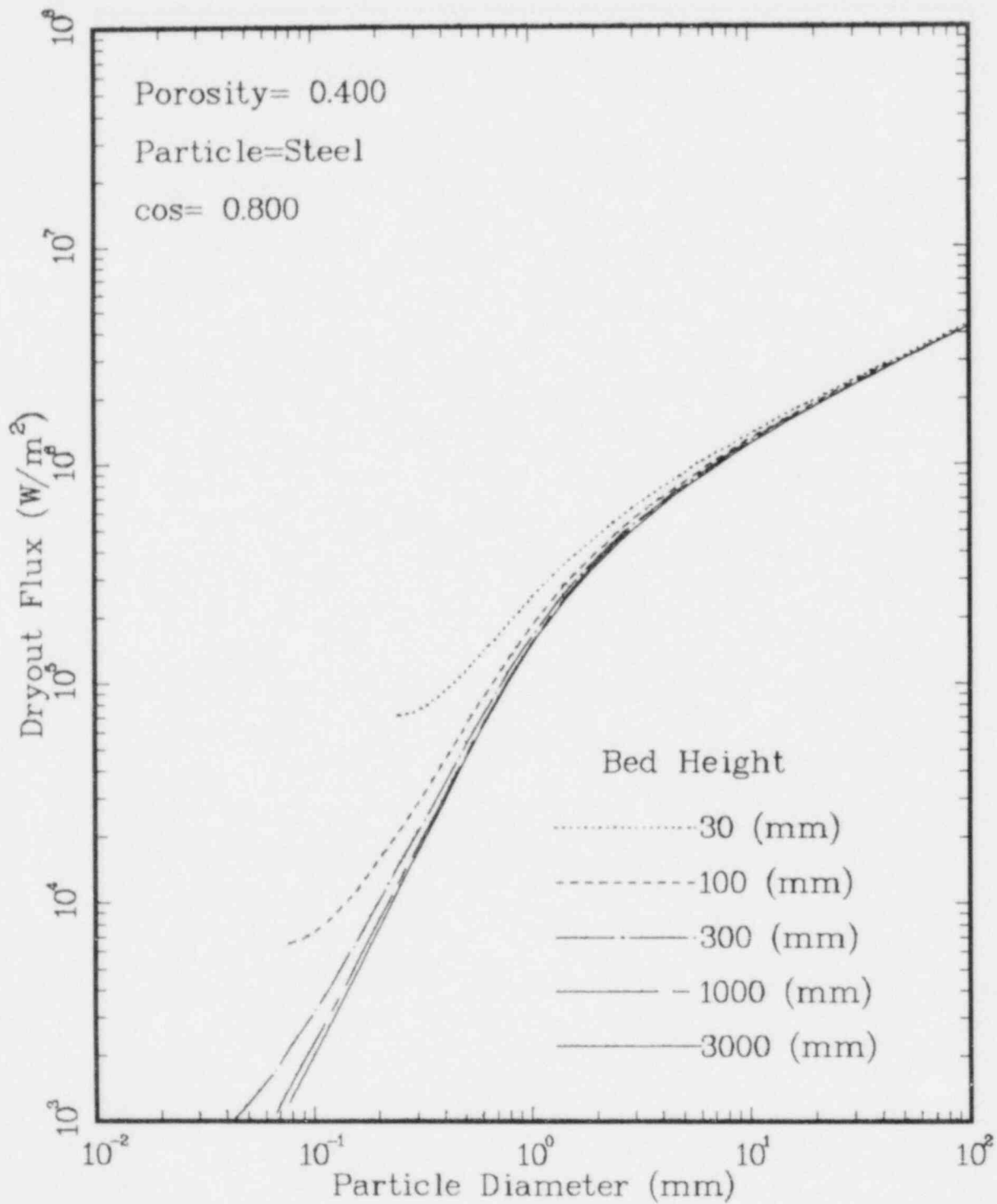


Figure 4-5g. Dryout Flux vs. Particle Diameter for Beds With 40% Porosity and Various Thickness. The beds are isopropanol-steel.

SODIUM

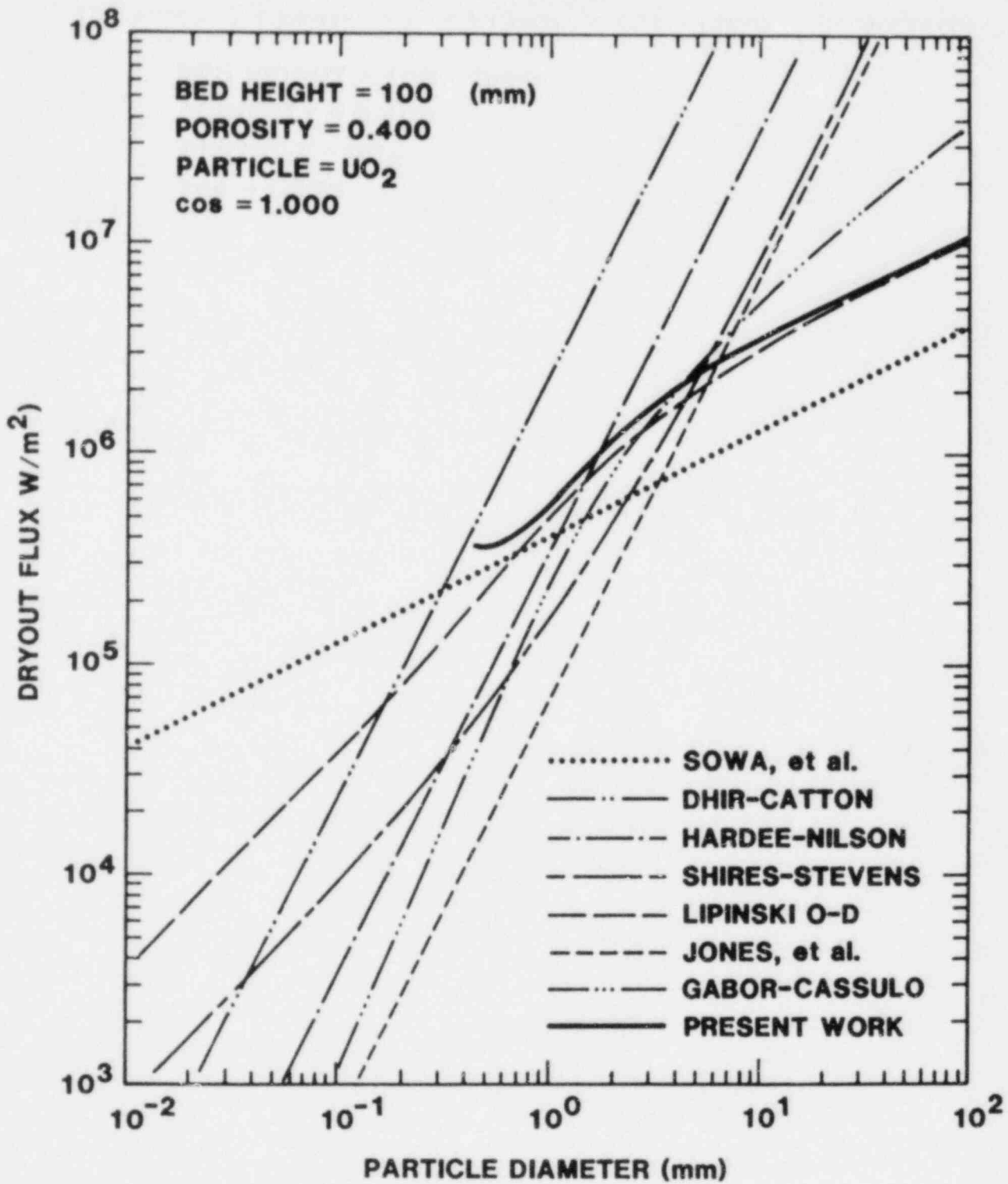


Figure 4-6a. Dryout Fluxes for Several Models:
(a) as in 4-5a, but With a 100-mm Thick Bed.

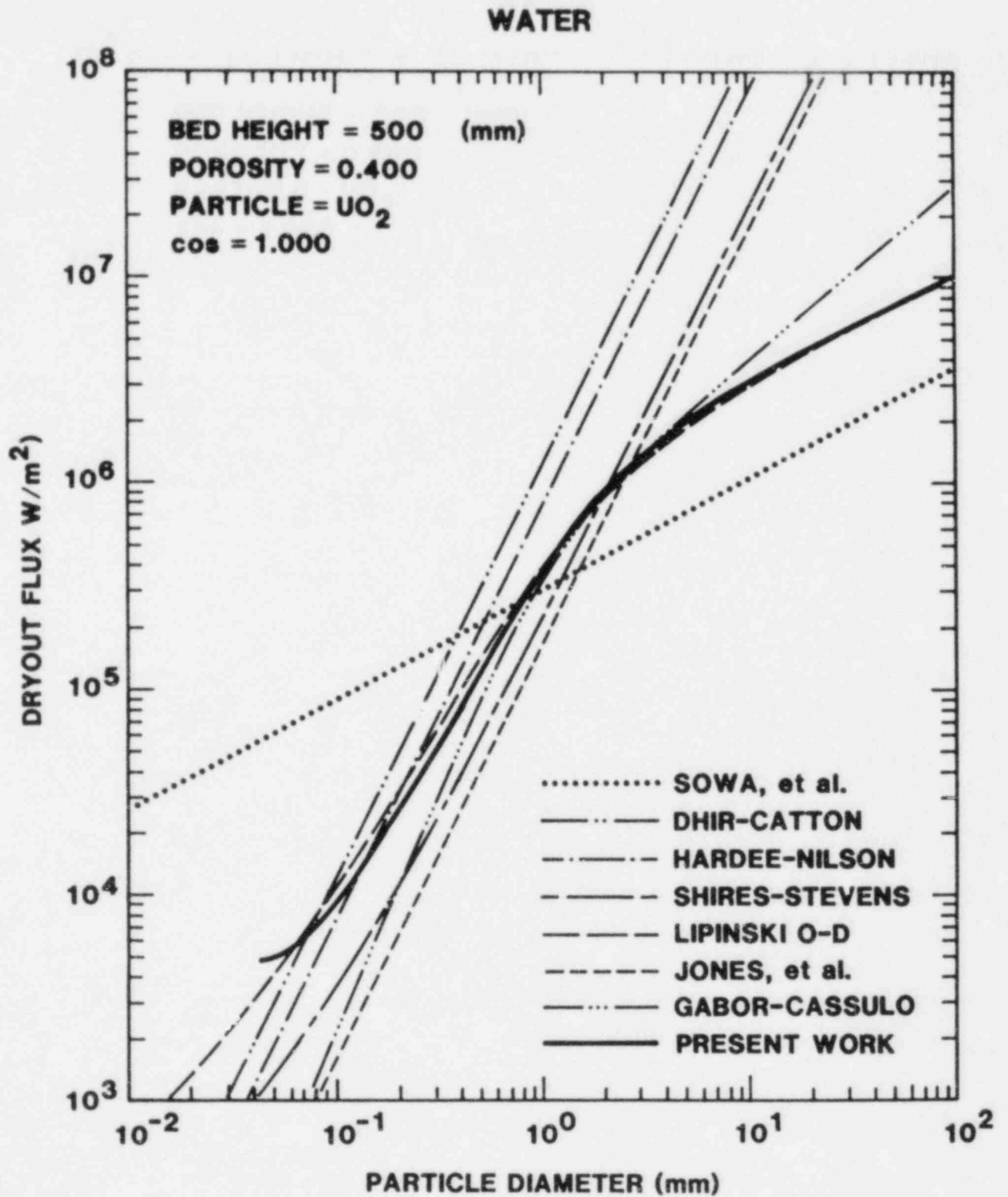


Figure 4-6b. Dryout Fluxes for Several Models: (b) as in 4-5b, but With a 500-mm Thick Bed.

where d is in meters. This formula was used in the plot. To avoid extremes in the figure, an upper limit to the porosity was set at 0.50. (This limit is outside of the range of the data.) The trend in the data clearly and the transition from laminar to turbulent behavior and the failure of laminar models in the turbulent region. In addition, the effect of capillary force and channels is evident for small particles. The agreement with both the present model and the zero-D model is good. (A more complete plot with all available dryout data will be presented later; at this time only trends in individual parameters will be presented.) Figure 4-8 shows a similar plot with freon. Again, the agreement with the present model is good. In this case the influence of capillary force and channels is not exhibited because of the low surface tension of freon.

Also shown in Figures 4-7 and 4-8 are the dryout fluxes for a flat plate according to Zuber [58] (Equation 2-5). It has been proposed [28,44] that the flat plate critical heat flux is a limit to the dryout flux in a volumetrically-heated particle bed. The data for both freon and water exceed this limit by factors of 4 and 5, respectively. Since both the method of vapor formation and the method of vapor release into the overlying pool are considerably different for a volumetrically-heated bed than for a flat plate, one should not expect a close relation between the dryout flux for a volumetrically-heated bed and that of a flat plate.

4.3.2 Dryout Flux vs. Bed Thickness

The dependence of heat flux on bed height by the various models is shown in Figure 4-9a for a water-steel bed with a particle diameter of 0.68 mm and a bed porosity of 40 percent. These conditions were chosen because much data for these conditions exist for comparison. Many of the models have no bed height dependence. The shallow bed model of Dhir and Carton can be seen becoming active for a bed height less than 33 mm. All the models with capillary force (Shires-Stevens, Lipinski zero-D, and the present work) show continuous bed height dependence. The present model predicts that with small bed heights (< 50 mm) the bed height dependence is strong due to the influence of channels. For medium heights ($50 < L < 500$ mm) the slope is less steep and due primarily to capillary

WATER

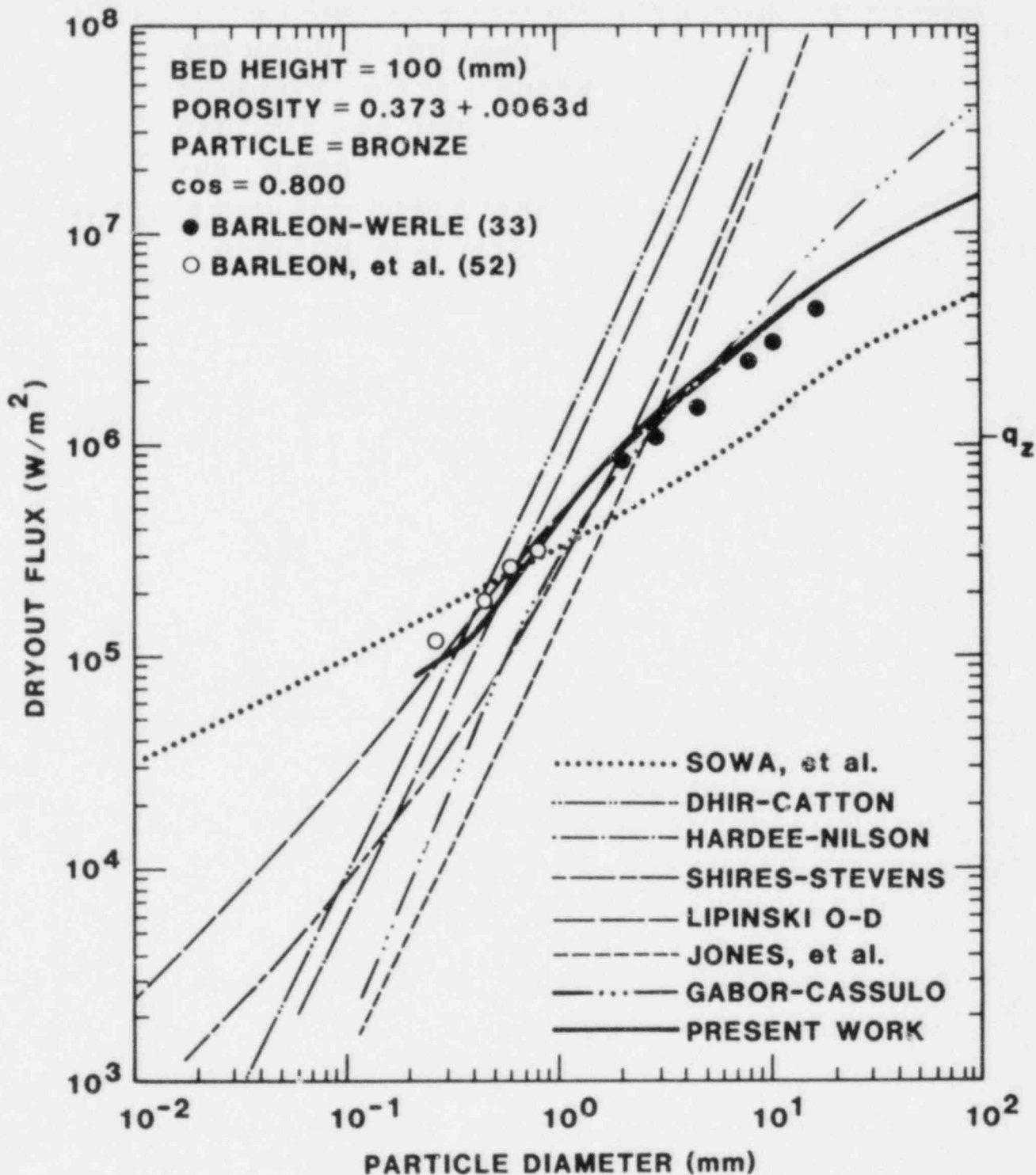


Figure 4-7. Predicted and Measured Dryout Fluxes for Beds With Bronze Particles and Water, 40% Porosity and 100 mm Thick. Various models and the data of Barleon and Werle [33,52] are shown.

FREON-113

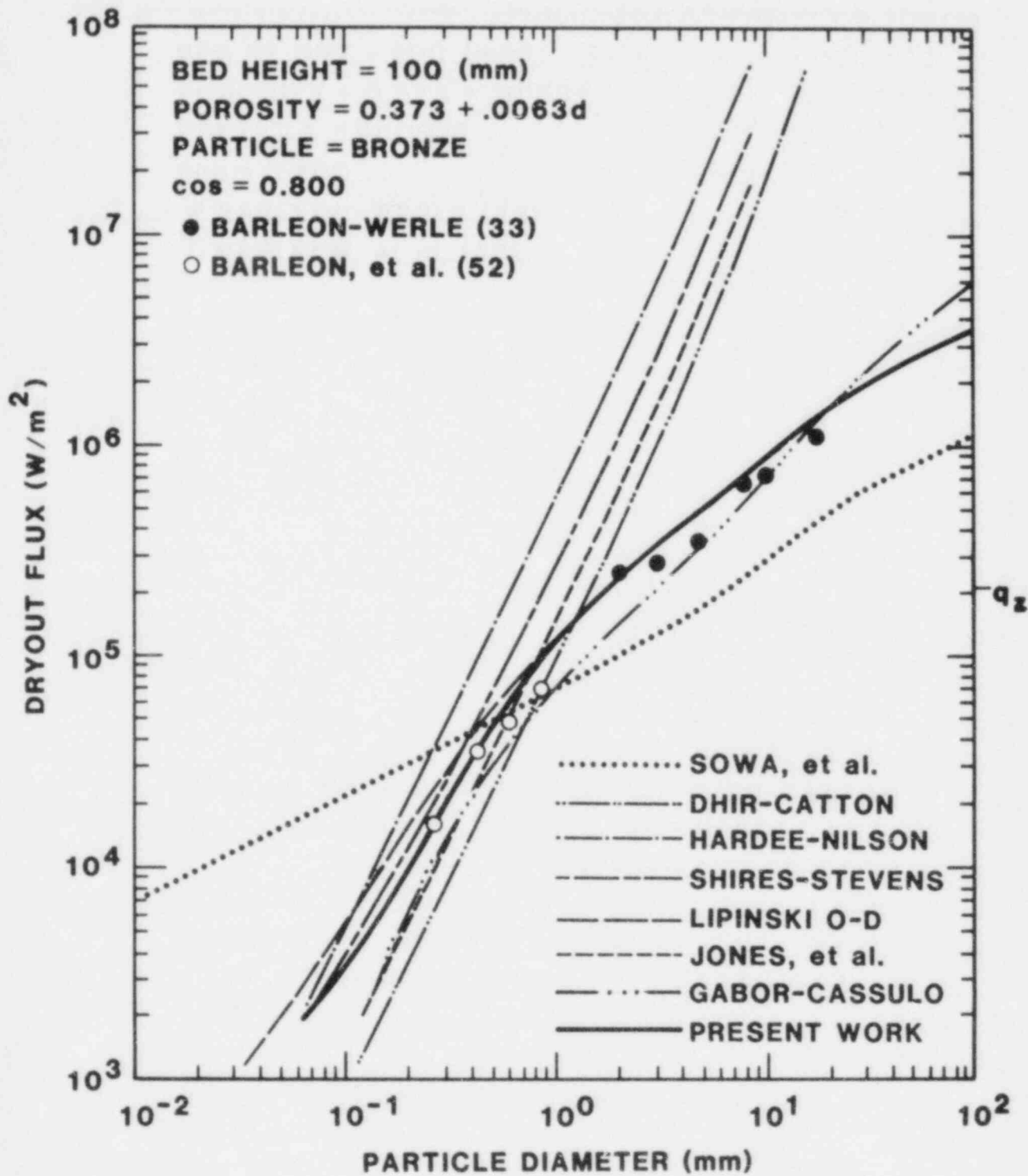


Figure 4-8. A Plot Similar to Figure 4-7, but With Freon-113.

force drawing the liquid into the bed. For large heights ($500 \text{ mm} < L$), the slope is near zero. In this region gravity is the primary force drawing liquid into the bed, and both the hydrostatic head and total flow resistance increase linearly with thickness. The three regions may be called channeled (or shallow), moderately deep, and very deep. The dryout predictions by the various models span a wide range, so comparison with data should easily indicate the best model.

Figure 4-9b shows the data from various researchers for the bed conditions in the plot. The data is widely scattered, spanning as much as a factor of six even for nearly identical conditions. The particle diameters used varied from 0.605 mm to 0.715 mm and the porosity from .38 to .42. This should introduce an error of less than $\pm 40\%$. Thus, the wide disagreement among the reported data must be due to different bed conditions not reported in the references, or possibly calibration errors. The scatter in the data makes it difficult to assess or refine the proposed dryout models.

In most cases the data from an individual reference show a decrease in dryout flux with bed heights, as predicted by the models with capillary force. But, the data is not accurate enough to distinguish channel effects from packed-bed capillary effects.

The scatter in the data may be due to calibration errors and radial heat loss. Of all the researchers, only Barleon and Werle both insulate their bed and overlying pool, and make corrections for heat losses. Even with insulation, the heat losses can be as high as 10 percent. Thus the accuracy of the data from experiments which are not insulated, in which heat losses are assumed negligible, and in which the beds are smaller in diameter (50 mm vs. 80 mm), is questionable. The data of Trenberth and Stevens may be exceptionally low because of their unusual method of heating the bed by a current running through it. Thus local tight packing will lead to reduced contact resistance between the particles and a local hot spot. This could lead to premature dryout. The data of Barleon and Werle agree fairly well with the present model predictions [52].

The acetone-steel data of Dhir and Catton [7] are compared with the models in Figure 4-10. As can be seen, the Dhir-Catton shallow and deep bed models (which were

WATER

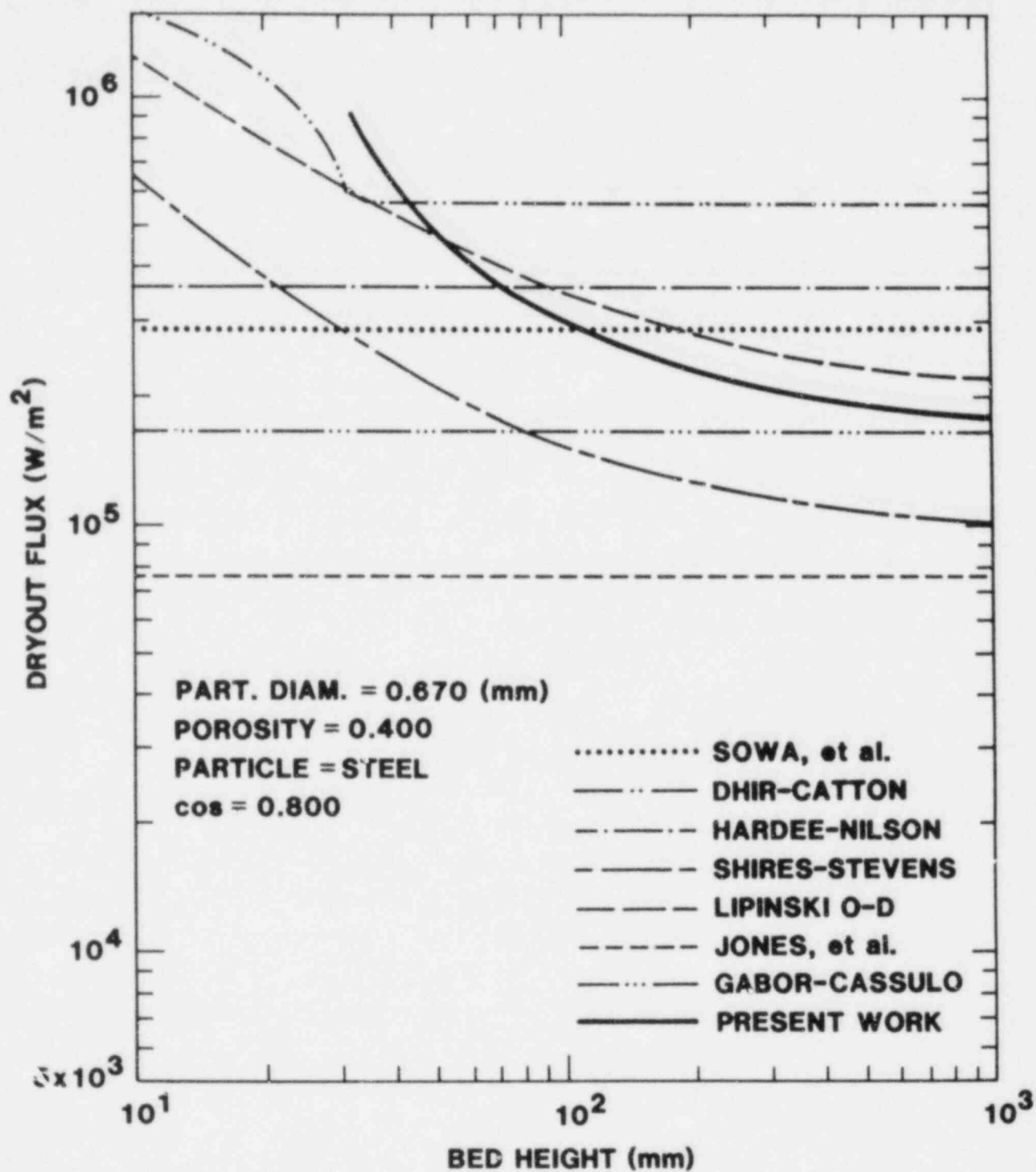


Figure 4-9(a). Dryout Flux vs. Bed Thickness for Various Models With a Water-Steel Bed With 40% Porosity and 0.68-mm Particle Diameter. The data of several references are shown in Figure 4-9b.

WATER

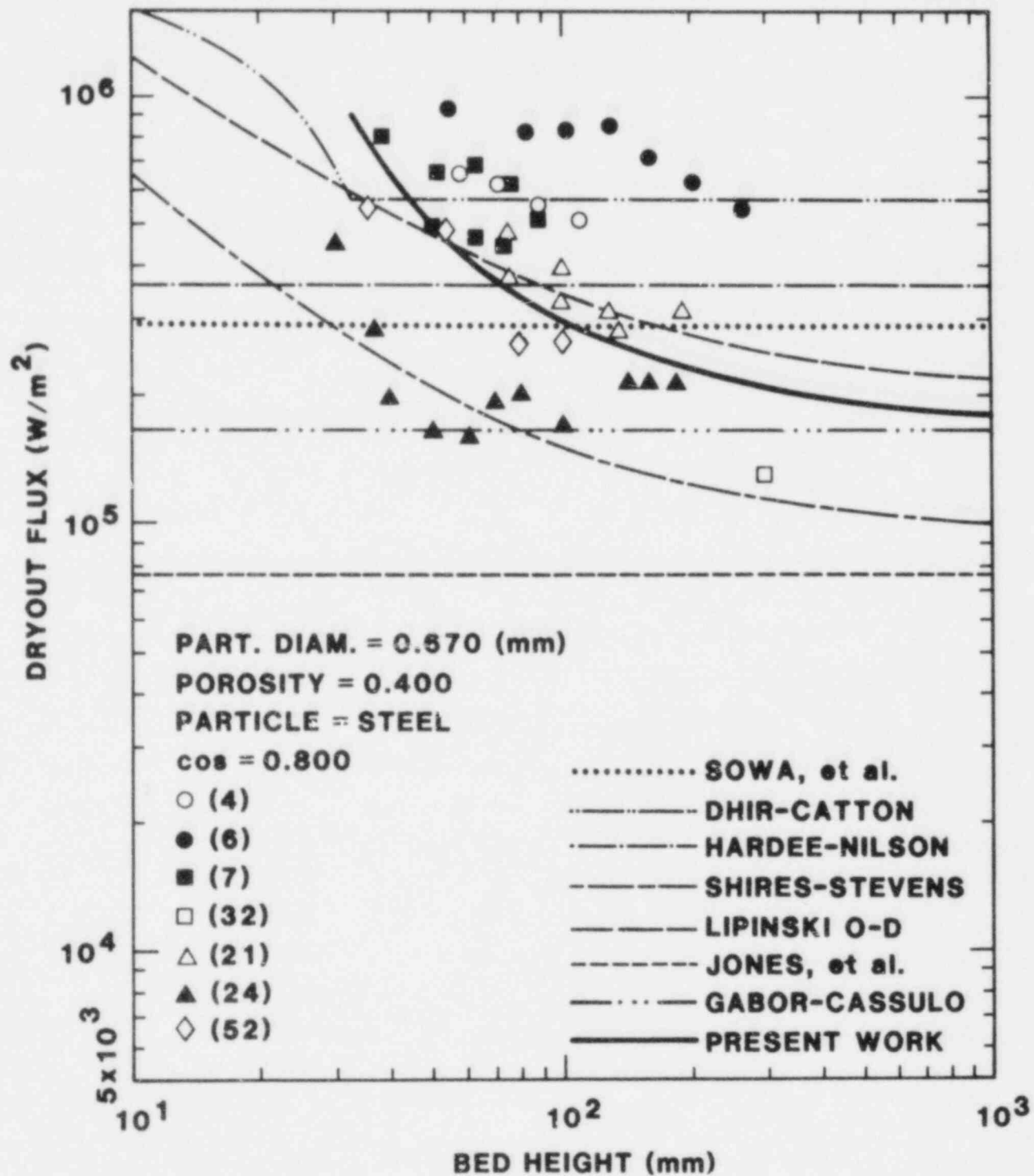


Figure 4-9(b). Dryout Flux vs. Bed Thickness for Various Models With a Water-Steel Bed With 40% Porosity and 0.68-mm Particle Diameter. The data of several references are shown in Figure 4-9b.

ACETONE

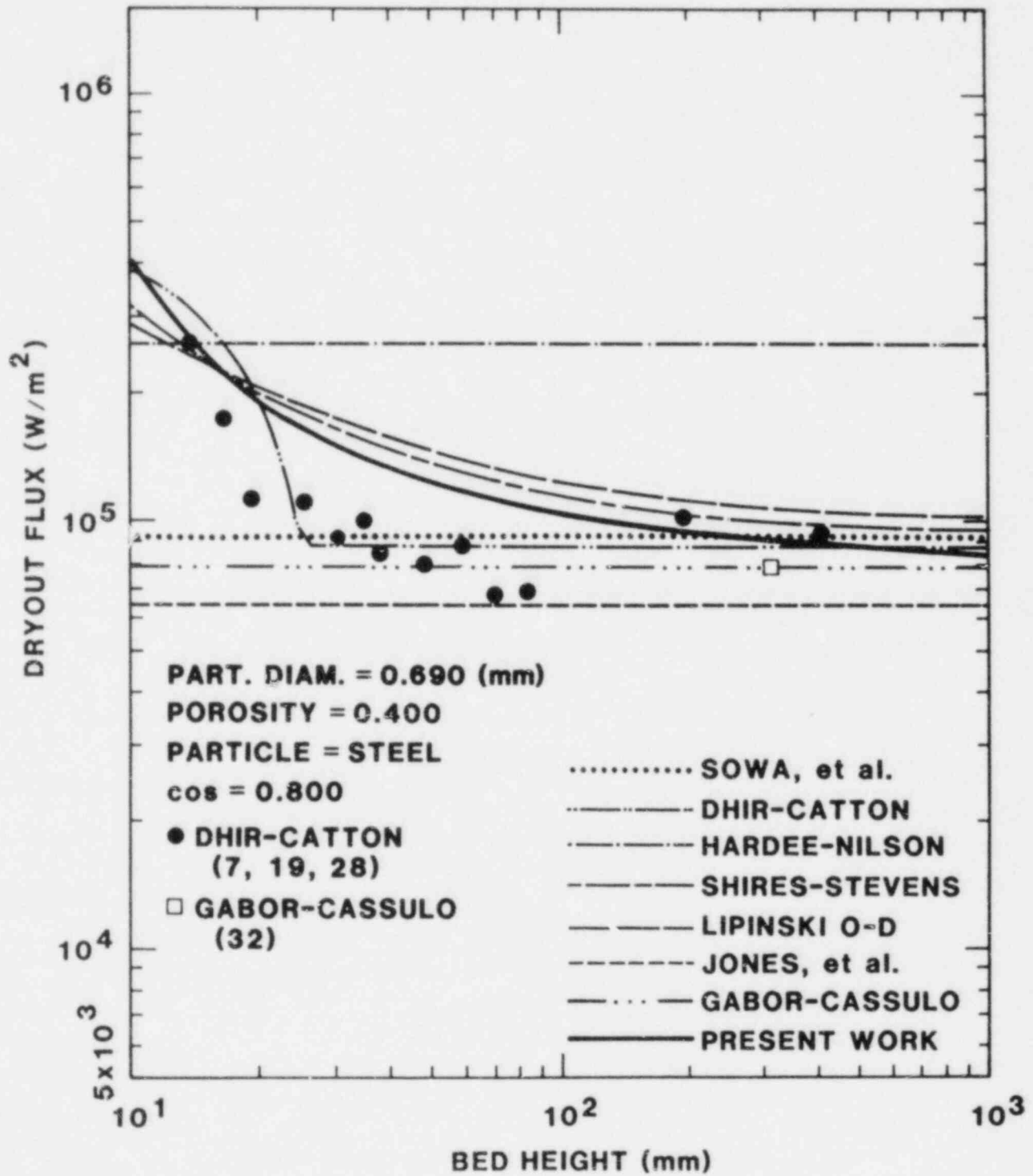


Figure 4-10. Dryout Flux vs. Bed Thickness for Acetone-Steel Beds Compared With Data.

fit primarily to this data with three empirical constants) agree with the data quite well. The models with capillary force predict a somewhat smoother bed height dependence than the data suggests, but nonetheless predict the generally small height dependence seen over most of the range. Indeed, nearly all the models perform well with deep acetone-filled beds. Without Figure 4-9b, this might give one a false sense of security.

The models are compared with the non-subcooled sodium-UO₂ data of Gabor, et al. [3] in Figure 4-11. The average particle diameter is taken as 0.325 mm, as suggested by the Fair-Hatch formula [55] (see Section 5.6). The porosity decreased substantially with bed height so the porosities used in the curves were their recommended values:

$$\epsilon = 0.593 - \left(\frac{0.507L}{1 - 1.25L} \right) \quad (4-4)$$

where L is the bed height in meters. To avoid extremes in the figure, a lower limit to the porosity was set at 0.40. (This limit is outside the range of the data.) The large variation in porosity gives bed height dependence to models which do not have it with constant porosity. However, only the present model has sufficiently strong dependence to match the data. The deviation of the zero-D model (which includes packed-bed capillary force) from the data indicates that channeling is an important part of the modeling for this data.

One important aspect of knowing the proper dependence of heat flux on bed thickness and material properties lies in properly interpreting experiments with simulant coolants. Reference 28 shows that there is no difference in dryout flux in acetone between a bed 30-mm and one 400-mm thick (with a particle diameter of 0.7 mm). Thus one might conclude the same about water. But the capillary force is much stronger in water than in acetone, and bed thickness effects depend on capillary force. For example, the present model predicts only a 76 percent difference in dryout flux with acetone (between 30 mm and 400 mm) but a 460 percent difference with water. Thus a 30 mm thick bed may be an improper simulation of a 400-mm thick bed with water.

SODIUM

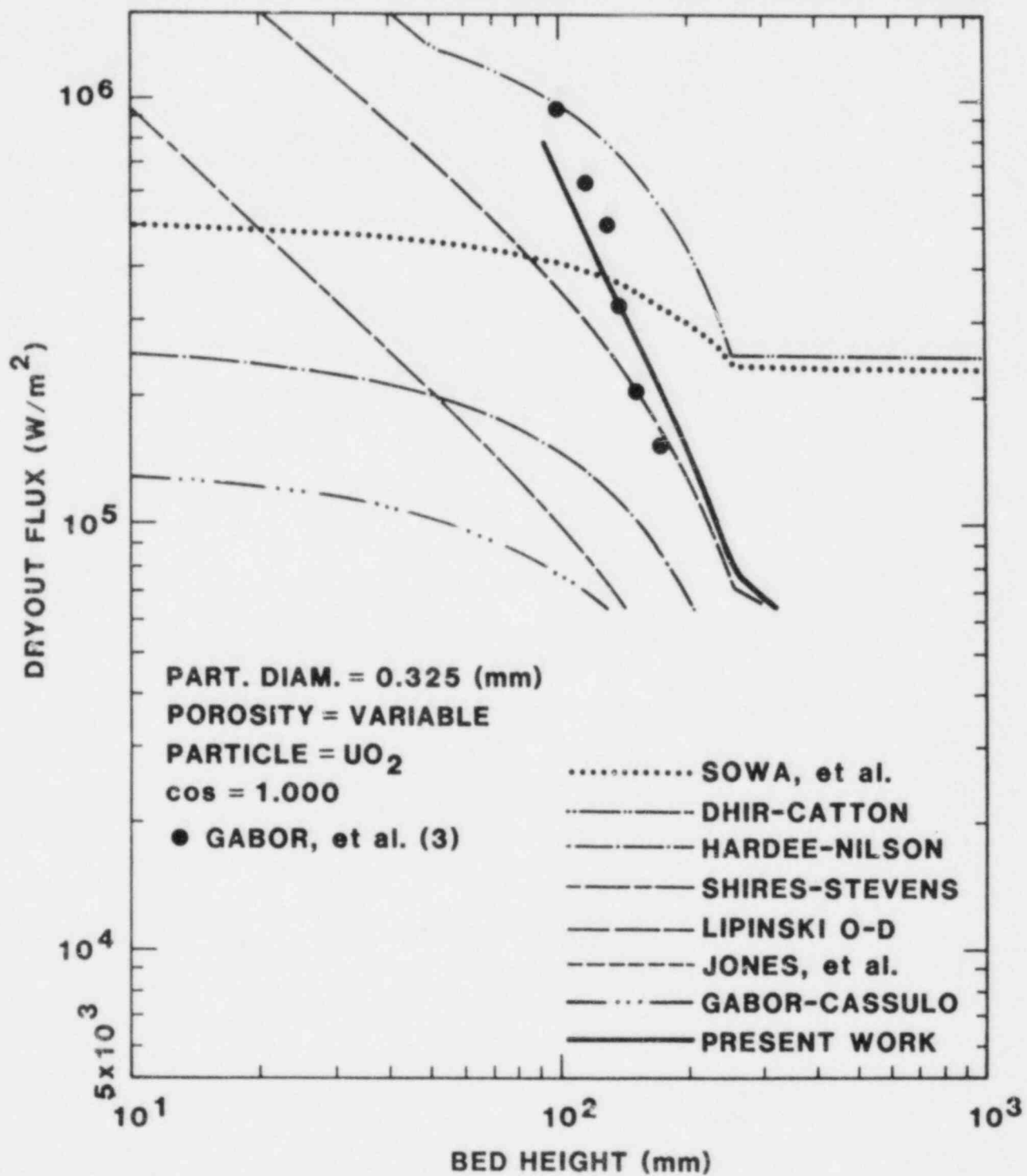


Figure 4-11. Dryout Flux vs. Bed Thickness for Sodium-UO₂ Beds Compared With the Data of Gabor, et al. [3].

4.3.3 Dryout Flux vs. Pressure

Figure 4-12 displays the present model's predicted pressure dependence of the dryout heat flux for water with various particle diameters and a 500-mm thick bed with 40 percent porosity. With small particles the dryout flux varies with pressure to the power of 0.64 near one atmosphere. This is because the vapor density is nearly linearly dependent on pressure near one atmosphere (denser vapor can carry more latent heat) but other material property changes impede heat removal. For large particles the pressure effect is less pronounced (pressure to the power of 0.40) because of the square-root dependence of the heat flux on the material properties. The rate of increase in dryout flux declines at higher pressures and reaches a maximum at about 60 bars.

Figure 4-13 shows the pressure dependence of the various models for water for the above case with 1-mm diameter particles. Most models show a strong pressure dependence near one atmosphere. The Dhir-Catton and Sowa, et al. models show the weakest dependence (pressure to the power of .31). There is no data with pressure variance for moderately deep or very deep beds. Reference 7 includes data for pressure variation by a factor of 4, but the beds were 20-mm to 60-mm thick and possibly subject to channeling. The observed heat flux in that case depended on about the fourth root of pressure. The proper dependence should be resolved because pressures of 170 atmospheres exist in water reactors and pressures of about two atmospheres (partly hydrostatic) exist at the bottom of sodium reactors.

4.3.4 Dryout Flux vs. Bed Porosity

Figure 4-14 displays the predicted porosity dependence of the dryout flux for a 500-mm thick water-UO₂ bed with various particle diameters. The changing slope indicates that near 50 percent porosity, the heat flux varies approximately with porosity to the fifth power for very deep small-particled beds, and second power for beds with large particles (the vertical scale is four times the horizontal scale.) In many cases, the sensitivity to porosity is not as large as some early models predicted (fifth power).

WATER

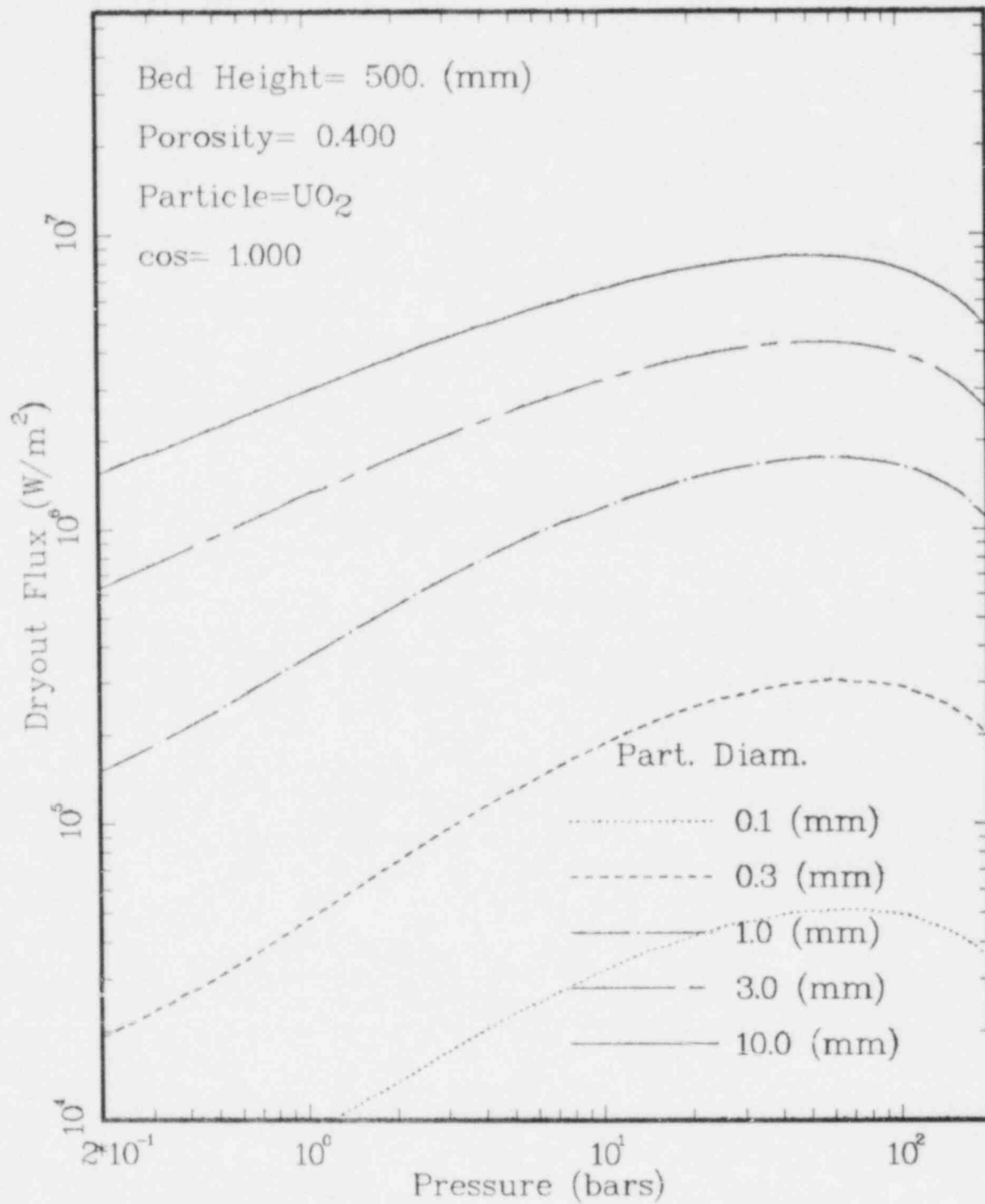


Figure 4-12. Dryout Flux vs. Pressure for a 500-mm Thick Water-UO₂ Bed With 40% Porosity and Various Particle Diameters.

WATER

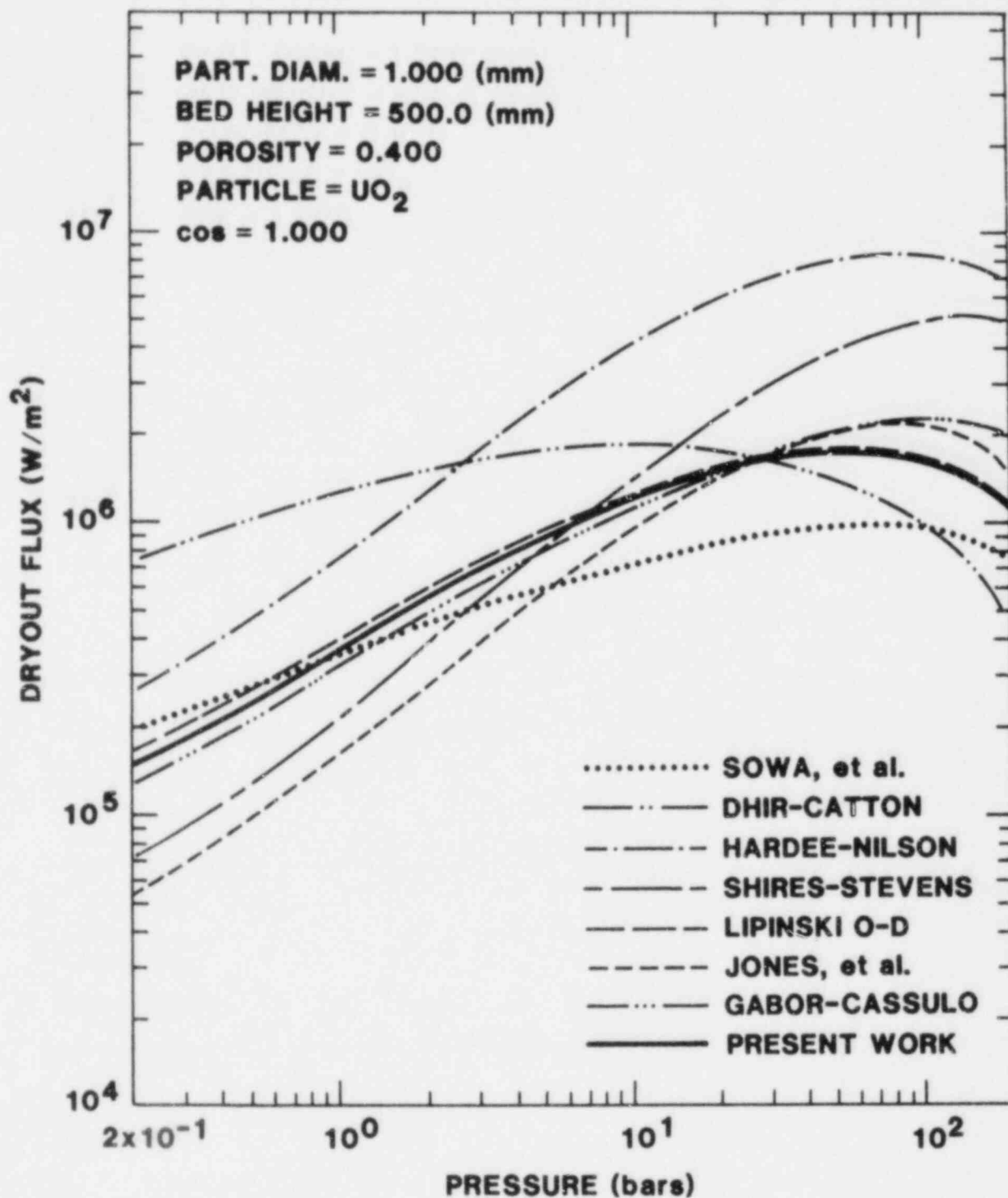


Figure 4-13. Dryout Flux vs. Pressure for Various Models With a Water-UO₂ Bed 500-mm Thick With 40% Porosity and 1-mm Diameter Particles.

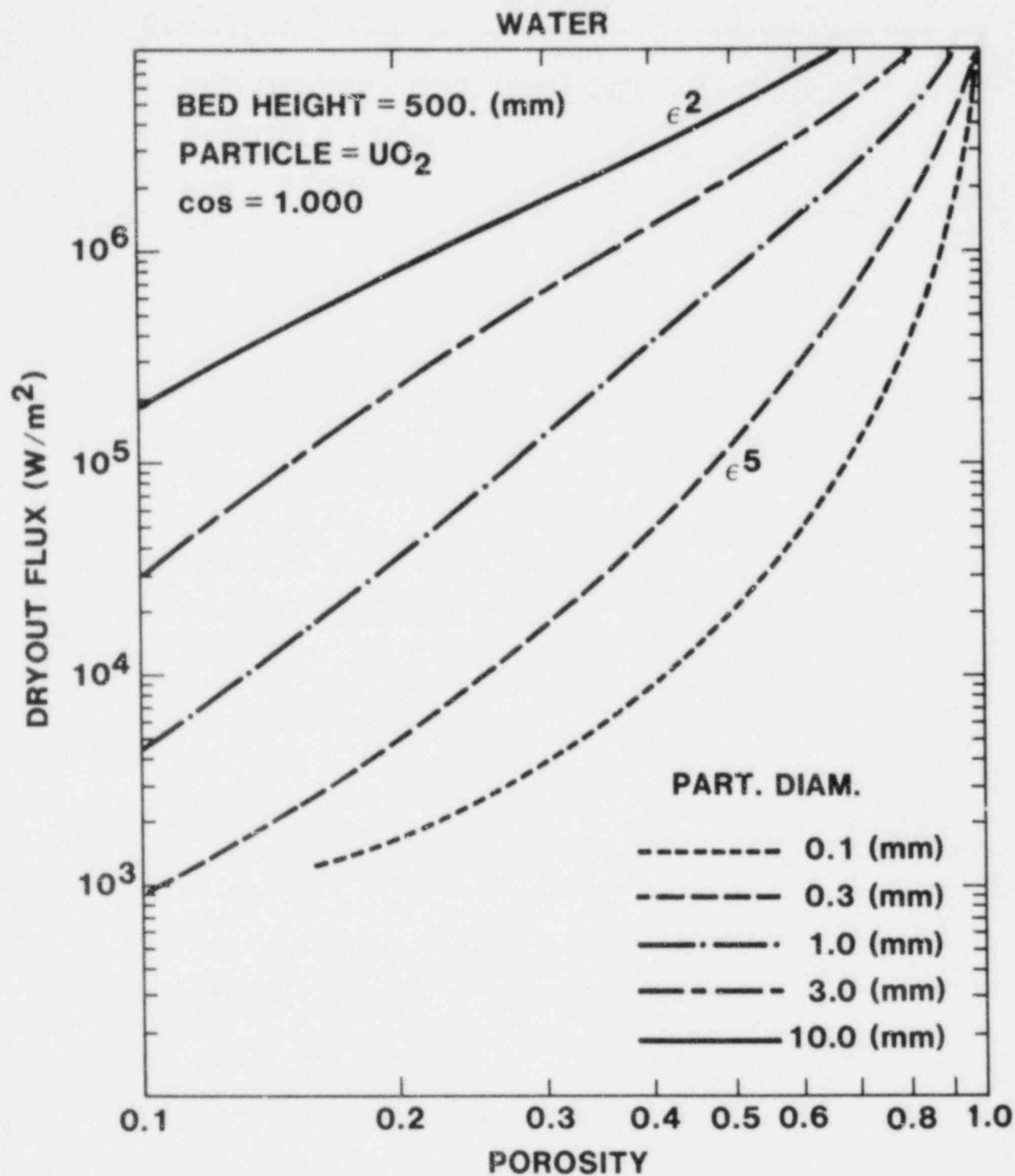


Figure 4-14. Dryout Flux vs. Porosity for a Water-UO₂ Bed 500-mm Thick With Various Particle Diameters.

4.3.5 Comparison With Dryout Measurements

The previous data comparisons have shown selected dependencies while holding other parameters fairly constant. Because of the many variables involved, perhaps the best way to compare a wide range of data is to plot the measured dryout flux vs. the predicted dryout flux. Then a perfect model would place all the data on a 45% line.

There have been many measurements of dryout flux with volume heating using various fluids and particles (see Section 2.1). The dryout data presently available are summarized in Appendix A. All measurements from a single reference in which particle diameter, bed thickness, and material properties are within 15 percent of each other, and in which porosity is within 5%, have been averaged to one point. This data set (260 points) includes six different fluids, (water, acetone, freon-113, methanol, isopropanol, and sodium), five different solids (steel, bronze, copper, lead, urania), spans bed thicknesses from channeled (15 mm) to very deep (450 mm), includes particle diameters from 0.26 mm to 16 mm (i.e., from laminar to turbulent flow), and porosities from 0.37 to 0.54. The measured dryout fluxes span two and one-half orders of magnitude (16 kW/m² to 4300 kW/m²). All pressures are at one atmosphere unless otherwise indicated.

A comparison between all the one-atmosphere data from Appendix A (260 points) and the present model is shown in Figure 4-15a. The plot is log-log so that underpredictions and overpredictions by the same factor will receive the same visual weight. The model agrees quite well with the data. Comparisons with other models are shown in Figures 4-15b through 4-15h. Only the models by Sowa, et al. [1] and the early zero-D model by Lipinski [27] yield comparable agreement with the data.

An average error fraction may be defined as

$$f = \sum_i f_i / N \quad (4-5)$$

PRESENT WORK

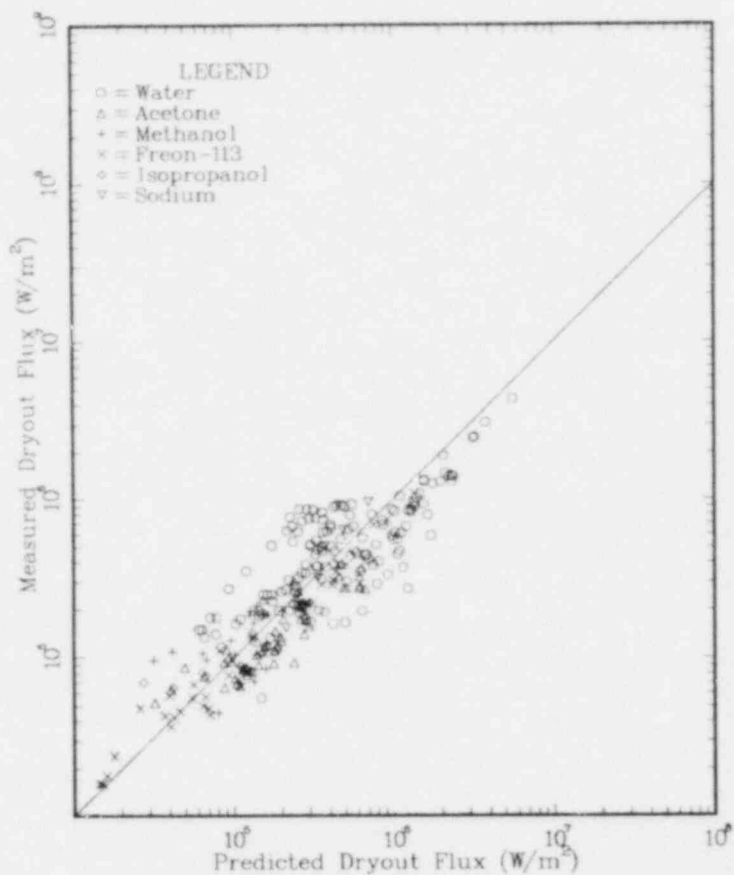


Figure 4-15a. Comparison of Volume-Heated Bed Dryout Data for Single-Sized Spheres With Dryout Models of the Present Work.

SOWA, ET AL. MODEL

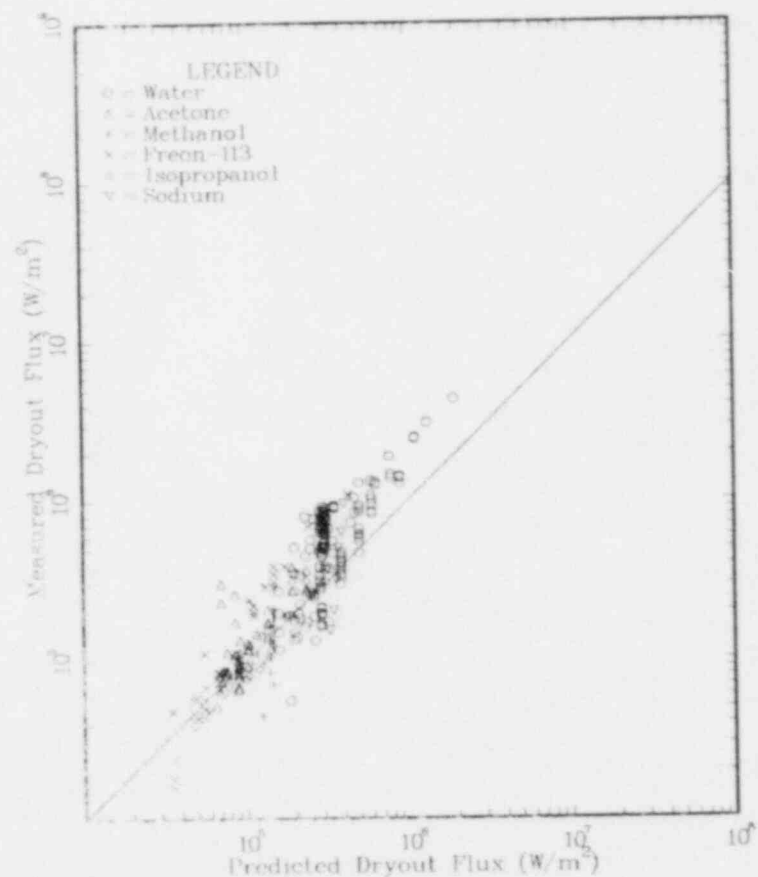
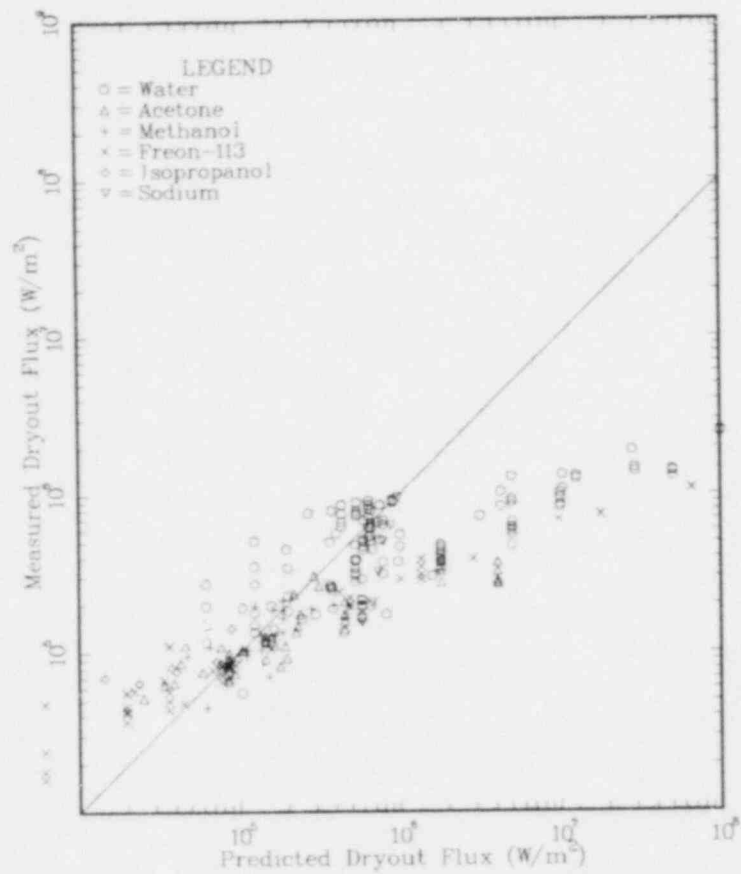


Figure 4-15b. Comparison of Volume-Heated Bed Dryout Data for Single-Sized Spheres With Dryout Models of Sowa, et al. [1].

DHIR-CATTON MODEL



HARDEE-NILSON MODEL

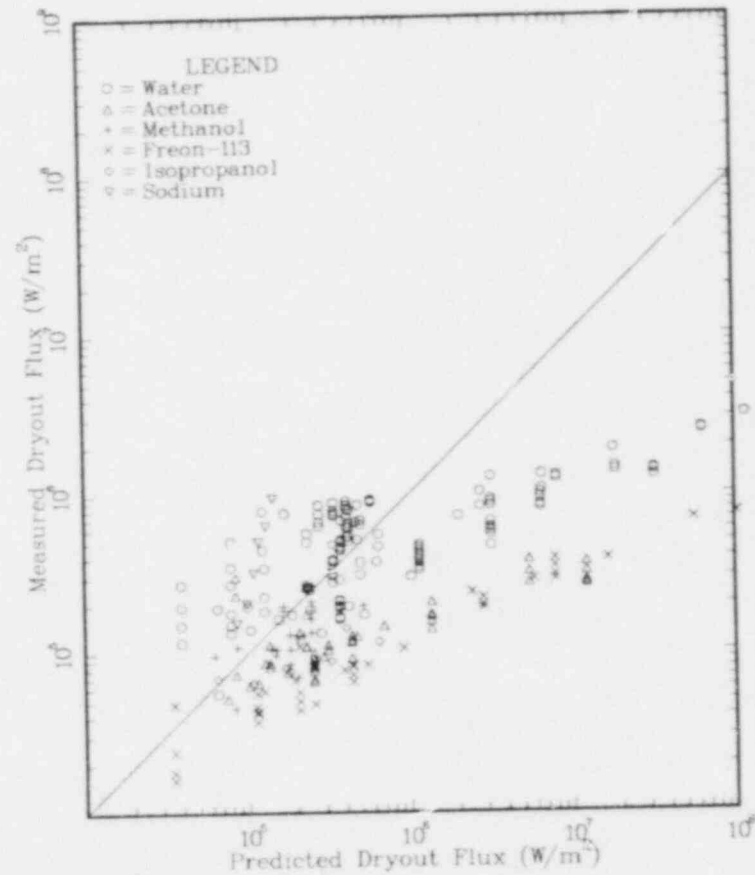


Figure 4-15c. Comparison of Volume-Heated Bed Dryout Data for Single-Sized Spheres With Dryout Models of Dhir and Catton [5,7] (Combined Deep and Shallow")

Figure 4-15d. Comparison of Volume-Heated Bed Dryout Data for Single-Sized Spheres With Dryout Models of Hardee and Nilson [8]

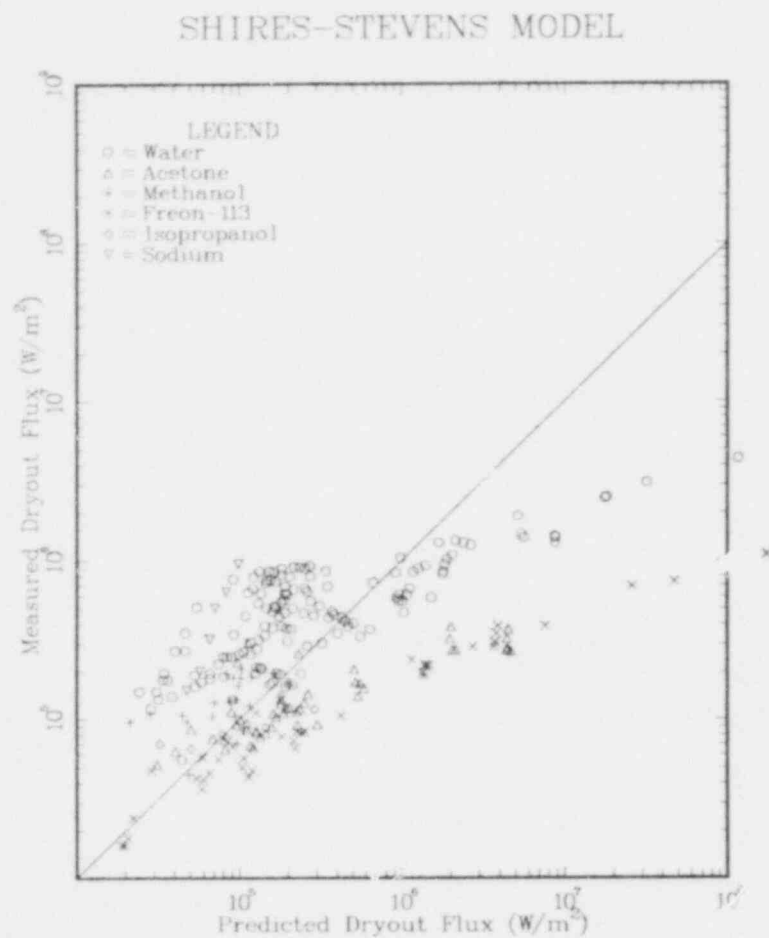


Figure 4-15e. Comparison of Volume-Heated Bed Dryout Data for Single-Sized Spheres With Dryout Models of Shires and Stevens [20]

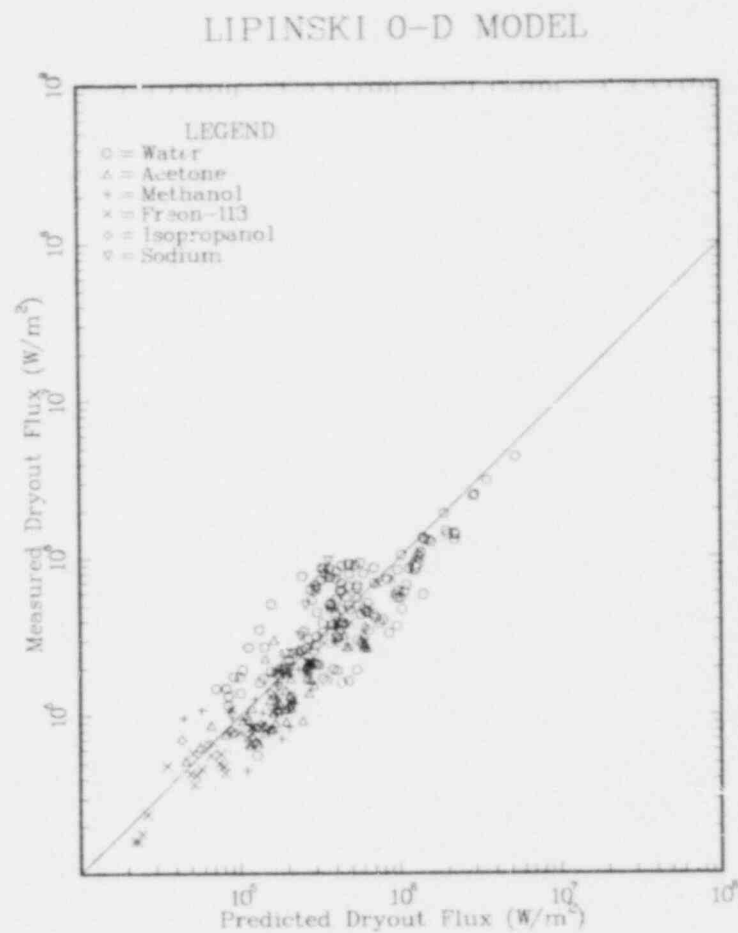


Figure 4-15f. Comparison of Volume-Heated Bed Dryout Data for Single-Sized Spheres With Dryout Models of Lipinski [27] (Early Zero-D)

JONES-EPSTEIN MODEL

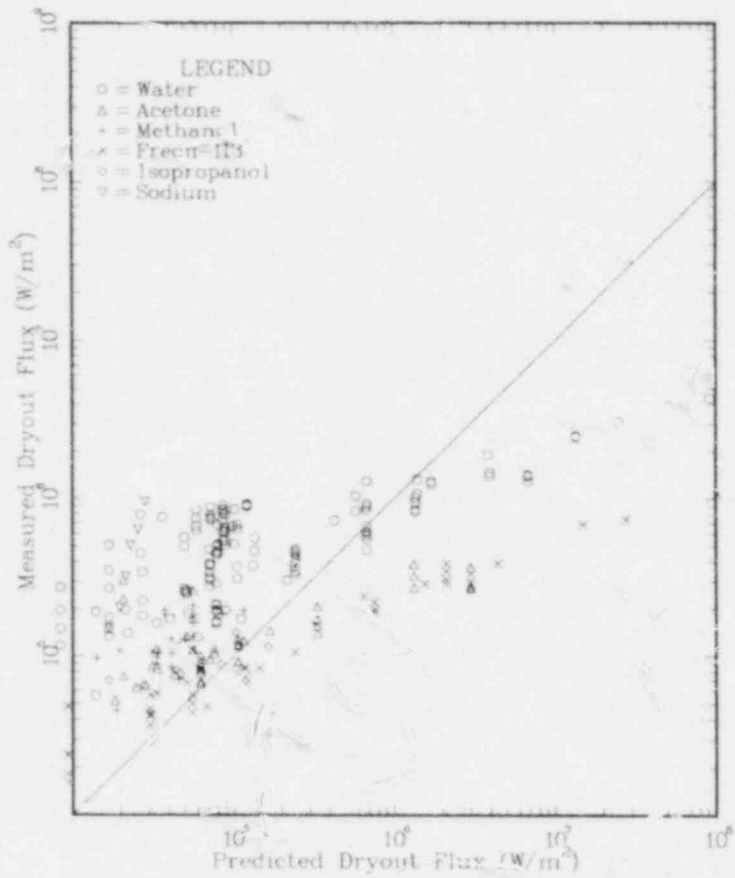


Figure 4-15g. Comparison of Volume-Heated Bed Dryout Data for Single-Sized Spheres With Dryout Models of Jones et al. [29]

GABOR MODEL

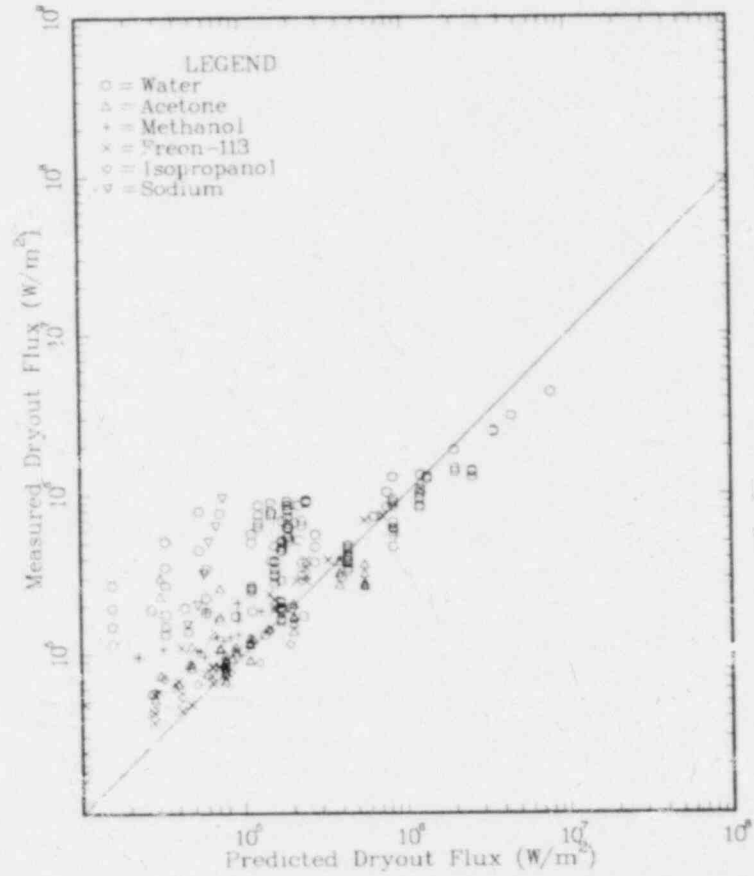


Figure 4-15h. Comparison of Volume-Heated Bed Dryout Data for Single-Sized Spheres With Dryout Models of Gabor et al. [32]

where N is the number of data points and

$$f_i = \frac{q_m}{q_p} - 1 \quad \text{for } q_m > q_p \quad (4-6)$$

$$= \frac{q_p}{q_m} - 1 \quad \text{for } q_p > q_m \quad (4-7)$$

where q_m and q_p are the measured and predicted dryout fluxes. The definition is designed so that f_i is always positive and so that overpredictions and underpredictions by the same factor yield the same error fraction. The average error fraction for the various models applied to the data from Appendix A is shown in Table 4-1.

Table 4-1. Average Error Fraction for Published Dryout Models

<u>Model</u>	<u>Error Fraction</u>
Sowa, et al. [1]	0.61
Dhir-Catton [5,7]	3.94
Hardee-Nilson [8]	6.94
Shires-Stevens [20]	3.41
Lipinski (early zero-D) [27]	0.54
Jones, et al. [29]	4.80
Gabor, et al. [32]	1.59
Present Work	0.60

The scatter in dryout data for supposedly nearly identical beds shown in Figure 4-9b suggests that it may be impossible to achieve a lower error fraction than the present model (or reference 27 model) obtained with the complete data set. This may be due to unreported bed differences or calibration discrepancies. Using the data from a single research team with one set of equipment and techniques may help reduce some of the scatter. The data of Barleon and Werle [23,33,52] include water and freon-113,

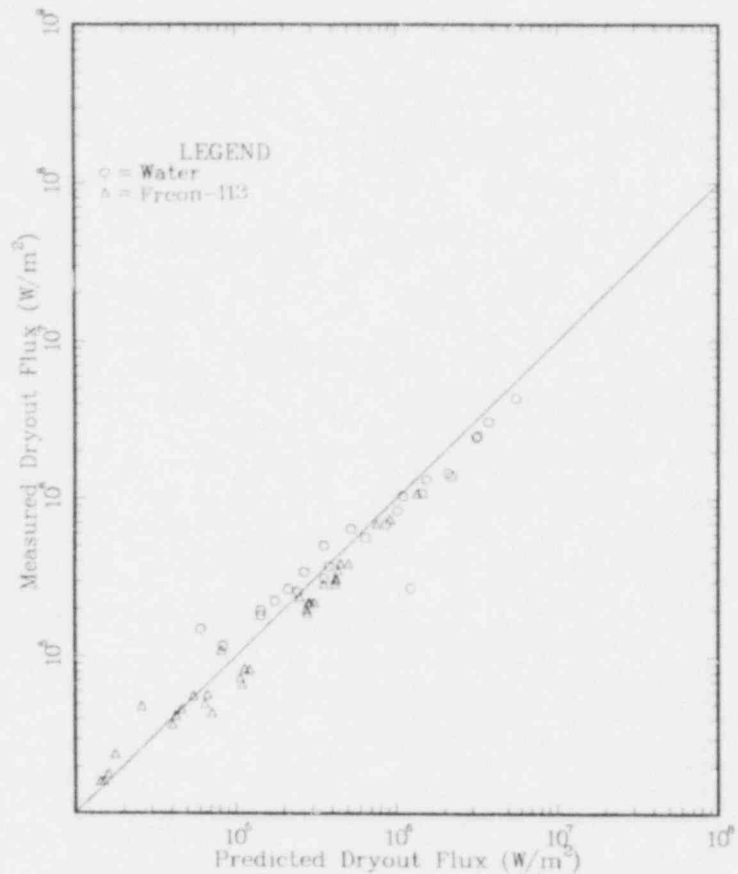
span bed thicknesses from 30 mm to 100 mm, particle diameters from 0.26 mm to 16 mm, and heat fluxes from 16 kW/m² to 4300 kW/m². (Indeed their data is responsible for much of the expanse of the full data set in Appendix A.) Thus that data set represents a wide span with a consistent calibration and measurement technique. In addition, they explicitly account for radial heat losses. Finally, with only two fluids, comparisons between fluids will be less confusing.

A comparison of the Barleon-Werle data with the present model is shown in Figure 4-16a. The average error fraction with this data is 0.35 (vs. 0.60 with the full data set) and the agreement with the model is significantly better than with the full data set. Part of this difference in agreement may be due to modeling errors involving the additional fluids in the full set. But it is also quite likely that much of it is due to calibration and measurement differences (particularly with radial heat losses).

The plot for the Sowa et al. model [1] is shown in Figure 4-16b. The correlation in the large-particle region is good but consistently high by a factor of two. This may be because the model is based on a flooding correlation, which is more appropriate for a bottom-heated bed. The small-particle data is correlated fairly well also, even though the correlation was based on turbulent flow. The lack of dependence on bed thickness in the model causes data with a single particle diameter but different bed heights to be stacked in columns. (The average error fraction is 0.76.)

The Dhir-Catton model [5,7] is compared with the data from Barleon and Werle in Figure 4-16c. (The deep bed model or the shallow bed model is used, depending on the bed conditions.) The worst agreement is for large dryout fluxes, which correspond to large diameter particles and turbulent conditions. In that case, the prediction is as much as 50 times too large. This disagreement is because the model is based on laminar flow equations, and thus should really only be used for laminar (i.e., small-particle) conditions. However, even with small particles there is disagreement between predictions and the data. The predictions are generally too low. This is because of the lack of capillary force in the model, which can be important even when channels are not. In some cases the measurements for a particular

PRESENT WORK



SOWA, ET AL. MODEL

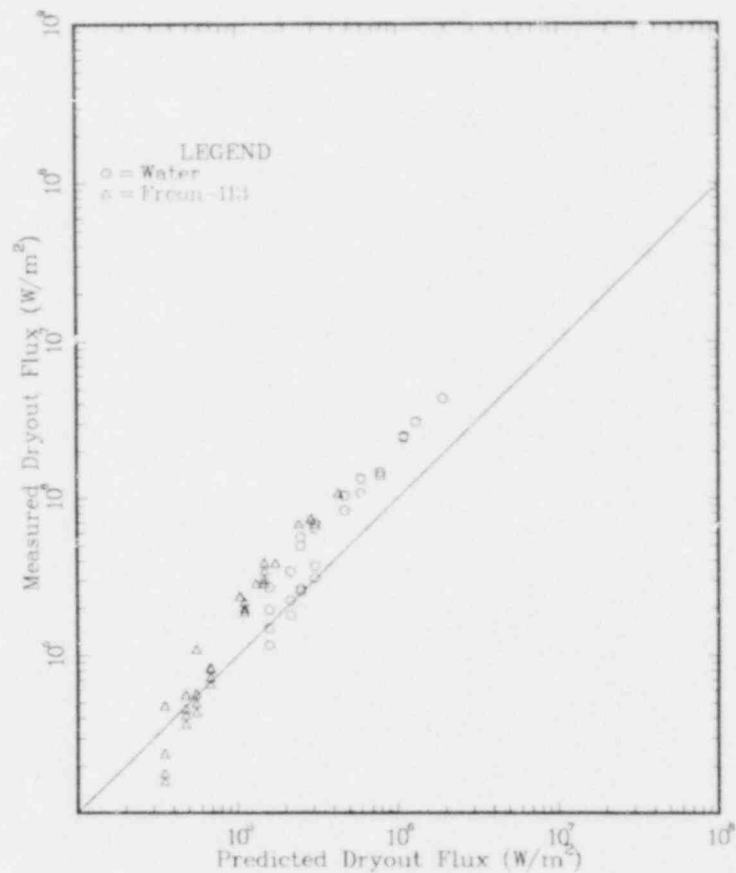
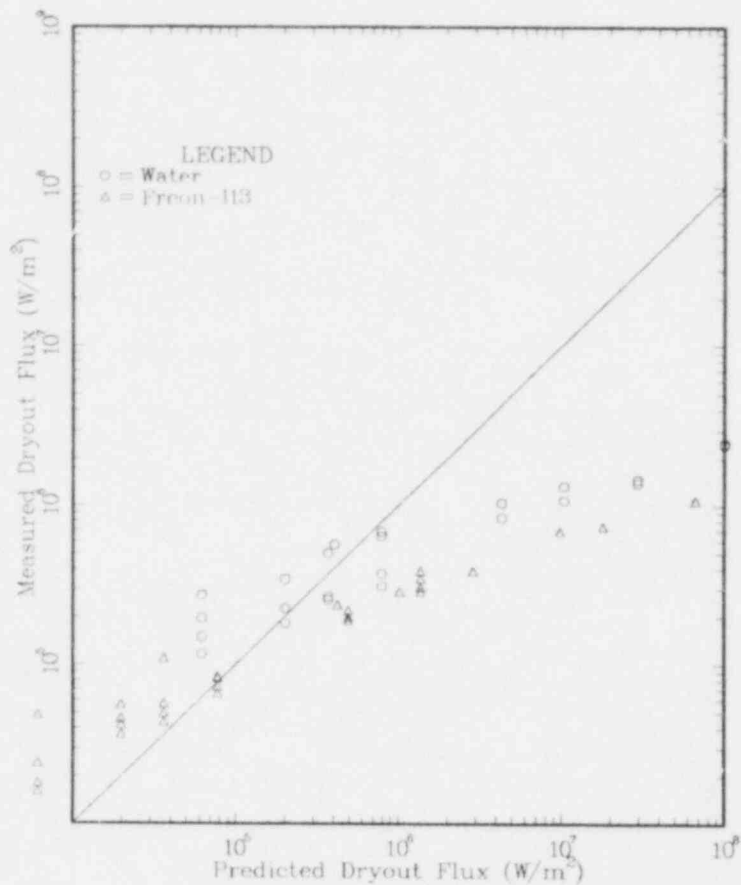


Figure 4-16a. Comparison of Barleon-Werle [33,52] Dryout Data With the Models in Figures 4-15a Through 4-15h.

Figure 4-16b. Comparison of Barleon-Werle [33,52] Dryout Data With the Models in Figures 4-15a Through 4-15h.

DHIR-CATTON MODEL



HARDEE-NILSON MODEL

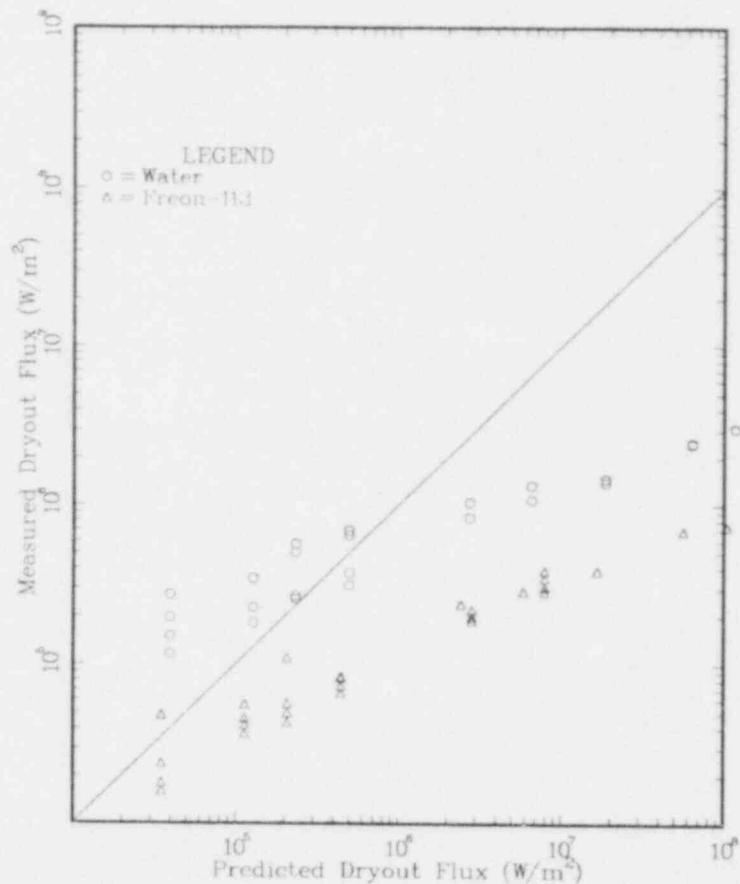


Figure 4-16c. Comparison of Barleon-Werle [33,52] Dryout Data With the Models in Figures 4-15a Through 4-15h.

Figure 4-16d. Comparison of Barleon-Werle [33,52] Dryout Data With the Models in Figures 4-15a Through 4-15h.

predicted flux are stacked in a column (e.g., at a predicted flux of 65000 W/m^2). This is not due to scatter in the measurement but rather is due to changes in bed thickness. Again, the lack of capillary force causes the disagreement.

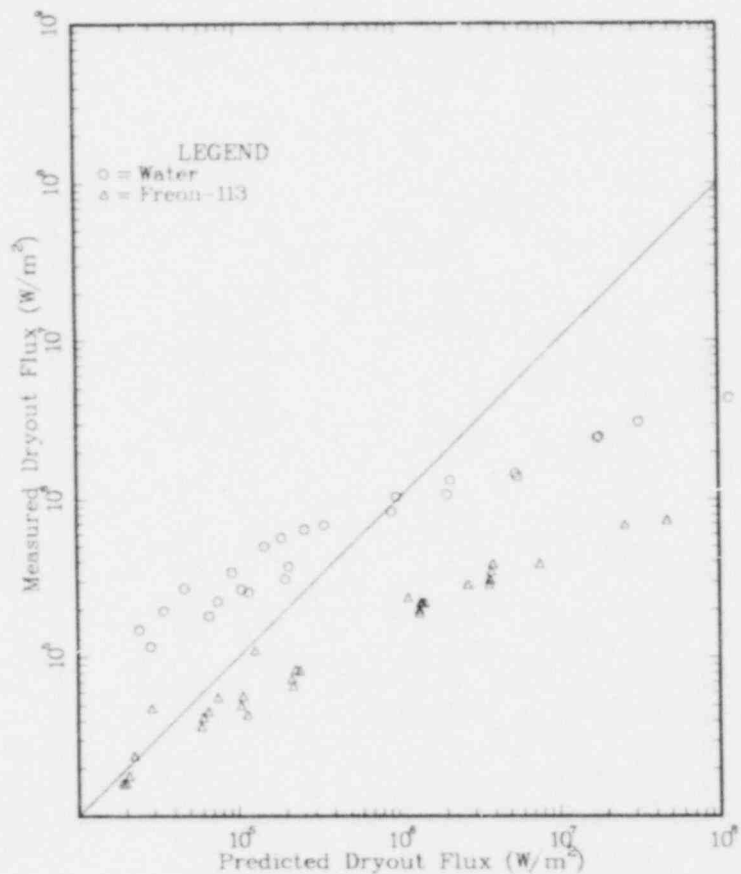
A similar plot for the Hardee-Nilson model [8] is shown in Figure 4-16d. The disagreement between model predictions and the data is even greater than with the Dhir-Catton model. Again, lack of turbulence and lack of capillary force are the main limitations. But in addition, there is a separation between the freon-113 and water data. This separation is partly due to a wrong dependence on viscosity in the model because of the linear relative permeabilities used in the Hardee-Nilson model. Use of cubic relative permeabilities in the present model resolves this difficulty.

A plot for the Shires-Stevens model [20] is shown in Figure 4-16e. The large-particle disagreement is again present. However, because the model includes capillary force, which gives it bed thickness dependence, data in which only the bed thickness is changed is no longer "stacked," as it was in the Dhir-Catton and Hardee-Nilson models. But, again, because of the linear relative permeabilities used, the water and freon-113 predictions are separated as in the Hardee-Nilson model.

The plot for the Lipinski early zero-D model [27] is shown in Figure 4-16f. The correlation is even slightly better than for the present model, although the amount is probably not significant. The main deficiency in the zero-D model is the lack of channeling. A major advantage is the greater simplicity. (An improved zero-D model will be developed in Section 6.1 and compared with the present (one-D) model in Section 6.2.)

The plot for the Jones et al. model [29] is shown in Figure 4-16g. The lack of turbulence and capillary force is again evident in the large and small particle data, respectively. The model is specified for bottom-heated beds, so a doubling of the predicted dryout flux would be justified. This would aid the small-particle correlation, but the scatter would still be large. In addition, the water and freon-113 data are separated by the model, indicating a difficulty in the relative permeability terms, even though the relative permeabilities were formulated to include liquid-vapor drag.

SHIRES-STEVENSON MODEL



LIPINSKI O-D MODEL

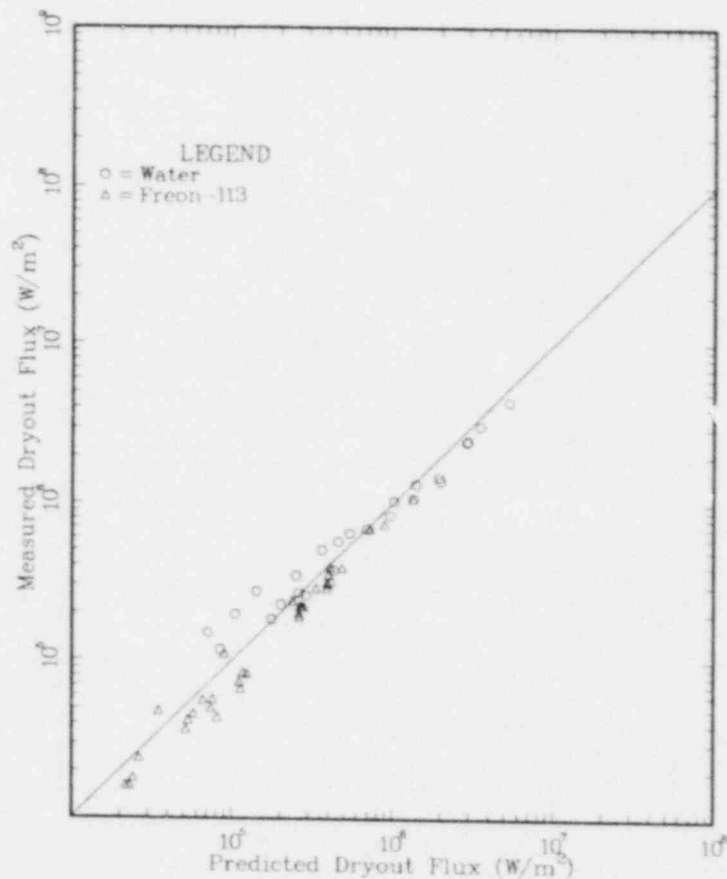
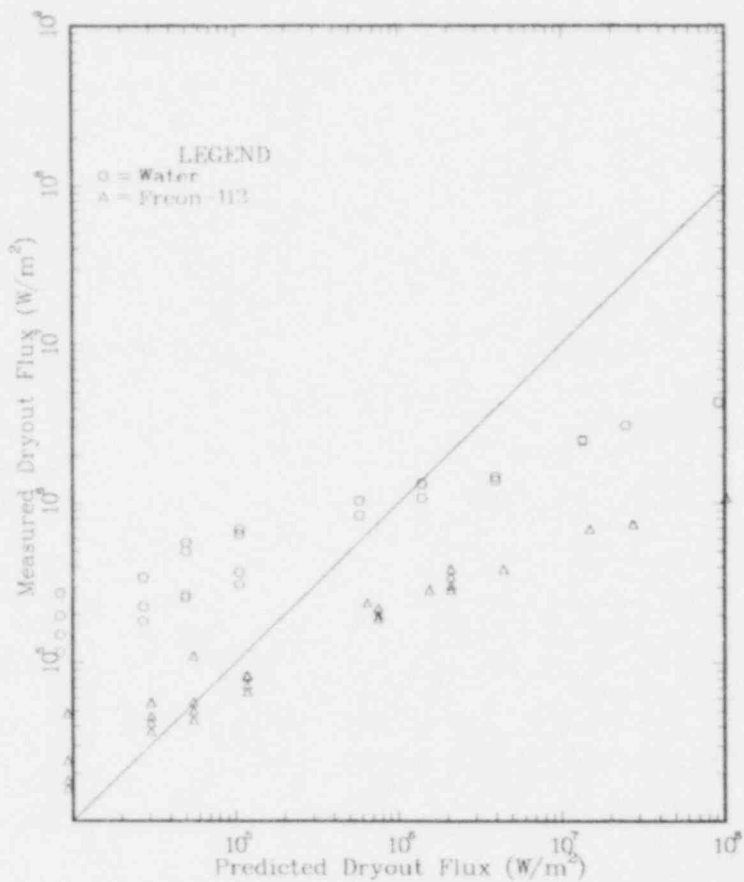


Figure 4-16e. Comparison of Barleon-Werle [33,52] Dryout Data With the Models in Figures 4-15a Through 4-15h.

Figure 4-16f. Comparison of Barleon-Werle [33,52] Dryout Data With the Models in Figures 4-15a Through 4-15h.

JONES-EPSTEIN MODEL



GABOR MODEL

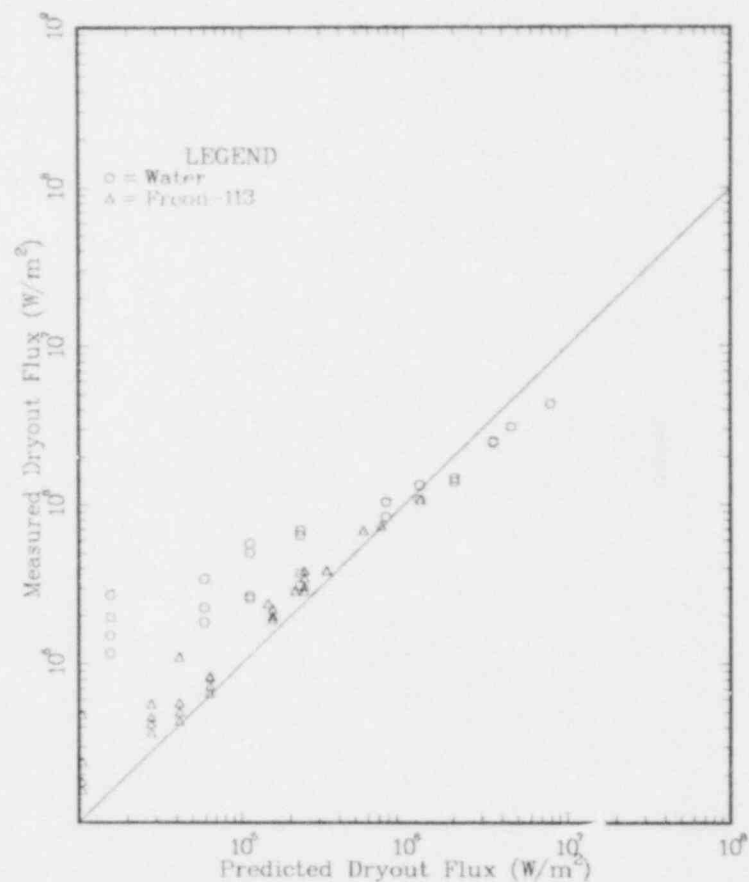


Figure 4-16g. Comparison of Barleon-Werle [33,52] Dryout Data With the Models in Figures 4-15a Through 4-15h.

Figure 4-16h. Comparison of Barleon-Werle [33,52] Dryout Data With the Models in Figures 4-15a Through 4-15h.

The plot for the volume-heated Gabor-Cassulo model [32] is shown in Figure 4-16h. The agreement in the large-particle region is good because of the use of the Ergun equation, but the lack of capillary force makes the agreement with small particles poor. The range of the data is not sufficient to test the unusual large-particle diameter dependence ($d^{5/6}$) in this model.

The average error fractions for the Barleon-Werle data set are summarized in Table 4-2.

Table 4-2. Average Error Fraction for Published Dryout Models Using Data From Barleon and Werle [23, 33, 52]

<u>Model</u>	<u>Error Fraction</u>
Sowa, et al. [1]	0.76
Dhir-Catton [5,7]	9.00
Hardee-Nilson [8]	19.08
Shires-Stevens [20]	8.22
Lipinski (early zero-D) [27]	0.30
Jones, et al. [29]	7.13
Gabor, et al. [32]	1.54
Present Work	0.35

4.4 Dry Zone Thickness

Having considered the conditions necessary to obtain incipient dryout, let us now consider what happens with powers above the incipient dryout power. As noted in Section 4.3, the present model predicts the existence of stable a dry zone for heat fluxes above the dryout flux. The steady-state dry zone thickness is predicted to increase as the bed power increases. (See Figures 4-3a and 4-3b.) The heat produced in the dry zone is assumed to be transmitted by some means (most likely by conduction and radiation) to the base of the boiling zone. (This is required by Equation 3-19.) If the dry zone is too thick, melting and restructuring of the debris may occur. The present model does not address that issue.

Stable dry zones have been consistently observed in subcooled sodium-UO₂ tests [9,12,30,51] and presumably exist in non-subcooled beds also. Figure 4-17a and b display the dry zone thickness vs. power for sodium-UO₂

beds 150-mm thick with 40 percent porosity and particle diameters of 0.3 mm and 3.0 mm, respectively. The dry zone in Figure 4-17b is hypothetical since it would melt before achieving steady state. The dry zone is much thicker for a given power above dryout for the large-particle case than for the small-particle case. The reason is that the influence of capillary force, which allows steady dry zones to exist, is less with large particles. With large particles, the dry zone attempts to extend to the layer where capillary force is influential. This is at the minimum in the saturation curve in Figure 4-3b. Thus, the cool, thin, steady dry zones observed in the sodium-UO₂ tests [9,12,30,51] might be thick and rapidly melting in beds with large particles, or in thicker beds. (Unfortunately the D-series dry zones achieved to date have been too small, non-uniform, and near incipient dryout for a good comparison with the present model.)

Another aspect of dry zone formation is relevant to experiments. If the bed power is increased from just below dryout to just above dryout, the bed saturation state must change. In Figure 4-3a, the change is small and dryout will occur at the bed bottom. But in Figure 4-3b, the change is great and the dry zone is destined to be thick. Unfortunately such a thick dry zone under steady conditions would lead to particle melting. Thus, investigation of such a state is quite difficult. However, Equation (3-21) requires only that the heat flux at any level be expressed fully in vapor flow. Under steady-state dry conditions, the vapor is produced in a burst at the top of a dry zone by the heat flux delivered from the zone by conduction. But just prior to dryout (and after the power increase) vapor at that same elevation is the same as in steady-state dryout, except it is being delivered by transient boiling. Thus the vapor flow should be sufficient to prevent any further liquid penetration past that elevation. The boiling below that elevation must feed solely on the reservoir established before the power change. Referring to Figure 4-3b, that reservoir (or bed saturation) is smallest at the location of the top of the eventual dry zone. Thus one might expect the location of initial dryout to coincide with the eventual top of the dry zone. In other words, the dry zone would only grow downward with time (for a fixed power). If this is true, this would make study of the thick dry zone predictions much easier.

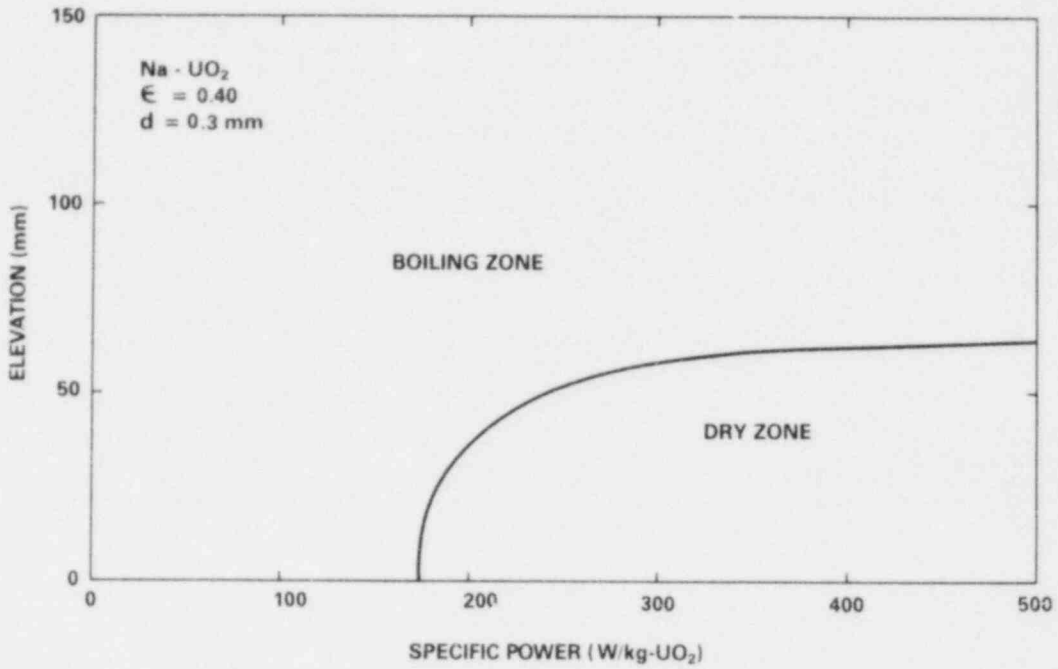


Figure 4-17a. Dry Zone Thickness vs. Power for Sodium-UO₂ Beds 150-mm Thick With 40% Porosity. Particle diameters are 0.33 mm.

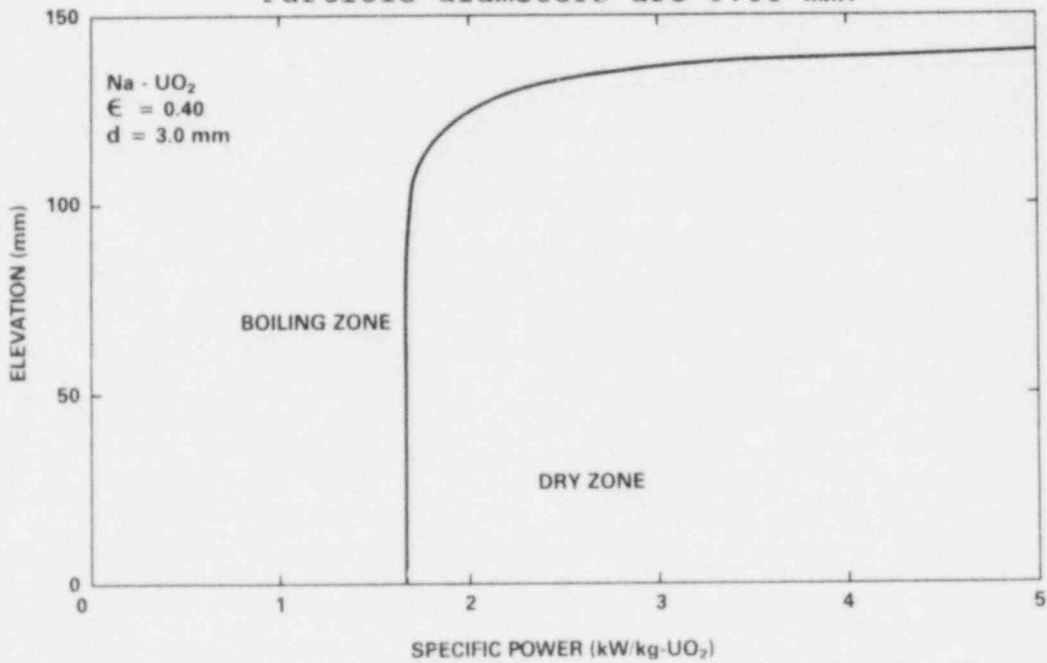


Figure 4-17b. Dry Zone Thickness vs. Power for Sodium-UO₂ Beds 150-mm Thick With 40% Porosity. Particle diameters are 3.0 mm.

Trenberth and Stevens [24] may have seen some aspect of this effect. They report that the location of initial dryout tends to increase with increasing particle diameter or bed height. This agrees with the trends in the saturation curves in Figures 4-3a and 4-3b. However, there is much scatter in the data.

4.5 Summary of Model Features for a Uniform Bed on a Plate

The present model predicts channel length, subcooled zone thickness at incipient channel penetration, saturation (liquid fraction) within the bed as a function of elevation, incipient dryout power, and dry zone thickness as a function of power. It can be applied to either uniform beds or stratified beds, with either an adiabatic support or a bottom-cooled support which is either permeable or subcooled.

A uniform bed on an adiabatic impermeable support is the simplest situation. For this case, the model predicts channel lengths which are similar to that predicted by Jones and Baker [31], but which increase slightly with power. For channels to penetrate a subcooled zone, the model requires that the zone be slightly thinner than the resulting channel length. Within the bed, the model predicts that the saturation should increase monotonically with elevation if the particles are small and the bed not too thick. But for thicker beds with larger particles, the model predicts a minimum in the saturation at a distance below the base of the channeled region less than the capillary head (see Equation 4-1).

The heat flux at dryout in a uniform bed is predicted to increase with increasing particle diameter, with decreasing bed thickness, and with increasing porosity. The dependency on all these parameter changes depending on whether the bed is channeled, moderately deep, or very deep. The dryout fluxes observed in the literature range from channeled to very deep, from laminar to turbulent, and span two and one-half orders of magnitude in dryout flux. The 260 data points are correlated by the model with an average error of 60 percent.

For powers above incipient dryout, the model predict a stable dry zone at the base of the bed which increases with increasing power. The dry zone is generally thicker with deeper beds or larger particles. Dry zone measurements need to be made yet for comparison with the model.

5. MODEL PREDICTIONS FOR OTHER BED TYPES

The previous chapter described the features of the one-D model as applied to the simple case of a uniform bed on an adiabatic impermeable support. This chapter shall describe the application to beds with other conditions.

5.1 Very Deep Beds

For some applications, a particle bed may be very deep. (This is especially true for water reactors.) With a very deep bed, capillary force is negligible and the first two terms of Equation (3-20) may be dropped. In addition, channels may be ignored. Equation (3-20) then becomes algebraic and much easier to solve:

$$\begin{aligned}
 & \frac{1.75 (1-\epsilon)q^2}{\epsilon^3 dh_{1v}^2} \left(\frac{1}{\rho_v(1-s)^3} + \frac{1}{\rho_1 s^3} \right) \\
 & + \frac{150 (1-\epsilon)^2 q}{\epsilon^3 dh_{1v}} \left(\frac{\mu_v}{\rho_v(1-s)^3} + \frac{\mu_1}{\rho_1 s^3} \right) \\
 & + \frac{(1-\epsilon)w}{3 \epsilon d \rho_1 s} \left(\pm 1.75w + \frac{3.5q}{h_{1v}} - \frac{150(1-\epsilon)\mu_1}{d} \right) \\
 & = (\rho_1 - \rho_v)g \quad \text{for } q \gtrsim wh_{1v} \quad (5-1)
 \end{aligned}$$

The equation is still one-dimensional since the particle diameter and bed porosity may be functions of elevation and q need not reflect a uniform source.

For simplicity in describing the features of this equation, the bed now will be assumed to rest on an adiabatic impermeable plate so that $w = 0$ and $z = 0$ at the bed bottom.

In addition, the source will be assumed uniform so that conversion between q and z is simple [i.e., Equation (3-19) applies]. (Other conditions would yield many of the same qualitative results.) Equation (5-1) then becomes

$$\frac{1.75 (1-\epsilon) S^2 z^2}{\epsilon^3 d h_{lv}^2} \left(\frac{1}{\rho_v (1-s)^3} + \frac{1}{\rho_l s^3} \right) + \frac{150(1-\epsilon)^2 S z}{\epsilon^3 d h_{lv}} \left(\frac{\mu_v}{\rho_v (1-s)^3} + \frac{\mu_l}{\rho_l s^3} \right) = (\rho_l - \rho_v) g \quad (5-2)$$

The elevation z may be easily solved for as a function of saturation.

Figure 5-1 shows the saturation in a very deep water-filled bed 1.0 m thick with 40 percent porosity and 1 mm particle diameter. Curves for various powers are shown. Since Equation (5-2) is quadratic, there are two possible saturations at each elevation. Only the solution with large saturation is stable against perturbations in power or saturation. For example, if the bed were in the state of lower saturation and a small decrease in power occurred, it would then be in a state which could remove more heat than was being produced. This would allow more liquid to enter than would be removed by vaporization, the saturation would increase more, and eventually the bed state would change to the one with a large saturation. Conversely, a small increase or decrease in power with the bed in the state with large saturation would cause a respective decrease or increase in heat removal capability, driving the bed back to the large saturation state. Thus the state with large saturation would be stable and the one with small saturation would be unstable.

As the power in the bed increases, the saturation in the stable solution decreases. Physically, the excess vapor produced by the power increase expels some liquid until there is sufficient room for it to exit. The denser liquid on the other hand, does not need as much room as the vapor, and thus, is still able to maintain a replenishing flow. Subsequent power increases yield more vapor, which reduces the saturation and allows more heat removal.

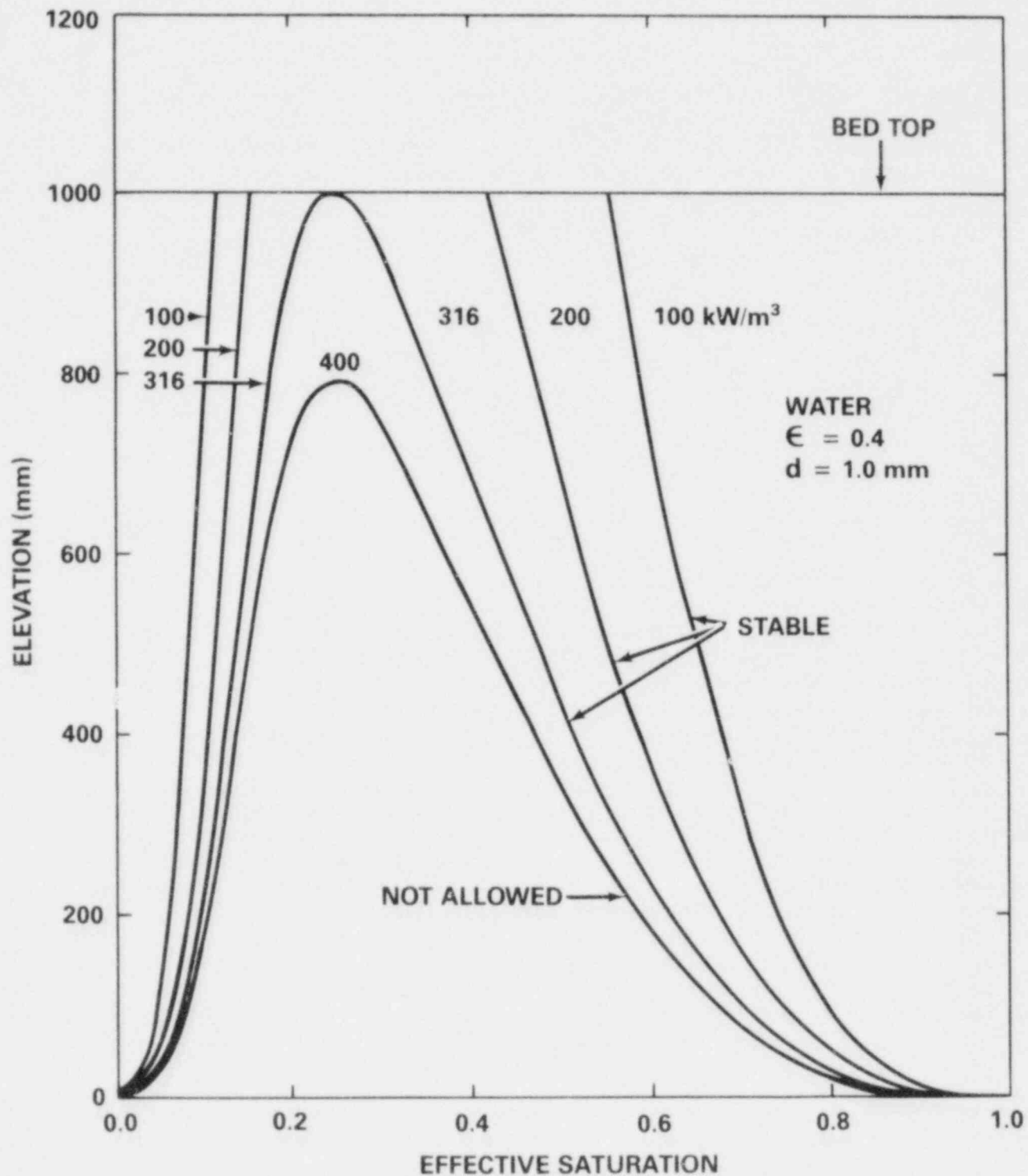


Figure 5-1. Saturation Profile in a Very Deep Water-Filled Bed 1 Meter Thick With 40% Porosity and 1-mm Diameter Particles. Several powers are considered.

However, at some power, a further power increase will generate enough vapor to restrict the liquid flow so that it is not adequate to maintain the vaporization. When this happens, dryout occurs. This condition occurs at a power of 316 MW/m^3 for the bed in Figure 5-1. For higher powers (e.g., 400 MW/m^3) the saturation is not defined in the top portion of the bed since there is no real solution to Equation (5-2) there. Thus the entire bed is predicted to dry out for any power above the incipient dryout power. This trend was noted in Section 4.4 as the particles became large or the beds became deep.

The dryout power may be determined by finding the curve for the largest power which still yields a real solution to Equation (5-2) at the top of the bed. This is equivalent to finding the saturation at the top of the bed which maximizes the heat flux at the bed top. This may be done by maximizing S with respect to variations in s while holding z equal to the bed thickness. Physically, the saturation which is being varied is the effective saturation at the top of the bed. This process of maximizing the bed power (or heat flux) with respect to variation in the saturation is exactly the procedure first suggested by Hardee and Nilson [8]. The process is very meaningful physically, contrary to some criticism [39]. However, it is now seen that for very deep beds it is the saturation at the top of the bed which is varied, rather than the average saturation. But this is reasonable since both the vapor and liquid flow resistances are greatest at the top of a very deep bed. The same maximizing procedure will yield the dryout flux in Equation (5-1), but only if the inlet flux w is either held constant or expressed as an explicit function of the saturation at the bed top.

At this point it becomes necessary to reconcile the double-valued saturation curve in Figure 5-1 with the single-valued solution to the one-D model described previously (e.g., Figures 4-3a and 4-3b). Capillary force becomes negligible as the particle diameter or the bed thickness becomes larger. Thus Figure 4-3b is more applicable. As the capillary force is reduced, the sub-dryout curves in Figure 4-3b become the large-saturation curves in Figure 5-1. The true incipient dryout curve for Figure 4-3B should extend down to the graph origin, and corresponds to the small saturation branch at dryout in Figure 5-1. The upper portion of the curves in Figure 4-3b become horizontal and vanish. Thus the

lower-power curves in Figure 4-3b (in which saturation increases with elevation) is due to gravity. In Figure 5-1, a boundary condition of $s = 1$ at the bed bottom is very reasonable since there is no vapor generated below that elevation. It is only the existence of capillary force which reverses this situation in shallow beds such as in Figure 4-3.

5.2 Uniform Bed on a Cooled Plate (Downward Boiling)

If a uniform bed is resting on an impermeable, but bottom-cooled plate, some of the heat generated in the bed will be removed downward. Early models assumed that the downward heat flow would be by conduction through a subcooled zone at the bed bottom, and that all heat generated above that subcooled zone would be removed upward by boiling [12,16]. The downward heat flux in this case may be easily determined to be

$$q_{\text{down}} = \sqrt{2k_b (T_s - T_b)S} \quad (5-3)$$

where k_b is the bed conductivity, T_s is the coolant boiling temperature, T_b is the bed bottom temperature, and S is the volumetric heat source.

For this mode of heat removal to be effective, both large bed conductivities and large temperature differences are needed. The former limits the use of bottom-cooling primarily to sodium filled beds (because of the low conductivity of water). The latter demands a low thermal resistance in the support plate so that a large temperature difference does not occur across the plate and force the bed bottom temperature to near T_s .

Recognition of capillary forces acting in a bed leads to another possible mechanism of downward heat removal which could be greater than conduction. In many beds of interest, capillary forces are stronger than gravitational forces. Thus, if an adequate supply of liquid were maintained at both the top and the bottom of the bed, capillary forces would draw the liquid into the bed from both above and below. This may be seen in Figure 5-2. When the decay heat vaporizes some of the liquid in the bed, the vapor is driven out of the bed (both upward and downward). Downward-flowing vapor is not possible in a pool,

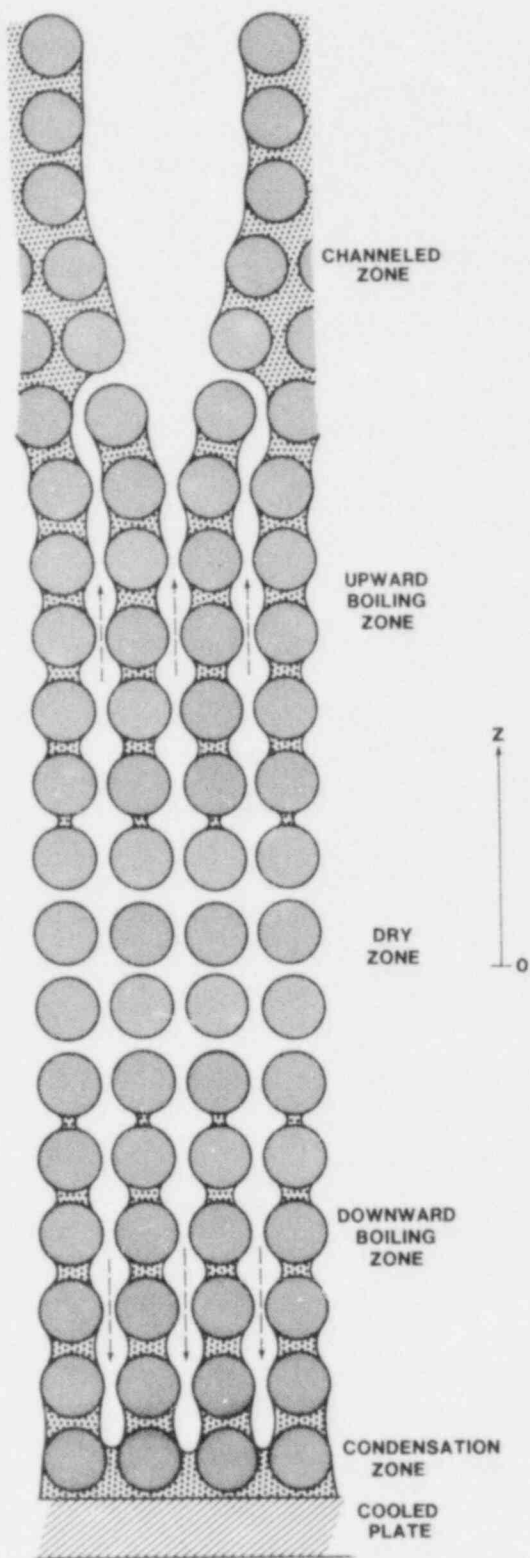


Figure 5-2. Downward Boiling in a Bottom-Cooled Bed.

but is possible in debris because of the continuous vapor paths established and the pressure gradient allowed by capillary force. Normally the downward-driven vapor would collect at the bottom support plate, build up a back pressure, and stop the vapor flow. However, if the support plate were cool enough to condense all the vapor (or if the plate were permeable) the vapor flow could continue and the condensed liquid (or new liquid passing upward through a permeable plate) could be drawn back up into the bed by capillary force. This process may be called "downward boiling" and can be just as effective at heat removal as upward boiling (if the capillary force is much greater than the gravitational force). (The prediction of, and equations for downward boiling were first presented by Lipinski [27].)

Equation (3-21) allows for downward boiling since the plane where $z = 0$ is defined at the location where $q = 0$. Thus the plane of $z = 0$ divides the upward boiling zone from the downward boiling zone. (See Figure 5-2.) In Equation (3-21), a local heat flux (q) less than zero indicates downward boiling. (For example, if the curves in Figure 4-3a were extended downward, they would represent a downward boiling zone.)

Figure 5-3 shows the saturation in a sodium- UO_2 bed 150 mm thick with 0.3 mm diameter particles, 40 percent porosity, 300°C of top subcooling, and a fixed downward flux of 100 kW/m². (The thickness of the top subcooled zone is calculated according to the series conduction model with the Kampf-Karsten bed conductivity and McDonald-Connolly temperature drop in the pool, as described in Reference 30.) Curves for various powers are shown. The elevation is shown with respect to the bottom of the bed (and thus is different than "z"). Channeling is assumed to be suppressed by the subcooling (based on empirical information from Reference 53), and the top subcooled zone thickness decreases with increasing power. As the total bed power increases, the plane separating upward from downward heat flow moves downward. The saturation minimum occurs near this separation plane (see also Figure 5-2) and this is what helps to draw the liquid into the bed from both above and below.

For low powers (e.g., 275 and 300 W/kg- UO_2) the saturation reaches unity above the bed bottom. This indicates that a bottom subcooled zone of the appropriate thickness must exist in order to maintain the specified downward heat flux of 100 kW/m². Low enough bed bottom

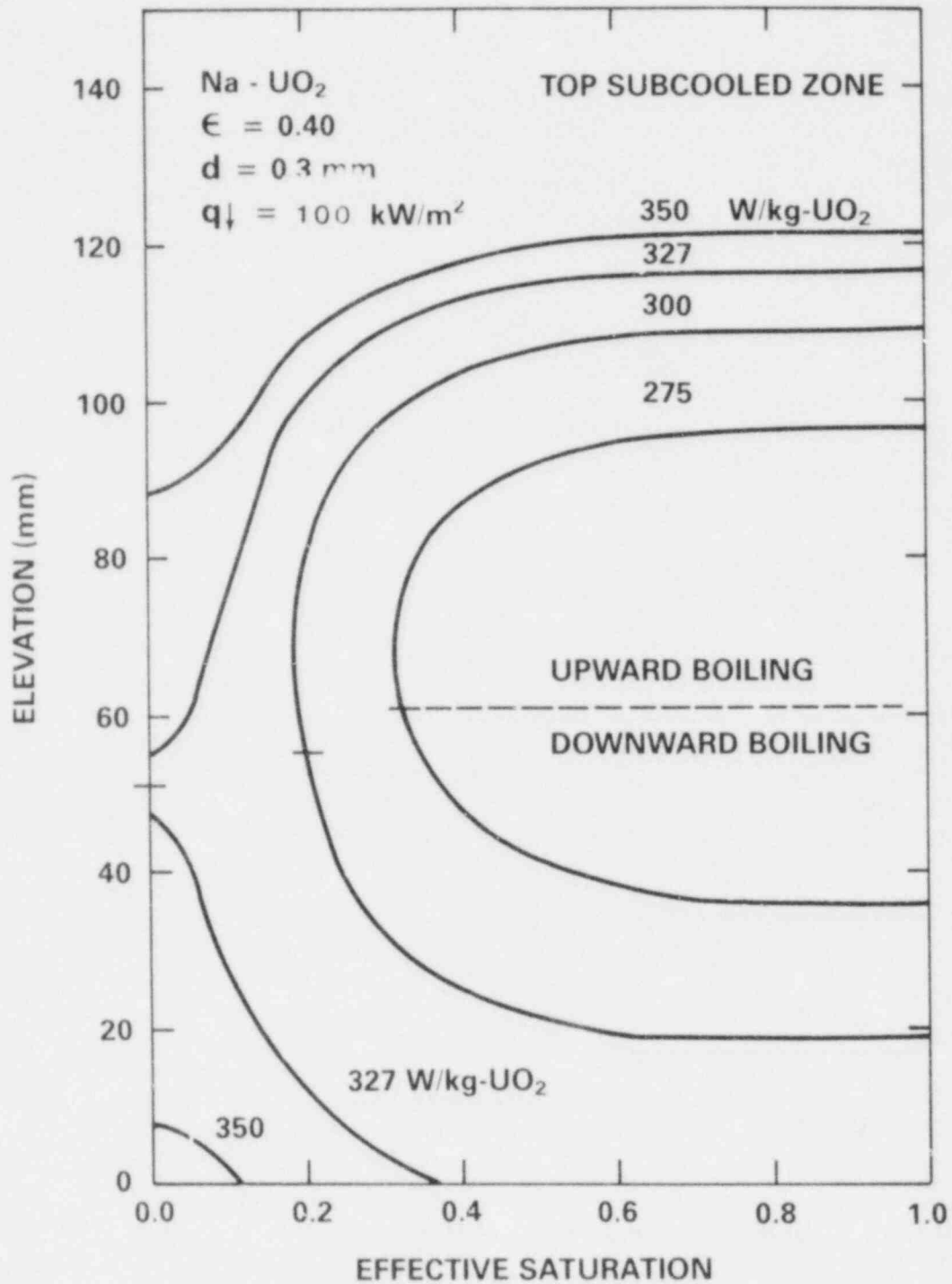


Figure 5-3. Effective Saturation in a 150-mm Thick Sodium-UO₂ Bed With 300°C Top Subcooling and a Fixed Downward Flux of 100 kW/m². The division between upward and downward boiling is marked by ticks.

temperatures must be established by the bottom-cooling device to assure this. (A bottom series conduction model (see Section 2.2) must be used for the subcooled zone.) For higher powers (e.g., 327 and 350 W/kg-UO₂) the saturation is between zero and one on the bed bottom. This implies a minimal subcooled zone only thick enough to condense the downward flowing vapor.

At 327 W/kg-UO₂ dryout occurs at the heat flux separation plane. Heat removal within the dry zone is only by conduction and radiation since there can be no steady-state vapor flow from the lower boiling region to the upper boiling region. Half of the heat in the dry zone goes up and half goes down. Thus the maximum temperature difference above boiling in the dry zone is about one-fourth what it would be in a dry zone of the same thickness and power on an adiabatic bottom. For larger powers the dry zone grows both upward and downwards. At some power it reaches the bed bottom and subsequently grows only upward.

Downward boiling was first noted experimentally by Barleon, Werle, and Lipinski [53]. They measured the heat flux coming from the base of a bottom-cooled water-bronze bed 200 mm thick with 0.26 mm diameter particles and 37.3 percent porosity. They also measured (with thermocouples) the thickness of the bottom subcooled zone and calculated the heat generated within the subcooled zone. The measured downward flux was found to be greater than the heat flux from the heat generated in the subcooled zone alone. (The ratio was 3:1 at dryout.) This indicates that heat generated above the subcooled zone was being delivered downward by downward boiling.

The existence of downward boiling will enhance debris coolability over that expected from downward conduction through a subcooled zone and could influence the design of bottom-cooled core retention devices.

5.3 Uniform Bed on a Permeable Plate

It is possible for debris to be supported on a permeable plate with flow entering the bed from below. For example, in a light water reactor the degraded core may rest on the permeable grid spacers and core support plate, as in Figure 5-4. Without forced flow from the main pumps, liquid may still be driven through the bed either through coolant injection or an excess head in the downcomer and steam generator. Under these conditions, the inlet liquid mass flux (w) in Equation (3.21) is

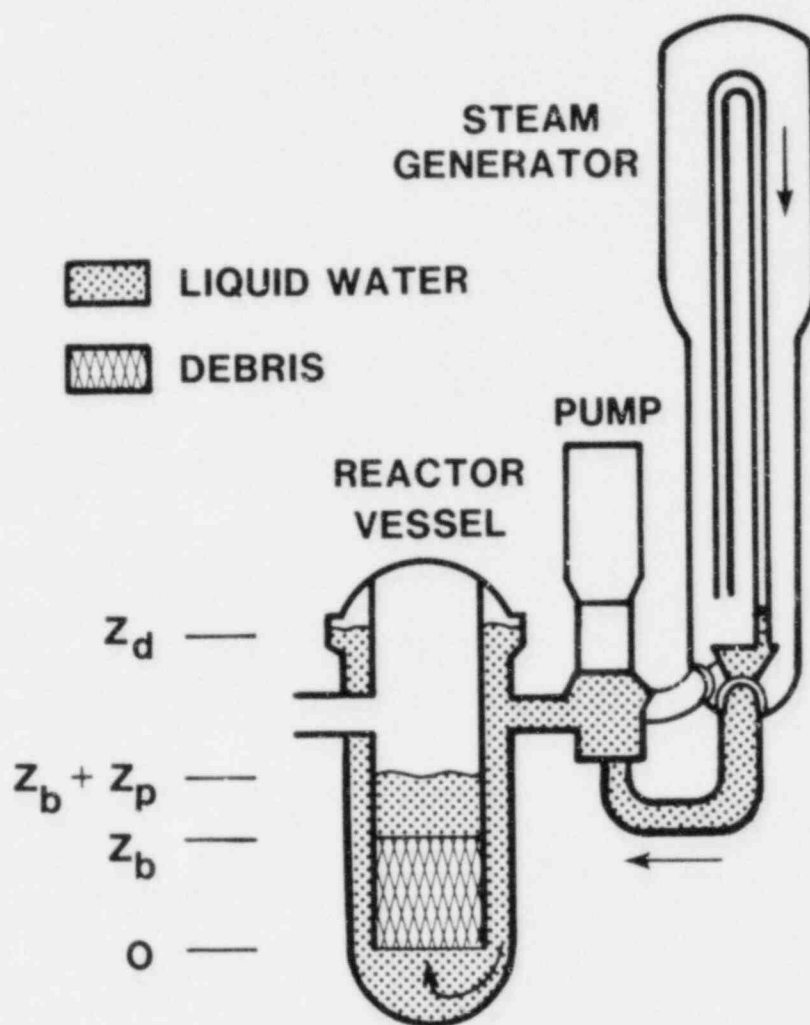


Figure 1.3-8. Bottom-Fed Debris in Typical PWR. Bed Thickness is Z_b , Pool Thickness is Z_p , and Downcomer Head is Z_d .

Figure 5-4. Situation for Inlet Flow Through a Bed Resting on a Permeable Plate.

greater than zero. If the inlet liquid is subcooled the location of $z = 0$ is defined in the bed as the plane where boiling occurs. For a uniformly-heated bed the distance above the bed bottom is

$$L_{sc} = \frac{w\Delta T C_p}{S} \quad (5-4)$$

where ΔT is the subcooling, C_p is the specific heat of the liquid, and S is the volumetric power. The saturation profile in a bed with an inlet liquid flux is similar to the profile shown in Figures 4-3a and 4-3b. However, one interesting feature is that although the vapor flow is always upward, the liquid flow is downward in the top of the bed and upward at the bottom of the bed. The location of the liquid stagnation plane occurs where $q = wh_{1v}$ and thus rises as w increases.

Often one knows or regulates the pressure across the bed rather than the inlet liquid flux. Thus Equation (3-27) must be integrated over the bed to obtain the total pressure drop across the bed. The inlet flux is varied numerically until the desired pressure drop is obtained. (With subcooled inlet flow, Equation (3-1) must be used in the nonboiling region.)

Figure 5-5 shows the dryout power vs. pressure gradient across a bed at dryout with inlet flux (w) as a parameter. The water-UO₂ bed is 500 mm thick with 40 percent porosity and 1 mm diameter particles. Both the overlying pool and inlet water are non-subcooled. The condition with $w = 0$ corresponds to a bed on an impermeable plate. The pressure across the bed for this condition is less than the hydrostatic head equal to the bed thickness (see top scale in Figure 5-5). This is because the liquid displaced by the vapor causes a greater decrease in pressure than the increase caused by the resistance to vapor flow. As the inlet flux is increased, both the dryout power and the pressure drop across the bed increase. However, the increase in pressure drop is initially slower than the increase in dryout power. Thus, for example, a 16% increase in hydrostatic head across the bed will double the dryout power with respect to $w = 0$. This marks a substantial increase in debris coolability.

An additional benefit of an inlet liquid flux is its influence on post dryout behavior. For a deep bed

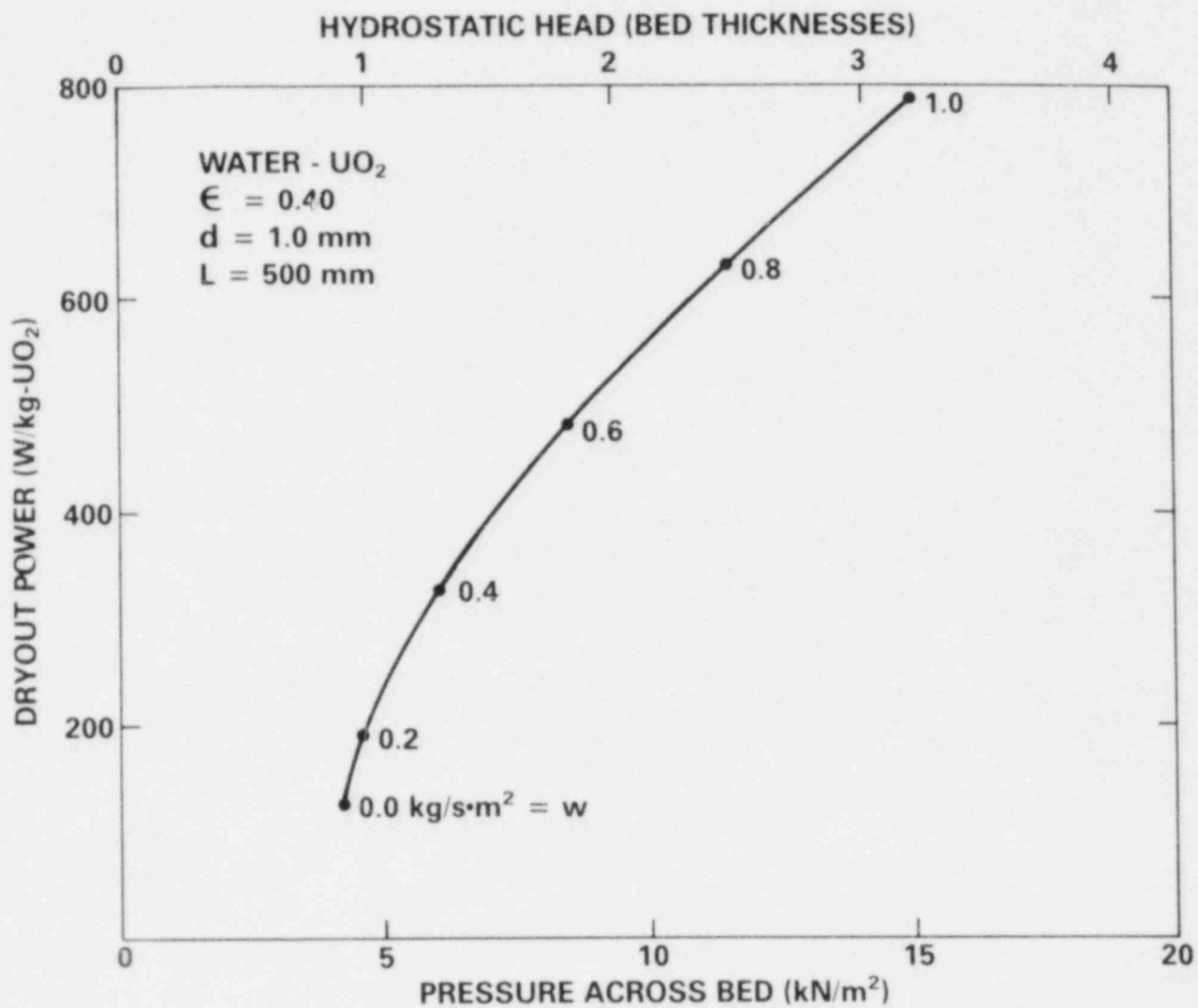


Figure 5-5. Dryout Power vs. Pressure Drop Across a Bed With Inlet Flow for a Water-UO₂ Bed 500-mm Thick With 40% Porosity, 1-mm Diameter Particles, and Various Flows.

on an impermeable support, the dry zone extends to nearly the entire bed with powers slightly above the dryout power. The temperature in the dry zone is very large since heat is removed solely by conduction and radiation until melt occurs. But with an inlet liquid flux, the dry zone is limited to the top of the bed. This causes the zone to be significantly thinner. In addition, inlet flow allows the dry zone to be cooled by steam flow. The temperature rise in the dry-zone is then determined by the vapor specific heat and the mass flow, since mixing assures good heat transfer from the debris to the vapor. The temperature at a particular elevation will increase approximately linearly with elevation and inversely with inlet flux.

In the case of very deep beds, the saturation profile may be obtained (easily) from Equation (5-1). The pressure drop is still obtained by integrating Equation (3-27) numerically. When dryout occurs, the dry zone extends from the stagnation plane (where $q = wh_{1v}$) to the bed top. But after dryout, the pressure drop calculation is valid only in the boiling zone. In the dry zone, Equation (3-1) must be used for the vapor flow. Thus the inlet flow will change when dryout occurs if the pressure across the bed is kept constant. This again makes post-dryout calculations difficult.

The model predictions may be compared with data obtained by Naik and Dhir [39] for water flowing into an inductively-heated steel bed. Unfortunately they always used low enough powers so that $q < wh_{1v}$ (i.e., the stagnation plane was pushed up past the top of the bed). Thus dryout was never achieved. They also expressed their results in terms of a constant exit quality x_e , which may be related to bed heat flux q and inlet flux w by

$$q = x_e wh_{1v} \quad (5-5)$$

where h_{1v} is the heat of vaporization. The closest to dryout they achieved was with $x_e = 0.8$. This data, for the largest and smallest particle diameter used, is compared with the present model predictions in Figure 5-6. The pressure drop across the boiling zone (normalized to the hydrostatic head equal to the boiling zone thickness) is plotted versus inlet mass flux. Since their data was insensitive to bed thickness, a thickness of 200 mm was

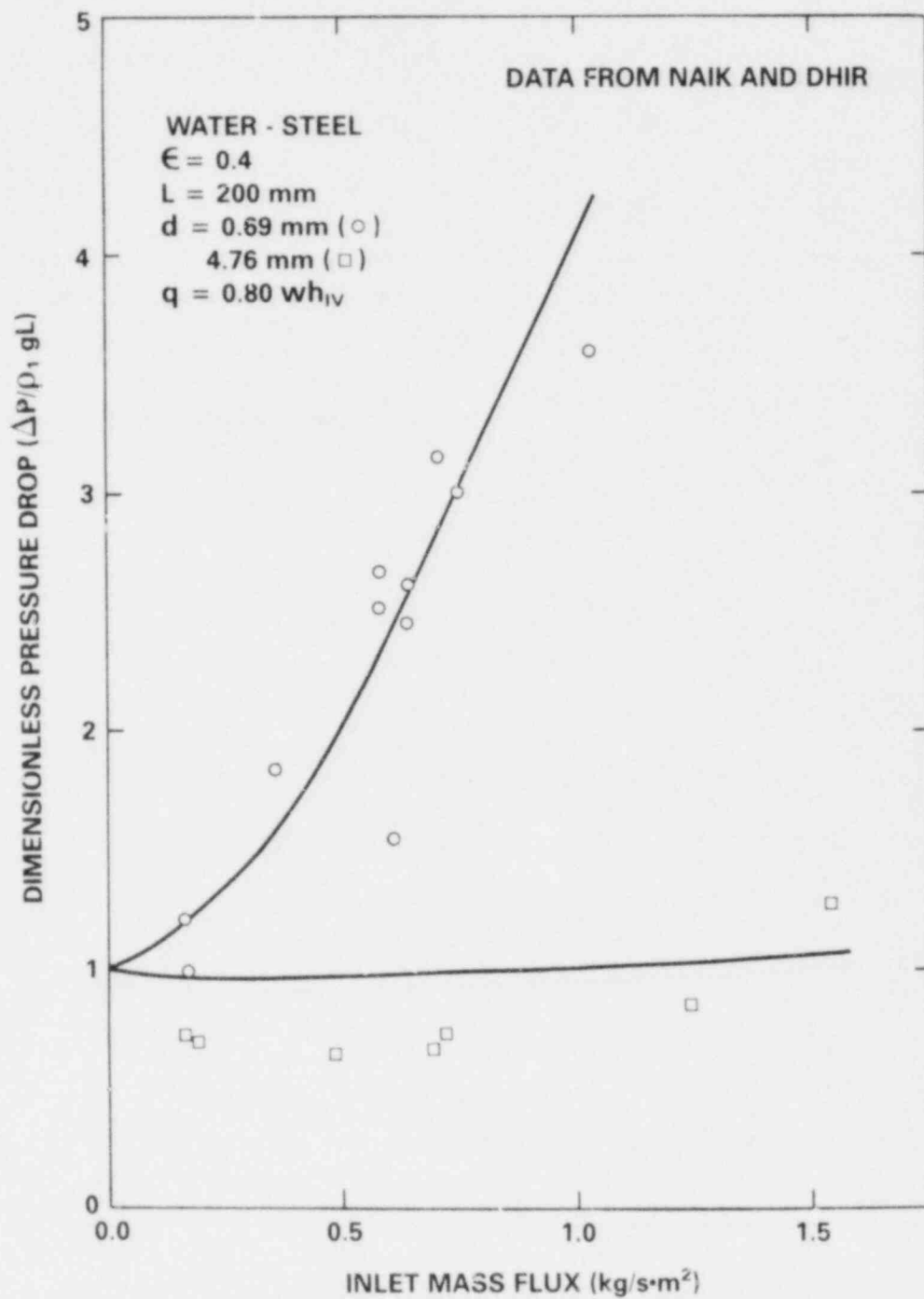


Figure 5-6. Measured Pressure Drop Across a Bed With Inlet Flow Compared With the Model

arbitrarily chosen for the calculation. As can be seen, the agreement with the data is good. (With other qualities and particle diameters similar results are obtained.)

5.4 Stratified Beds

Following formation of debris in a reactor accident, the particles might settle through a thick liquid layer before forming a bed. In such a case the large particles would settle faster and the bed would become stratified, that is, the particle diameter and porosity would be a function of elevation in the bed. Depending on the bed formation history and distance the particles fall, there would be many possible stratified configurations. A limiting case is complete stratification, in which the particle diameter decreases monotonically with elevation.

Equation (3-21) can explicitly handle stratified beds since all parameters in it may be functions of elevation. It is presently the only model for boiling in debris capable of handling stratification (except for the early one-D model of Lipinski and Rivard [16]). The top boundary condition is the same as for a uniform bed, with the channel criterion [Equations (3-26) and (3-28)] applying to the particle diameter and porosity at the base of the channel. This requires iteration to solve. In addition, in a partially stratified bed, every elevation above the base of the channel must be able to support the channel. (This condition is always satisfied in uniform or completely stratified beds.)

There are two major differences in the boiling behavior of a stratified bed as compared to a uniform bed. First, the dryout flux tends to be dictated by the conditions near the top of the bed. This is because the largest liquid flow and vapor flow in the bed must pass through the top layer. Indeed, for very deep beds, Equation (5-1) indicates that the dryout flux is determined entirely by the conditions in the top layer (see Section 5.1). This means that the dryout flux in a very deep, fully stratified bed, is equal to the dryout flux in a bed of the same thickness composed entirely of the particles size (and porosity) in the top layer.

The second difference is described by the second term in Equation (3-21). This term is zero for uniform beds but is present for stratified beds. Its value is the opposite of the gravitational term. This indicates

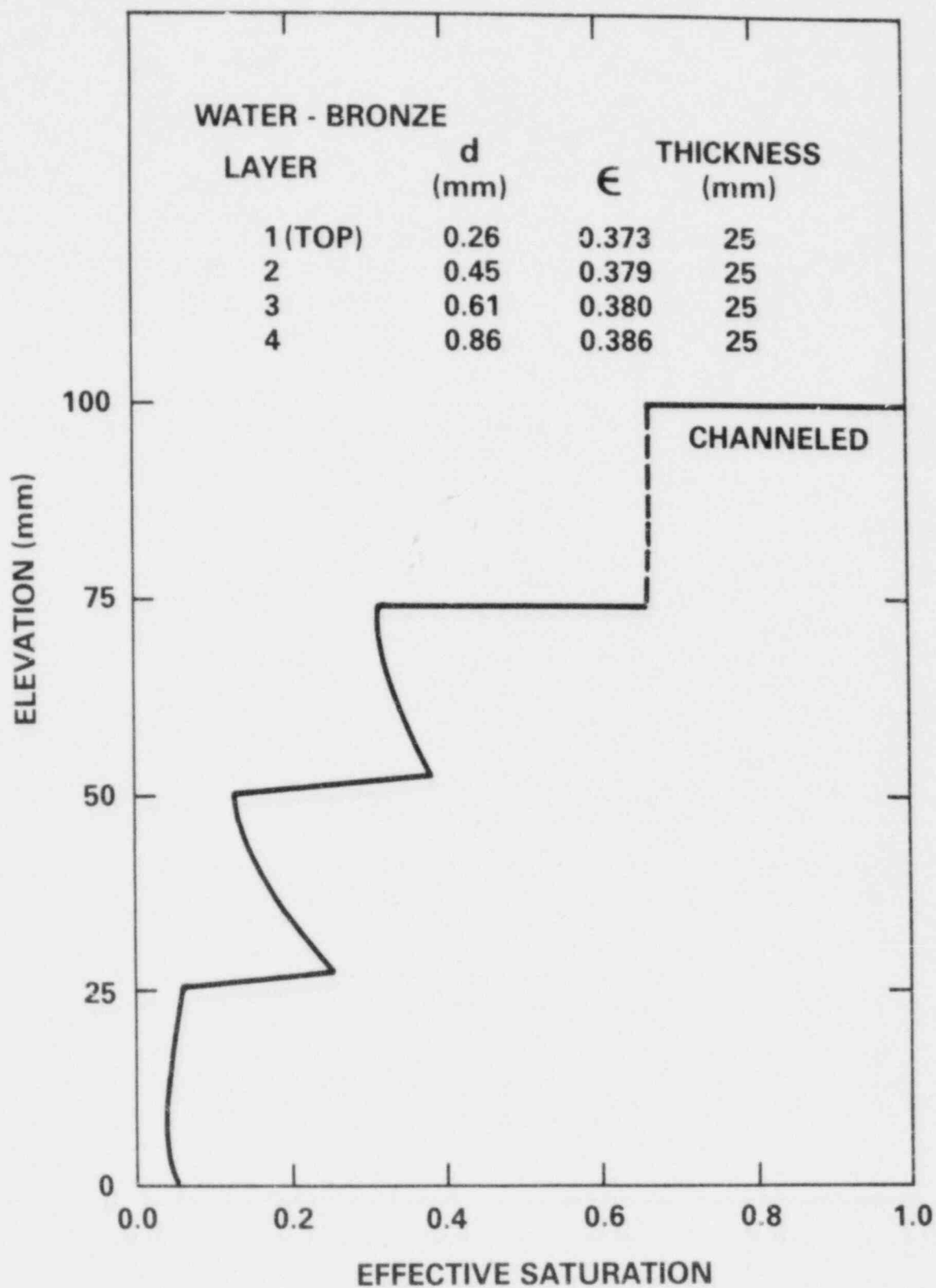


Figure 5-7. Saturation vs. Elevation in a Stratified Bed of Constant 40% Porosity and Four 25-mm Layers of Particle Diameters 0.86, 0.61, 0.45, and 0.26 mm (Bottom to Top)

that in a stratified bed capillary force draws the liquid up toward the region of smallest particles. This retards the downward liquid flow and yields a lower dryout flux. The amount of reduction depends on the gradient of the particle diameter. Combined, these two effects produce a much lower dryout flux in a stratified bed than in a comparable mixed bed.

Figure 5-7 shows the curious behavior of the liquid fraction in a discretely stratified bed. The bed is composed of four layers 25-mm thick each. The particle diameter and porosity for each layer are given in the figure. The power is just below dryout. The sharp change in saturation at the bottom two layer interfaces is due to continuity in flow resistance while the permeability undergoes a step change. This behavior has been observed qualitatively in stratified experiments by Barleon, Werle, and Lipinski [53].

Channels are predicted to penetrate the top layer, but not into the second layer. Thus it is not clear how much of the step change in saturation from the top interface should be used (from the second term in Equation 3-21). It is arbitrarily decided to use half. In this case, the predicted dryout flux is 54.4 kW/m^2 , and the observed dryout flux is 33 kW/m^2 [53]. If the same bed is mixed, the average particle diameter by Fair and Hatch [55] (see Section 5.6) is 0.28 mm. The predicted dryout flux is then 93.2 kW/m^2 and the observed is 80 kW/m^2 [53]. Stratification is seen to decrease the dryout flux in this case.

In order to compare in general the dryout flux in a stratified bed to that in a bed with the same particles uniformly mixed, one must decide on a particle size spectrum to use and also determine what is the dryout flux in a uniform bed with that spectrum of particle sizes. An arbitrarily chosen spectrum for the example is:

$$\phi = \frac{d - d_m}{d_M - d_m} \quad (5-6)$$

where ϕ is the weight fraction of particles less than diameter d , and where d_m and d_M are the minimum and maximum particle sizes in the distribution. The Fair-Hatch

[55] formula defines an average particle size in a distribution which can be used directly in the Equation (3.21). (This will be described more fully in Section 5.6.) The Fair-Hatch effective diameter for the distribution described in Equation (5-6) is

$$d_e = \frac{d_M - d_m}{\ln (d_M/d_m)} \quad (5-7)$$

(The particles are assumed spherical for simplicity.)

In a stratified bed with uniform porosity, the particle diameter at elevation z is then simply

$$d = d_M - (d_M - d_m) \frac{z}{L} \quad (5-8)$$

where L is the bed thickness. To keep the range small, d_m and d_M will be restricted to

$$\frac{d_M}{d_m} = 5. \quad (5-9)$$

One may rearrange Equations (5-7) and (5-9) to obtain

$$d_m = .402 d_e \quad (5-10)$$

$$d_M = 2.012 d_e \quad (5-11)$$

With the above definitions of particle size spectrum and average diameter, the dryout flux of stratified and mixed beds may be compared. (The stratified bed will not have discrete layers since the particle diameter varies smoothly.) Figure 5-8 shows the dryout flux for uniform and stratified beds versus particle size distribution, with the distribution characterized by d_{ave} . The bed is UO_2 (spheres) in non-subcooled sodium, 200-mm thick, with 40 percent porosity, and on an adiabatic impermeable plate. The dryout flux is reduced by stratification in

SODIUM

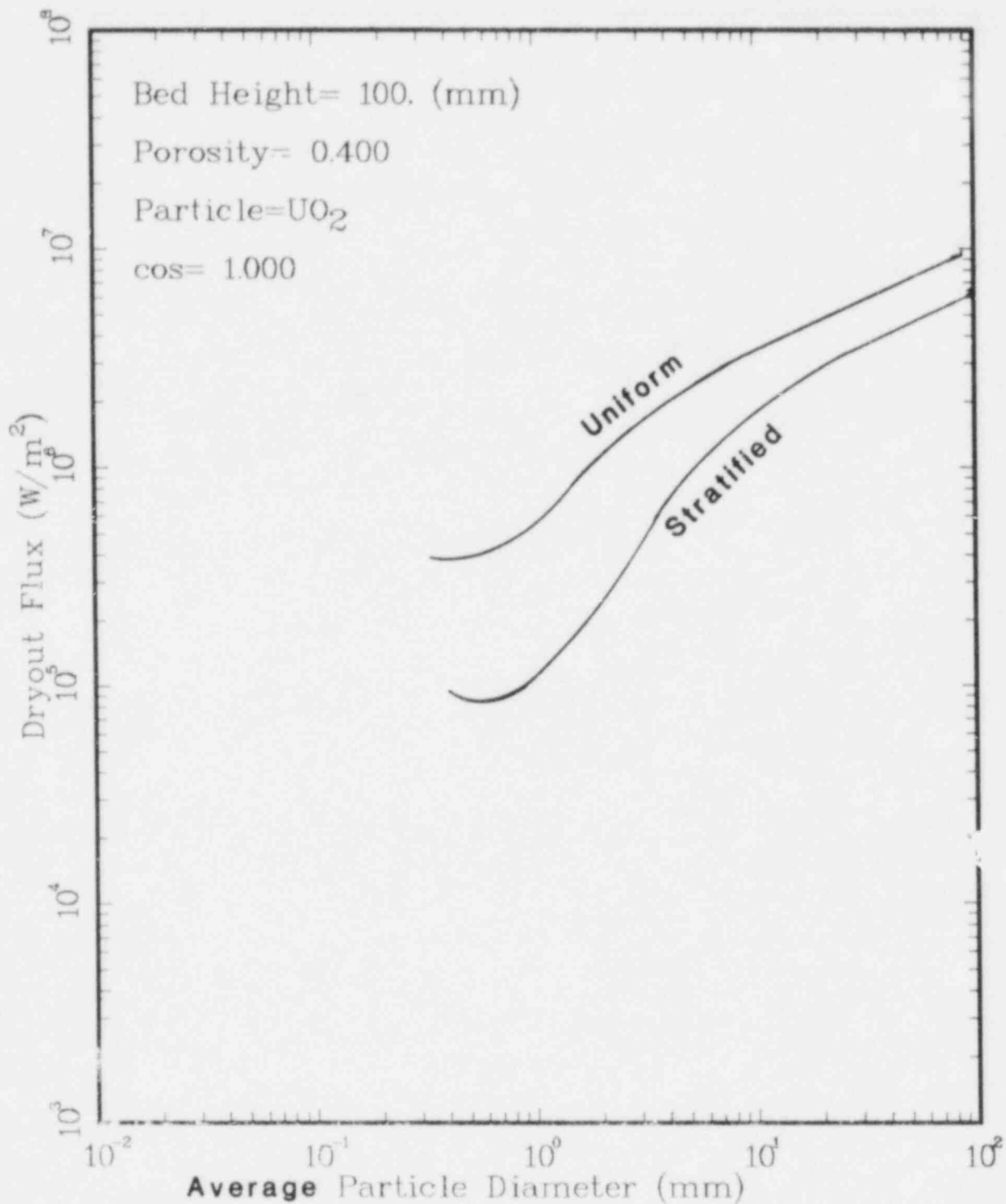


Figure 5-8. Dryout Flux vs. Average Particle Size in a Stratified Bed and Corresponding Mixed Bed of Sodium and UO₂, 100-mm Thick With 40% Porosity.

all cases. Two distinct regions can be seen. With large particles, capillary force is negligible and dryout is dictated by the top layer of particles. Thus it follows by a constant amount below the mixed dryout curve. For small particles capillary force tends to hold the liquid near the bed top and the dryout flux is reduced even more.

The dryout flux in a stratified bed with a subcooled fluid deserves special note. In order to achieve channel penetration with sodium, either large power or low subcoolings are needed to reduce the subcooled zone thickness.

With large power, dryout will occur. Therefore, to achieve channel penetration before dryout requires low subcooling. With stratification, extremely low subcoolings are required (less than 100°C). Thus, channel penetration in stratified LMFBR beds may be very unlikely. This may be an advantage to experimental simulation since it may be possible to achieve dryout before channeling in a subcooled stratified bed with water, which would make experimental investigation of packed stratified beds easier. But care must be taken to avoid flashing disturbances (see Section 2.1).

5.5 Bottom-Heated Beds

The one-D model allows for a volumetric power which varies with elevation. An extreme example of a non-uniform source is bottom heating. The one-D model predicts a reduction in dryout flux by two for small particles but no change with large particles. The data of Barleon and Werle [33] shows a reduction by two for small particles, as predicted, but there is also a factor of two reduction for large particles contrary to prediction. Thus the model must be assumed to be in error by as much as a factor of two for bottom-heated beds with large particles. The reason for this error is not known.

5.6 Non-Spherical Particles and Damaged Fuel Pin Bundles

The model developed and nearly all of the data considered has involved single-sized spherical particles. Beds of such particles obviously do not occur in reactor accidents. Rather, the particles are rough and involve a

spectrum of sizes. However, the model can be easily applied to such conditions simply by defining a proper effective diameter.

As mentioned in Section 2.2, Fair and Hatch [55] studied flow through distributions of soil particles and recommended a formula for permeability based on particle size distribution and roughness. (LeRigoleur [11] noted the relevance of this work to debris coolability.) The formula yields an equation for an effective particle diameter:

$$d_e = f_s \left(\sum_i \frac{w_i}{d_i} \right)^{-1} \quad (5-12)$$

where w_i is the weight fraction of particles with sieve diameter d_i , and f_s is a shape factor which is 1 for spheres and 0.78 for rough particles.

Dhir [17] compared this formula with dryout in inductively-heated distributions of steel spheres and found the formula to work well except when very small (spherical) particles (0.1 mm or less) are included in the distribution.

Squarer et al. [49] also measured dryout with spherical particle distributions and again found the formula to work reasonably well. They noted that the porosity can be much lower in a distribution and it is important to insert this lower porosity in the dryout formula. (The correction term they derived for porosity changes is mathematically equivalent to inserting the correct porosity in the dryout formula they used.) They suggest an alternate formula using the standard deviation of the size distributions.

A severely damaged pin bundle is another example of accident "debris" which may be difficult to cool and which is not a bed of uniform spheres. But, again, the present model can be applied (in many cases) if an effective "particle" size can be defined.

The extreme case is an undamaged pin bundle. In that case, with laminar flow, the momentum equation (Equation 3-1) becomes the Hagen-Poiseuille law for flow through channels:

$$\bar{v}_{loc} = \frac{d_h^2}{32\mu} \frac{dP}{dz} \quad (5-13)$$

where \bar{v}_{loc} is the average velocity of the fluid between the pins and d_h is the hydraulic diameter. This equation is not exact, but use of a hydraulic radius is a common approximation for non-cylindrical channels. For a square lattice of pins with pitch (spacing) p :

$$d_h = \frac{4(p^2 - \pi d_p^2/4)}{\pi d_p} \quad (5-14)$$

where d_p is the pin diameter. But in the laminar case Equation (3-1) is expressed in terms of porosity (ϵ) and superficial velocity (v):

$$v = - \frac{d^2 \epsilon^3}{150(1 - \epsilon)^2 \mu} \frac{dP}{dz} \quad (5-15)$$

For a square pin bundle the porosity is

$$\epsilon = \frac{p^2 - \pi d_p^2/4}{p^2} \quad (5-16)$$

which may also be expressed as

$$1 - \epsilon = \frac{\pi d_p^2}{4p^2} \quad (5-17)$$

The superficial velocity is

$$v = \epsilon v_{loc} \quad (5-18)$$

Inserting Equations (5-14) and (5-16) through (5-18) into Equation (5-13) and reducing yields

$$v = - \frac{d_p^2 \epsilon^3}{32(1 - \epsilon)^2 \mu} \frac{dP}{dz} \quad (5-19)$$

Notice that the porosity dependence is exactly the same as in Equation (5-15). This is no accident. The equations for porous media were derived from channel considerations in a manner very similar to that just described. Equation (5-19) will match Equation (5-15) exactly if the effective spherical diameter is

$$d_e = 2.2 d_p \quad (5-20)$$

In the turbulent limit, the channel flow equation is

$$v_{loc}^2 = - \frac{d_h}{2f\rho} \frac{dP}{dz} \quad (5-21)$$

where f is a channel friction factor and is nearly constant. The turbulent limit of Equation (3-1) is

$$v^2 = - \frac{\epsilon^3 d}{1.75(1 - \epsilon)^2} \frac{dP}{dz} \quad (5-22)$$

Substitution and reduction as above yields agreement between the two equations (with matching porosity dependence) if

$$d_e = \frac{1.75 d_p}{2 f} \quad (5-23)$$

With $f = .004$, this becomes

$$d_e = 220 d_p$$

(5-24)

Inserting the laminar and turbulent effective particle diameters into the deep-bed laminar and turbulent limits of the present model yields the result that the dryout flux is about 5 and 15 times greater, respectively, for an intact pin bundle than for a bed of spheres of diameter equal to the pin diameter and bed porosity equal to the bundle porosity. This demonstrates the advantage of straightening the tortuous flow paths in a debris bed. Again, it must be emphasized that the use of Equations (5-20) and (5-24) is only as accurate as the hydraulic diameter assumption for a pin bundle.

For a damaged bundle, the effective diameter is less than for an intact bundle. Unfortunately there is no way to quantify the amount at this time. One further note (suggested by E. D. Gorham - Berg on): for slightly damaged pins the dryout flux is predicted to be so large that phenomena not included in the model become important. Possible phenomena are burnout on a pin or particle surface with liquid adjacent to it or entrainment of liquid droplets in the vapor flow. In these regimes the model will fail. But such large powers are well beyond the typical decay heat levels following a reactor accident.

5.7 Subcooled Sodium-UO₂ Bed

Heat removal from UO₂ debris in a subcooled sodium pool is of particular interest to the safety of liquid metal fast breeder reactors. Because of the large thermal conductivity of sodium, subcooling the overlying pool (below the boiling point) can have a strong influence on the dryout flux of the debris. Initially one would expect that with the additional heat removal mechanism of conduction, the dryout flux should be increased by subcooling. However, research with sodium-UO₂ debris beds in the D series at Sandia National Laboratories [10,12,18,30,47,51,54] has led to another possibility. It was proposed [30,54] that the subcooled sodium induced a subcooled zone at the top of the bed which suppressed the formation of vapor channels. Without these low-resistance vapor paths, the dryout flux in a subcooled bed would actually be less than in a non-subcooled bed. This channel suppression phenomenon was described in Section 2.1 and 3.3.2, and can be accommodated by the present model (as described in Section 3.3.2).

The D-series experiments have used fission-heated UO_2 particles in subcooled beds. The bed parameters are summarized in Table 5-1. Because the first four tests used a mixture of particle sizes, the average particle size as defined by the Fair-Hatch formula (see Section 5.6) is used in the table and the model. In order to compare the present model predictions with the dryout data from the D-series, the effect of heat removal by conduction or convection to the subcooled pool must be determined. Rivard [9,12,16] has proposed that a subcooled zone overlies a boiling zone in the bed (see Section 2.1), and that the boiling zone thickness would be

$$L_b = \sqrt{L^2 - 2k_b (T_s - T_t)/S} \quad (5-25)$$

where L is the total bed thickness, k_b is the effective bed conductivity, T_s is the sodium saturation temperature, T_t is the temperature at the top of the bed, and S is the volumetric source. Rivard suggests that the temperature difference between the pool and the top of the bed may be determined by the McDonald-Connolly relation [59]. For the D-series this reduces to

$$T_t - T_p = \left(\frac{q}{2400} \right)^{0.75H} \quad (5-26)$$

where q is the heat flux from the bed (in W/m^2) and T is in $^{\circ}C$.

The effective bed conductivity k_b is suggested in reference 30 to be determined by the Kampf-Karsten relation [76] when the sodium is stagnant in the bed:

$$k_{kk} = k_f \left[1 - \left[\frac{(1 - \epsilon)(1 - k_p/k_f)}{k_p/k_f + (1 - \epsilon)^{1/3} (1 - k_p/k_f)} \right] \right] \quad (5-27)$$

Table 5-1. Debris-Bed Experiment Parameters [18,51,54]

Parameter	D-1	D-2	D-3	D-4	D-6
Bed Loading (UO ₂) kg/m ²	300.	600.	899.	454.	600.
Bed Depth, mm	58.	106.*(99.-113)	158.	82.5	114.
Particle Diameter Range, mm	0.1-1.0	0.1-1.0	0.1-1.0	0.1-1.0	0.1-1.0
Ave. Effective Particle Diameter, mm	0.35	0.27	0.29	0.24	(stratified)
Bed Porosity	0.48	0.43	0.43	0.44	0.47
Bulk Sodium Temperatuures, °C	400,500,550,565	400,600	500,400,600	300,600,450	382-590
Saturation Temperatures, °C	900,940,960,955	863,909	918,885,910	760,795,770	885-915
Subcooling, °C	500,440,410,390	463,309	418,485,310	460,195,320	493-325
Max. Specific Power, kW/kg-UO ₂	1.0	1.28	0.43	4.12	0.69

*Average value, bed surface inclined.

where k_f and k_p are the fluid and particle conductivity respectively and ϵ is the bed porosity.

With convection, the following empirical relation was obtained from the D-series [51,54]:

$$k_b = k_{kk} \left(\frac{Ra}{0.76} \right)^{0.34} \quad (5-28)$$

The Rayleigh number is

$$Ra = \frac{k_f \rho_f g \beta_f S L^3}{2 k_{kk}^2 \alpha_f \mu_f} \quad (5-29)$$

where k is thermal conductivity, ρ is density, g is gravitational acceleration, β is volumetric expansivity, k is permeability, S is volumetric power density, L is bed thickness, α is thermal diffusivity, μ is dynamic viscosity, and the subscript f refers to fluid. The sodium is stagnant for $Ra < 0.76$.

With these additional models for conduction and single-phase convection, the dryout predictions of the present model are shown in Figure 5-9 for the beds D-2, D-3, D-4, and D-6. (D-1 did not achieve dryout, and D-6 was run before D-5.) The vertical line in each curve represents the subcooling at which channel formation is predicted. The dryout powers for the channeled and packed states are on to the left and right of the vertical lines respectively. (The channel penetration criterion was fit to the subcooled water-bronze data for Reference 53 with one empirical constant.)

The dryout data from the experiments is also shown. During the operation of some of the tests flashing of superheated liquid sodium occurred which greatly disrupted the beds. Only dryout data from before such disruptions are shown since the bed parameters after disruption are not known. All of the data agrees reasonably well with the predictions for packed-bed dryout. Unfortunately, the D-series has not yet been able to test accurately the channel penetration criterion for sodium. In D-2 channeling

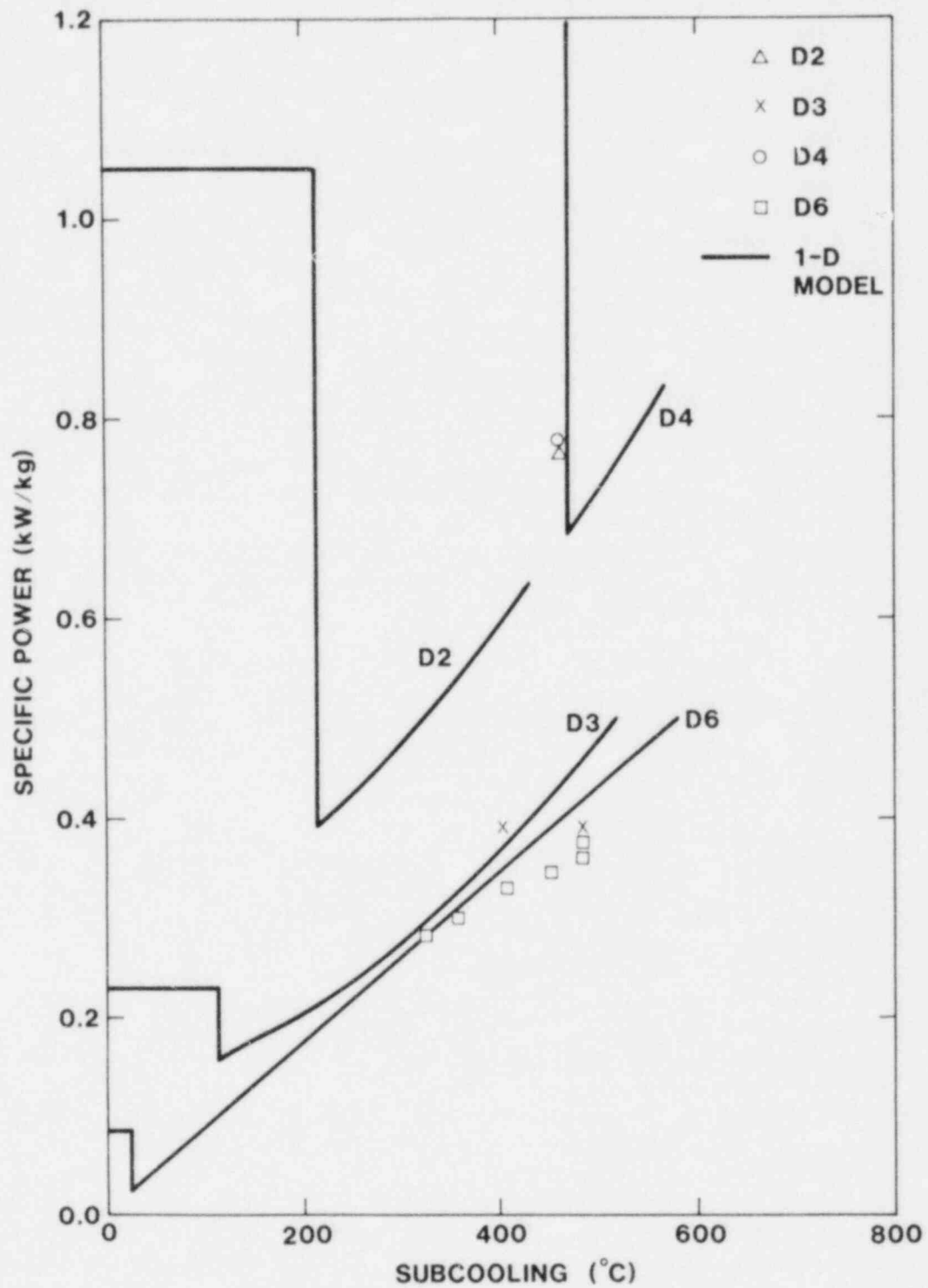


Figure 5-9. Dryout Model Predictions and Data From Subcooled Sodium-UO₂ Data

is predicted at about 200°C subcooling. At 300°C subcooling the power was increased to 1.3 W/g without dryout. However, a large flashing disturbance had occurred before this condition, and the predictions do not apply to the disturbed bed. In D-3 there was no flashing but the subcooling range was too small to test channeling. In D-4 the pre-flash subcooling was on the borderline of predicted channeling, and the bed was found to be packed. Unfortunately, before performing a measurement with 195°C subcooling, flashing occurred. (The dryout power after flashing and with 195°C subcooling was greatly increased to 3.6 W/g.) D-6 was performed with dryout obtained over a wide of subcooling without an occurrence of flashing. Because the bed was stratified, channel penetration was predicted to require very low subcooling (26°C) and indeed the data suggests the bed was packed. After obtaining the initial data a very large flashing event occurred. Afterward the dryout power for all subcoolings was increased by only about 15 percent. This suggests that flashing is not sufficient by itself to cause channeling and a high dryout power in all cases.

The present model is also able to predict the dryout flux of non-subcooled volume-heated sodium-UO₂ beds fairly well, as can be seen in Figure 4-11 in Section 4.3.2. Thus the model can be a useful tool for assessing coolability of post-accident LMFBR debris.

5.8 Summary of Model Features for Other Bed Types

For very deep beds, Equation (3-21) becomes a simple algebraic equation (5-1). The dryout flux is obtained by maximizing the heat flux at the top of the bed with respect to variations in the saturation at the top of the bed. The entire bed is predicted to dry out once the incipient dryout power is exceeded.

Downward heat removal by boiling ("downward boiling") is predicted by the model for a bottom-cooled bed. In this process liquid is drawn up into the bed by capillary force, vapor is driven downward by the resulting pressure gradient, and the vapor is condensed at the cooled base of the bed to be recycled upward. The amount of heat removed downward by boiling is predicted by the model as a function of power and bed condition. The process has been observed experimentally and could influence design of core retention devices.

With a permeable support plate, flow entry into the bed bottom is possible. The model predicts a significant increase in the dryout flux by this process with moderate increase in the pressure drop across the bed. In addition, the dry zone is predicted to occur at the top of the bed rather than the bottom. In this case the zone is cooled by vapor flow and the temperature in the dry zone is significantly cooler than in a zone without inlet flow at the bed bottom. The pressure gradients predicted by the model agree with experimental data.

With a stratified bed, the dryout flux is predicted to be lower than with the same bed uniformly mixed. The reason for this is twofold: First, the top layer (where the liquid and vapor flows are largest) contains the smallest particles. Second, capillary force tends to draw the liquid to the region with the smallest particles, which is at the top of the bed. For very deep beds (in which capillary force is negligible) the model predicts that the dryout flux is the same as in a uniform bed composed entirely of the smallest particles. In a thinner bed the dryout flux would be even lower than in a similar bed composed of the smallest particles. Finally, channeled penetration of a subcooled stratified bed is predicted to require a very small subcooling.

With bottom-heated beds, the model predicts a reduction by two in the dryout flux with small particles but no change with large particles. The model agrees with data from bottom-heated beds in which capillary force is strong. But with large particles, it predicts dryout fluxes which are twice those observed.

The model is directly applicable to debris of non-spherical particles and a spectrum of sizes simply by using an effective particle diameter. An explicit formula for such a diameter is given and has been partially verified experimentally. Similar application to damaged pin bundles is also possible, and formulas for effective diameters are derived.

When compared with all published volume-heated sodium-UO₂ dryout data (including subcooled sodium) the present model performs well for both packed dryout and channeled dryout. However, the precise conditions predicted for channel penetration of a subcooled zone have not been well-tested yet.

6. ZERO-DIMENSIONAL MODEL

The one-dimensional model, as described in Equation (3-21), with the boundary condition described by Equation (3-26) and (3-28) is a first order differential equation which must be solved numerically. The dryout flux can only be obtained iteratively, which means numerically solving the equation many times. In addition, the various features and trends in the model which are displayed in the graphs in Chapters 4 and 5 are not intuitively obvious in Equation (3-21). Fortunately, in the zero-dimensional limit, the one-D model can be reduced to a single algebraic equation. Such an equation is easier and faster to use. In addition, the features of the one-D model are much more apparent. The resulting dryout flux is not much different from the one-D model.

6.1 Zero-D Model Development

The one-D model begins with one-dimensional coupled first-order differential equations and algebraic equations [Equation (3-6), (3-7), (3-13) to (3-16)]. These equations can be reduced to a more convenient algebraic form if the dimension is reduced from one to zero. In such a situation, information about the internal state of the bed is lost, but the improvement in manageability may be worth the loss. It will later be described how this zero-D approximation relates to the more detailed one-D model.

Considering only total flow through the bed, and only total pressure drops across the bed, the one-D model basis equations become

$$\frac{1.75 (1-\epsilon)\rho_v V_v^2}{d\epsilon^3 (1-s)^3} + \frac{150 (1-\epsilon)^2 \mu_v V_v}{d^2 \epsilon^3 (1-s)^3} + \frac{\Delta P_v}{L} + \rho_v g = 0 \quad (6-1)$$

$$\frac{1.75 (1-\epsilon)\rho_l V_l |V_l|}{d\epsilon^3 s^3} + \frac{150 (1-\epsilon)^2 \mu_l V_l}{d^2 \epsilon^3 s^3} + \frac{\Delta P_l}{L} + \rho_l g = 0 \quad (6-2)$$

$$\rho_v V_v h_{1v} = SL = q \quad (6-3)$$

$$\rho_v V_v + \rho_l V_l = w \quad (6-4)$$

$$\Delta P_v - \Delta P_l = \frac{6\sigma(1-\epsilon) \cos\theta}{\epsilon d} \quad (6-5)$$

In these equations, V_v is considered positive and V_l is considered negative, so as to be consistent with the one-D model equations. The heat flux q is that leaving the top of the bed, S is either a uniform or average source, and L is the bed thickness. The saturation s is not explicitly defined, but turns out to be the saturation at the plans of most resistance. Equation (6-4) indicates that the net mass flux through the bed is w . Since q and v_l refer to net quantities, there is no ambiguity over sign as there was in the one-D model (see Section 3.2). Equation (6-5) indicates the total capillary pressure drop between totally wet and totally dry portions of the bed, as proposed by Kozeny [57]. Thus Equation (6-5) makes the above equations apply only to the state of incipient dryout.

Subtracting Equation (6-2) from Equation (6-1) and inserting Equations (6-3), (6-4), and (6-5) yields

$$\begin{aligned} & \frac{1.75 (1-\epsilon)}{\epsilon^3 d h_{1v}^2} \left(\frac{1}{\rho_v (1-s)^3} + \frac{1}{\rho_l s^3} \right) q_d^2 \\ & + \frac{150 (1-\epsilon)^2}{\epsilon^3 d^2 h_{1v}} \left(\frac{\mu_v}{\rho_v (1-s)^3} + \frac{\mu_l}{\rho_l s^3} \right) q_d \\ & + \frac{(1-\epsilon)w}{\epsilon^3 d \rho_l s^3} \left(1.75 w - \frac{3.5}{h_{1v}} q_d - \frac{150 (1-\epsilon) \mu_l}{d} \right) \\ & = \frac{6 \cos\theta \sigma (1-\epsilon)}{\epsilon d L} + (\rho_l - \rho_v) g \end{aligned} \quad (6-6)$$

This is a simple quadratic equation which may easily be solved for the heat flux in terms of the saturation s . The dryout flux may be obtained by maximizing q with respect to variations in s (but only if w is held constant or expressed as an explicit function of s). The physical significance of this is the same as described in Section 5.1. As the bed power is increased, more vapor is produced. This reduces s and allows more room for vapor flow and heat removal. However, at some power the vapor fraction is so large that a subsequent increase would begin to choke off the inflowing liquid. At this power level (and subsequent saturation in the bed), the heat flux from the bed is the maximum possible. A subsequent increase in power will cause dryout. Mathematically maximizing the heat flux q with respect to variation in the effective saturation s mimics this process which occurs in nature. [Caution must be used with $w > 0$. Although the dryout flux is obtained correctly, the pressure drop across the bed is not. Use of Equation (6-1) will yield substantial errors.]

Equation (6-6) is the general zero-D model equation for dryout with moderately deep to very deep beds, small to large particles, and arbitrary inlet flow. The slightly more restricted case of a bed on an impermeable support (i.e., $w = 0$) has been studied extensively experimentally. This restriction simplifies the equation, and all subsequent discussion in this chapter will assume no inlet flow.

For a bed on an impermeable plate, $w = 0$ and Equation (6-6) becomes

$$q_d = \left(\frac{q_T^4}{4q_L^2} + q_T^2 \right)^{1/2} - \frac{q_T^2}{2q_L} \quad (6-7)$$

where

$$q_L = \frac{(\rho_1 - \rho_V) g d^2 \epsilon^3 h_{1V}}{150 (1 - \epsilon)^2} \left(\frac{\mu_V}{\rho_V (1-s)^3} + \frac{\mu_1}{\rho_1 s^3} \right)^{-1} \left(1 + \frac{\lambda_C}{L} \right) \quad (6-8)$$

$$q_T = \left[\frac{(\rho_1 - \rho_V) g d \epsilon^3 h_{1V}^2}{1.75 (1 - \epsilon)} \left(\frac{1}{\rho_V (1-s)^3} + \frac{1}{\rho_1 s^3} \right) \left(1 + \frac{\lambda_C}{L} \right) \right]^{1/2} \quad (6-9)$$

$$\lambda_c = \frac{6 \sigma \cos \theta (1 - \epsilon)}{\epsilon d (\rho_l - \rho_v) g} \quad (4-1)$$

This form is particularly useful because Equation (6-8) is the heat flux in the laminar limit (in which the first term in Equation (6-6) is negligible) and Equation (6-9) is the heat flux in the turbulent limit (in which the second term in Equation (6-6) is negligible).

The last equation defines the capillary head λ_c (which was also discussed in Section 4.2), which is the distance which the fluid would be drawn up into a dry bed from below against the force of gravity. It is a measure of the importance of capillary force, and its importance in dryout was first noted (in a slightly different format) by Shires and Stevens [20]. Indeed, for many of the beds possible in LMFBR accidents or used in early experiments, the capillary term dominates. Examples are given in Table 5-1. Since early models did not include this term, the introduction of it was an important step by Shires and Stevens. Note that the other influence of capillary force, i.e., channels, is missing. Thus Equation (6-7) applies only to packed boiling zones. The effect of channels will be added later.

Table 6-1

Capillary Head for Various Fluids With 0.5-mm Diameter Particles and 40% Porosity (Cos = 0.8, except for sodium).

Fluid	λ_c (mm)
Water	89
Sodium	295
Acetone	36
Methanol	36
Freon-113	13
Isopropanol	45

The dryout flux may be obtained by maximizing q in Equation (6-7) with respect to variations in s . In the laminar and turbulent limits, this may be done explicitly and the resulting critical effective saturations are respectively

$$s_L = \left(1 + \left(\frac{\mu_v \rho_1}{\mu_1 \rho_v} \right)^{1/4} \right)^{-1} \quad (6-10)$$

$$s_T = \left(1 + \left(\frac{\rho_1}{\rho_v} \right)^{1/4} \right)^{-1} \quad (6-11)$$

These critical saturations also set bounds on the range that s need be varied over for the general case in Equation (6-7).

In the laminar limit, the dryout flux may be obtained explicitly by inserting Equation (6-10) into Equation (6-8) and reducing:

$$q_d = \frac{(\rho_1 - \rho_v) g d^2 \epsilon^3 h_{1v} (1 + \lambda_c/L)}{150 (1 - \epsilon)^2 \left((\mu_v/\rho_v)^{1/4} + (\mu_1/\rho_1)^{1/4} \right)^4} \quad (6-12)$$

The similarity to the Hardee-Nilson [8] and the Shires-Stevens [20] model [Equations (2-6) and (2-10)] is apparent. The main difference with respect to the Shires-Stevens model is the different viscosity dependence.

In the turbulent limit the dryout flux also may be obtained explicitly by inserting Equation (6-12) into Equation (6-9) and reducing:

$$q_d = 0.756 h_{1v} \left[\frac{\rho_v (\rho_1 - \rho_v) g d \epsilon^3 (1 + \lambda_c/L)}{(1 - \epsilon) (1 + (\rho_v/\rho_1)^{1/4})^4} \right]^{1/2} \quad (6-13)$$

This differs from the Ostensen model [13,41] [Equation (2-9)] primarily by the capillary term and a numerical constant. The similarity between the two models is

somewhat surprising considering the difference in the methods by which they were derived. The Ostensen model was obtained from a flooding correlation by Wallis [57] and involved only the conversion of heat to vapor flow, with no optimization process.

The effect of channels may be added to the zero-D model by Equations (3-28) and (3-30) from the one-D model or by using Equation (3-22) from the channel model by Jones and Baker [31]. To maintain simplicity, and since the two channel models give similar results, the equation of Jones and Baker will be used for the zero-D model, modified by the cosine of the contact angle:

$$L_c = \frac{6 \sigma \cos \theta}{\epsilon d (\rho_p - \rho_l) g} \quad (6-14)$$

Assuming negligible flow resistance in the channel, the dryout flux will be determined by the packed region. Since the source is assumed uniform,

$$\frac{q_d}{q_{6-7}} = \frac{L_T}{L_T - L_c} \quad (6-15)$$

where q_d is the bed flux at dryout, q_{6-7} is the dryout flux using Equation (6-7) with a bed thickness of $L_T - L_c$, and L_t is the total bed thickness. Thus

$$q_d = \frac{q_{6-7}}{1 - L_c/L_T} \quad (6-16)$$

6.2 Features of the Zero-D Model Compared With the One-D Model

The features of the one-D model are now quite apparent in the equations of the zero-D model. Equation (6-16) clearly shows that as the channel length approaches the bed thickness (L_c approaches L_T), the dryout flux becomes very large. Equation (6-16) shows that the effect of channels is limited to beds in which L_c is comparable

to L_T . With $L_T \gg L_C$, Equation (6-7) applies. This equation shows that the dryout flux still has a dependence on bed thickness as long as λ_C is comparable to L . Thus the three ranges of bed depth (channeled, moderately deep, and very deep) become clearly identified with $L \approx L_C$, $L \approx \lambda_C$, and $L \gg \lambda_C$. This behavior was seen in the one-D model in Figure 4-9.

Equation (6-12) shows that in the laminar limit with very deep beds ($\lambda_C \ll L$) the dryout flux varies with the square of particle diameter. With strong capillary force ($\lambda_C \gg L$), inserting Equation (6-10) yields the dryout flux depending linearly on particle diameter. In the turbulent limit Equation (6-13) shows that with $\lambda_C \ll L$, the heat flux varies with the square root of particle diameter. These dependencies were seen in the one-D model in Figure 4-6.

Equation (6-13) shows that in the laminar very deep limit, the dryout flux varies with $\epsilon^3/(1-\epsilon)^2$, which is approximately the fifth power of porosity. But with $\lambda_C > L$, the porosity dependence in λ_C [Equation (6-10)] drops this to $\epsilon^2/(1-\epsilon)$, or approximately the third power of porosity. Equation (6-14) shows that with turbulence (and $\lambda_C < L$) the dryout flux varies with $(\epsilon^3/(1-\epsilon))^{1/2}$, which is about the square of porosity. These dependencies were seen in Figure 4-14.

Equation (6-13) shows that in the laminar limit the dryout flux depends almost linearly on vapor density as long as the dynamic viscosity is much less with liquid than with vapor. Since vapor density varies nearly linearly at one atmosphere pressure, the dryout flux should vary fairly strongly with pressure. By comparison, Equation (6-14) indicates that the dryout should vary less strongly for large particles (near one atmosphere pressure). This behavior was seen in Figure 4-13.

6.3 Mathematical Relation Between the Zero-D and One-D Models

The similarity between the zero-D and one-D models may be seen in various limits of the one-D model. With very deep beds, the zero-D and one-D models yield exactly the same relation for bed heat flux as a function of effective saturation at the bed top. This can be seen by comparing Equation (6-6) with $\lambda_C = 0$ and Equation (5-1).

The dryout flux is also exactly the same. However, the pressure drop through the bed, which is an important parameter in determining w in cases with inlet flow, can only be obtained with accuracy from the one-D model.

In the limit of zero inlet flow and of dominant capillary force but no channels, (e.g., a fairly thin bed with heavy particles) an algebraic dryout solution to the one-D model again can be obtained. However, one must also assume uniform conditions (volumetric power, particle diameter, and porosity) and either a laminar or a turbulent limit. The laminar and turbulent limits of Equation (6-6) under these conditions are, respectively,

$$\frac{-5\sqrt{6\sigma} \cos\theta (1-\epsilon)}{\epsilon d} \frac{dJ}{ds} \frac{ds}{dz} = \frac{150 (1-\epsilon)^2 S z}{\epsilon^3 d^2 h_{1v}} \left(\frac{\mu_v}{\rho_v (1-s)^3} + \frac{\mu_1}{\rho_1 s^3} \right) \quad (6-17)$$

$$\frac{-5\sqrt{6\sigma} \cos\theta (1-\epsilon)}{d} \frac{dJ}{ds} \frac{ds}{dz} = \frac{1.75 (1-\epsilon) S^2 z^2}{\epsilon^3 d h_{1v}^2} \left(\frac{1}{\rho_v (1-s)^3} + \frac{1}{\rho_1 s^3} \right) \quad (6-18)$$

In the laminar limit, Equation (6-17) may be rearranged to obtain

$$z dz = \frac{-\sigma \cos\theta \epsilon^2 d h_{1v}}{5\sqrt{6} (1-\epsilon) S} \left(\frac{\mu_v}{\rho_v (1-s)^3} + \frac{\mu_1}{\rho_1 s^3} \right)^{-1} \frac{dJ}{ds} ds \quad (6-19)$$

Integrating Equation (6-19) and rearranging yields a relation between z and s :

$$z = \left[L^2 - \frac{2 \sigma \cos \theta \epsilon^2 d h_{1v}}{5 \sqrt{6} (1-\epsilon) S} \int_1^s \left(\frac{\mu_v}{\rho_v (1-s)^3} + \frac{\mu_1}{\rho_1 s^3} \right)^{-1} \frac{dJ}{ds} ds \right]^{1/2} \quad (6-20)$$

Dryout will occur when $s = 0$ at $z = 0$. Then

$$q_d = \frac{-2 \sigma \cos \theta \epsilon^2 d h_{1v} \rho_v}{5 \sqrt{6} (1-\epsilon) L \mu_v} \int_0^1 \left(\frac{1}{(1-s)^3} + \frac{\mu_1 \rho_v}{\mu_v \rho_1} \frac{1}{s^3} \right)^{-1} \frac{dJ}{ds} ds \quad (6-21)$$

In the limit of negligible gravitational force, the zero-D laminar dryout condition [Equation (6-12)] becomes

$$q_d = \frac{\sigma \cos \theta \epsilon^2 d h_{1v} \rho_v}{25 (1-\epsilon) L \mu_v} \left(1 + \left(\frac{\mu_1 \rho_v}{\mu_v \rho_1} \right)^{1/4} \right)^{-4} \quad (6-22)$$

The similarity with Equation (6-21) is apparent. The ratio of the one-D dryout flux to the zero-D dryout flux (in the laminar-capillary limit) is

$$f_L = - \frac{2.5}{\sqrt{6}} \left(1 + \left(\frac{\mu_1 \rho_v}{\mu_v \rho_1} \right)^{1/4} \right)^4 \int_0^1 \left(\frac{1}{(1-s)^3} + \frac{\mu_1 \rho_v}{\mu_v \rho_1} \frac{1}{s^3} \right)^{-1} \frac{dJ}{ds} ds \quad (6-23)$$

This ratio is a function of Leverett function and the ratio of the vapor to liquid dynamic viscosities. The dryout flux ratio f_L is fit very well by the function

$$f_L = 0.500 \left(\frac{\mu_v \rho_l}{\mu_l \rho_v} \right)^{0.0785} \quad (6-24)$$

It varies from 0.5 to 0.9 for the fluids of interest. Thus the one-D dryout power is not too much different than the zero-D dryout power. This is fortunate since the zero-D dryout power is much easier to calculate than the one-D dryout power.

In the turbulent-capillary limit (which is difficult to achieve physically but shall be presented for completeness), Equation (6-18) may be rearranged and integrated to

$$z = \left[L^3 - \frac{3 \cdot 5 \sqrt{6} \sigma \cos \theta \epsilon^2 h_{1v}}{1.75 s^2} \int_1^s \left(\frac{1}{\rho_v (1-s)^3} + \frac{1}{\rho_l s^3} \right)^{-1} \frac{dJ}{ds} ds \right]^{1/3} \quad (6-25)$$

At dryout,

$$q_d = \left[\frac{-3.5 \sqrt{6} \sigma \cos \theta \epsilon^2 h_{1v} \rho_v}{1.75 L} \int_0^1 \left(\frac{1}{(1-s)^3} + \frac{\rho_v}{\rho_l s^3} \right)^{-1} \frac{dJ}{ds} ds \right]^{1/2} \quad (6-26)$$

The zero-D turbulent-capillary limit [Equation (6-14)] is

$$q_d = \left[\frac{6 \sigma \cos \theta \epsilon^2 h_{1v} \rho_v}{1.75 L} \left(1 + (\rho_v / \rho_l)^{1/4} \right)^{-4} \right]^{1/2} \quad (6-27)$$

The similarity with Equation (6-26) is apparent. The ratio of the one-D dryout flux to the zero-D dryout flux (in the turbulent-capillary limit) is

$$f_T = \left[-3 \frac{5}{\sqrt{6}} \left(1 + (\rho_V/\rho_L)^{1/4} \right)^4 \int_0^1 \left(\frac{1}{(1-s)^3} + \frac{\rho_V}{\rho_L s^3} \right)^{-1} \frac{dJ}{ds} ds \right]^{1/2} \quad (6-28)$$

The dryout flux ratio is fit very well by the function

$$f_T = 0.829 \left(\frac{\rho_L}{\rho_V} \right)^{0.0486} \quad (6-29)$$

The ratio varies from 1.0 to 1.3 for most fluids of interest.

The previous analyses have shown that the dryout heat fluxes predicted by the zero-D and one-D models are very similar in many limits. Given the greater ease with which dryout is obtained with the zero-D model, it is of interest to see how close the two models are between the limits explored.

Figure 6-1 displays the dryout flux vs. particle diameter for uniform water-UO₂ beds on adiabatic impermeable plates with 40 percent porosity and various thicknesses. Both the zero-D and one-D model predictions are shown. The one-D model is based on the equations listed in Section 3.4. The zero-D model is based on Equations (6-7) through (6-11), (6-14), and (6-16). The agreement between the models is close.

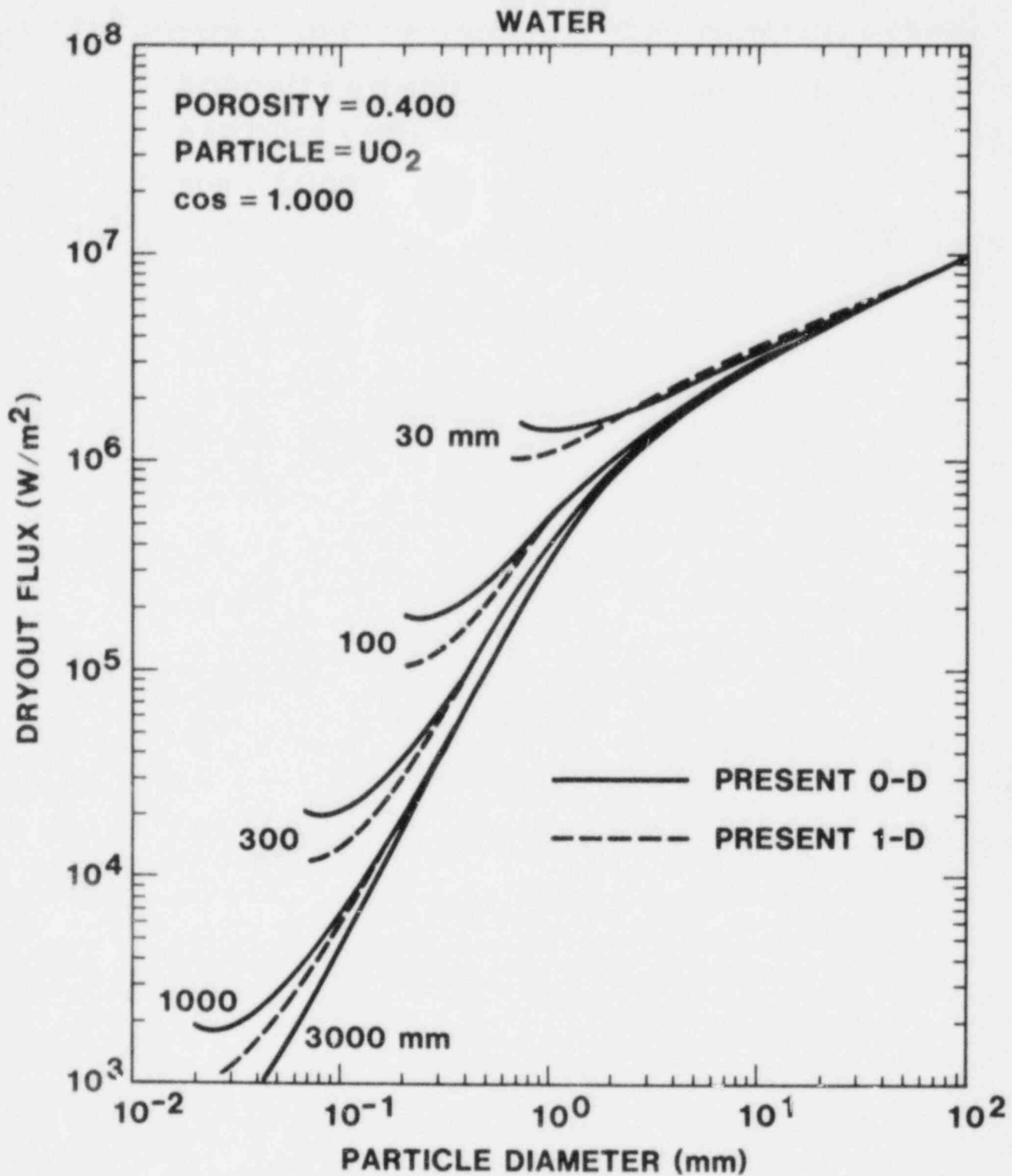


Figure 6-1. Dryout Flux vs. Particle Diameter for a Water-UO₂ Bed With 40% Porosity and Various Thicknesses as Predicted by the One-D and Zero-D Models.

6.4 Zero-D Dryout Model With Bottom-Cooling for Small Particles

Since the zero-D model contains the effect of capillary force, it is also capable of accommodating downward boiling (described in Section 5.2). Since downward boiling requires a strong capillary force, which in turn exists primarily with small particles and laminar flow, the laminar limit of the zero-D model shall be used [Equation (6-12)].

The upward heat flux at dryout is expressed by Equation (6-12) except that L is replaced by the thickness of the upward boiling region, L_{up} :

$$q_{up} = q_0 \left(\frac{\lambda c}{L_{up}} + 1 \right) \quad (6-30)$$

where

$$q_0 = \frac{(\rho_1 - \rho_v) q d^2 \epsilon^3 h_{1v}}{150 (1-\epsilon)^2 \left(\left(\frac{\mu v}{\rho v} \right)^{1/4} + \left(\frac{\mu_1}{\rho_1} \right)^{1/4} \right)^4} \quad (6-31)$$

The downward flux at dryout is

$$q_{down} = q_0 \left(\frac{\lambda c}{L_{down}} - 1 \right) \quad (6-32)$$

where L_{down} is the thickness of the downward boiling region and q_{down} is a positive number. For a uniform source (which is a basic assumption in a zero-D model),

$$q_{up} = \frac{L_{up} q}{L} \quad (6-33)$$

$$q_{\text{down}} = \frac{L_{\text{down}} q}{L} \quad (6-34)$$

where q is the total heat flux (up and down) from the bed at dryout:

$$q = q_{\text{up}} + q_{\text{down}} \quad (6-35)$$

Inserting Equation (6-33) into Equation (6-30), and Equation (6-34) into Equation (6-31) yields

$$q_{\text{up}} = \frac{q_0}{2} + \sqrt{\frac{q_0^2}{4} + \frac{\lambda_c q_0 q}{L}} \quad (6-36)$$

$$q_{\text{down}} = \frac{-q_0}{2} + \sqrt{\frac{q_0^2}{4} + \frac{\lambda_c q_0 q}{L}} \quad (6-37)$$

Combining Equations (6-35), (6-36) and (6-37) yields

$$q = \left(\frac{2\lambda_c}{L} + \sqrt{\left(\frac{2\lambda_c}{L}\right)^2 + 1} \right) q_0 \quad (6-38)$$

This defines the total heat flux at dryout from the bed in terms of bed parameters. Inserting Equation (6-38) into Equations (6-36) and (6-37) yields (with some difficulty):

$$q_{\text{up}} = \left(\frac{\lambda_c}{L} + \frac{1}{2} + \sqrt{\left(\frac{\lambda_c}{L}\right)^2 + \frac{1}{4}} \right) q_0 \quad (6-39)$$

$$q_{\text{down}} = \left(\frac{\lambda_c}{L} - \frac{1}{2} + \sqrt{\left(\frac{\lambda_c}{L}\right)^2 + \frac{1}{4}} \right) q_0 \quad (6-40)$$

This defines the upward and downward fluxes at dryout in terms of bed parameters. Equations (6-39) and (6-40) also indicate that

$$q_{up} = \frac{q + q_0}{2} \quad (6-41a)$$

$$q_{down} = \frac{q - q_0}{2} \quad (6-41b)$$

The factor by which the total heat flux from the bed is multiplied when downward boiling is permitted is found by dividing Equation (6-39) by Equation (6-12):

$$r = \frac{\frac{2\lambda_c}{L} + \sqrt{\left(\frac{2\lambda_c}{L}\right)^2 + 1}}{\frac{\lambda_c}{L} + 1} \quad (6-42)$$

This ratio varies between 1 and 4 as the importance of capillary force (λ_c/L) varies from 0 to ∞ . Table 3 gives examples of this ratio for various fluids with a 100 mm thick bed with 0.5 mm diameter particles and 40 percent porosity. As can be seen, downward boiling can significantly increase the power required to achieve dryout, especially in shallow beds. However, this effect can also be achieved by conduction in bottom-subcooled sodium-UO₂ beds. Thus the additional effect of downward boiling is not as strong in that case.

Table 3

Ratio of Dryout Powers With Downward Boiling to That Without Downward Boiling for $L = 100$ mm, $\delta = 0.5$ mm, and $\epsilon = 0.4$ for Various Fluids

Fluid	λ_c (mm)	Ratio
Water	89	2.02
Sodium	295	3.01
Acetone	36	1.44
Methanol	36	1.44
Freon-113	13	1.14
Isopropanol	45	1.55

6.5 Summary of the Zero-D Model

The one-D model can be simplified to an algebraic equation using a zero-dimensional approximation the resulting zero-D model applies primarily to uniform beds without channels. The criterion for dryout is Equation (6-7), with the heat flux (q) being maximized as the saturation (s) is varied between the values given in Equations (6-10) and (6-11). In the laminar and turbulent limits, Equations (6-12) and (6-13), respectively, (which are simpler) are valid. Channelled beds can be accommodated via Equation (6-16). Downward boiling in bottom cooled beds can be accommodated by Equations (6-38), (6-39), and (6-40).

The dryout flux predicted by the one-D and zero-D models agree closely for most cases. (See Figure 6-1.) The predictions of both models agree well with nearly all published volume-heated dryout measurements.

7. SUMMARY

Over the last ten years experiments and modeling of dryout in particle beds have produced over fifty papers. Considering only volume-heated beds, dryout measurements have been made for over 260 different beds involving six different fluids have been made (water, acetone, freon-113, methanol, isopropanol, and sodium) and five different solids (steel, bronze, copper, lead, and urania). Particle diameter has ranged from 0.26 mm to 16 mm, bed thickness from 15 mm to 450 mm, and resulting dryout heat flux from 16 kW/m² to 4300 kW/m². These volume-heated data are consolidated in Appendix A.

At least fifteen models to predict dryout have been produced. Six of them have been based on flooding and are nearly identical. The dependence of the dryout flux on particle diameter is predicted to range from square to square root, the dependence on bed thickness from strong to none, and on porosity from about fifth power to zero power. The most involved models include gravity and capillary force, and allow for laminar or turbulent flow. Models to predict channel length in a bed have also been developed. This report gives a more complete description of the derivation of some of that past modeling effort by the author, and introduces some additional extensions and improvements.

The model described in this report is for one-dimensional boiling and dryout in a porous medium and is based on conservation laws for mass, momentum, and energy, with separate equations for liquid and vapor flow. It includes the effects of both laminar and turbulent flow, two-phase friction, and capillary force. The boundary condition at the bed bottom includes the possibility of inflowing liquid and either an adiabatic or a bottom-cooled support structure. The top of the bed may be either channeled or subcooled. In the first case the channel length and the saturation at the base of the channels are predicted. In the latter case, a criterion for penetration of the subcooled zone by channels is obtained. With the different possible boundary conditions, and wide range of applicability, the model is very general.

The basic equations for the model are Equations (3-13), (3-21), (3-26), and (3-28). (Symbols are defined in the nomenclature.)

$$\begin{aligned}
& - \frac{\sqrt{150} \cos \theta \sigma (1 - \epsilon) dJ ds}{\epsilon d} - \sqrt{150} \cos \theta \sigma J \frac{d}{dz} \left(\frac{1 - \epsilon}{\epsilon d} \right) + (\rho_1 - \rho_v)g \\
& = \frac{1.75(1 - \epsilon)q^2}{\epsilon^3 d h_{1v}^2} \left(\frac{1}{\rho_v(1 - s)^3} + \frac{1}{\rho_1 s^3} \right) \\
& + \frac{150(1 - \epsilon)^2 q}{\epsilon^3 d^2 h_{1v}} \left(\frac{\mu_v}{\rho_v(1 - s)^3} + \frac{\mu_1}{\rho_1 s^3} \right) \\
& + \frac{(1 - \epsilon)w}{\epsilon^3 d p_1 s^3} \left(\frac{+ 1.75 w}{-} + \frac{3.5q}{h_{1v}} - \frac{150(1 - \epsilon)\mu_1}{d} \right)
\end{aligned}$$

for $q > wh_{1v}$ (3-21)

where J is the Leverett function, and is suggested to be

$$J = \frac{(s-1 - 1)0.175}{\sqrt{5}} \quad (3-13)$$

Equation (3-21) applies only to the packed boiling zone in the bed.

If the bed is channeled, the saturation at the top of the packed region is defined as

$$\begin{aligned}
& \frac{(1 - \epsilon)q_c}{\epsilon^3 d \rho_v g h_{1v} (1 - s)^3} \left(\frac{1.75 q}{h_{1v}} + \frac{150(1 - \epsilon)\mu_v}{d} \right) = \\
& p(1 - \epsilon) + \rho_1 \epsilon \quad (3-28)
\end{aligned}$$

where q is the heat flux at the base of the channels, whose length is

$$L_c = \frac{\sqrt{150} \cos \theta \sigma J}{\epsilon d (\rho_p - \rho_l) g} \quad (3-26)$$

The model is assumed inapplicable if the channel length exceeds half the bed thickness. If the bed is subcooled, channel suppression may occur, as described in Section 3.3.2.

For a uniform bed on an adiabatic impermeable support the model predicts channel lengths which are similar to that predicted by Jones and Baker [31], but which increase slightly with power. For channels to penetrate a subcooled zone, the model requires that the zone be slightly thinner than the resulting channel length. Within the bed, the model predicts that the saturation should increase monotonically with elevation if the particles are small and the bed not too thick. But for thicker beds (or with larger particles), the model predicts a minimum in the saturation near the middle or the top of the bed. All of the above predictions have been noted experimentally, but only qualitatively.

The heat flux at dryout in a uniform bed is predicted to increase with increasing particle diameter, with decreasing bed thickness, with increasing porosity, and with increasing pressure (up to a maximum at about 70 bars with water). The dependency on all these parameters changes depending on whether the bed is channeled, moderately deep, or very deep. The dryout fluxes observed in the literature range from channeled to very deep, from laminar to turbulent, and span 2-1/2 orders of magnitude in dryout flux. The diameter dependence predicted by the model is fairly well verified over the range of 0.25 to 16 mm. The bed thickness dependence is qualitatively observed but there is some disagreement within the data itself for water. The porosity dependence and pressure dependence are as yet not well tested. In general, the 260 data points are correlated by the model with an average error of 60 percent.

For powers above incipient dryout, the model predicts a stable dry zone (up to incipient melt) at the base of the bed which increases with increasing power. The dry zone is generally thicker with deeper beds or larger particles. Good dry zone thickness measurements are as yet unavailable for comparison with the model.

For very deep beds, Equation (3-21) becomes a simple algebraic Equation (5-1). The dryout flux is obtained by maximizing the heat flux at the top of the bed with respect to variations in the saturation at the top of the bed. The entire bed is predicted to eventually dryout once the incipient dryout power is exceeded. Due to experimental difficulties, this prediction is as yet not tested.

Downward heat removal by boiling ("downward boiling") is predicted by the model for a bottom-cooled bed. In this process liquid is drawn up into the bed by capillary force, vapor is driven downward by the resulting pressure gradient, and the vapor is condensed at the cooled base of the bed to be recycled upward. The amount of heat removed downward by boiling is predicted by the model as a function of power and bed condition. The process has been observed experimentally and could influence design of core retention devices.

With a permeable support plate, flow entry into the bed bottom is possible. The model predicts significant increases in the dryout flux by this process with moderate increase in the flow resistance through the bed. In addition, the dry zone is predicted to occur at the top of the bed rather than the bottom. In this case the zone is cooled by vapor flow and the temperature in the dry zone is significantly cooler than in a zone without inlet flow at the bed bottom. The pressure gradients predicted by the model agree with experimental data, but data for dryout are not yet available.

With a stratified bed (in which the smallest particles are at the top), the dryout flux is predicted to be lower than with the same bed uniformly mixed. The reason for this is twofold: First, the top layer (where the liquid and vapor flows are largest) contains the smallest particles. Second, capillary force tends to draw the liquid to the region with the smallest particles, which is at the top of the bed. For very deep beds (in which capillary force is negligible) the model predicts that the dryout flux is the same as in a uniform bed composed entirely

of the smallest particles. In a thinner bed the dryout flux would be even lower than in a similar bed composed of the smallest particles. These predictions need testing.

When compared with all published volume-heated sodium-UO₂ dryout data (including stratified beds and subcooled sodium) the present model performs well for both packed dryout and channeled dryout. The predictions for channel penetration of a subcooled zone have not been accurately tested yet. But channeling in a stratified bed is predicted to require a sodium pool very near the boiling temperature.

With bottom-heated beds the model predicts a reduction by two in the dryout flux with small particles but no change with large particles. The model agrees with data from bottom-heated beds in which capillary force is strong. But with large particles, it predicts dryout fluxes which are twice those observed. The reason for this discrepancy is at present unknown.

The model is directly applicable to debris of non-spherical particles and a spectrum of sizes simply by using an effective particle diameter. An explicit formula for such a diameter is given and has been partially verified experimentally. Similar application to damaged pin bundles is also possible, and formulas for effective diameters are suggested.

The one-D model can be simplified to an algebraic equation using a zero-dimensional approximation. The resulting zero-D model applies primarily to uniform beds without channels. The criterion for dryout is Equation (6-7), with the heat flux (q) being maximized as the saturation (s) is varied between the values given in Equations (6-10) and (6-11). In the laminar and turbulent limits, Equations (6-12) and (6-13), respectively, (which are simpler) are valid. Channeled beds can be accommodated via Equation (6-16). Downward boiling in bottom cooled beds can be accommodated by Equations (6-38), (6-39), and (6-40). The dryout flux predicted by the one-D and zero-D models agree closely for most cases. (See Figure 6-1.) Both models correlate nearly all dryout measurements well.

REFERENCES

1. E. S. Sowa, J. C. Hesson, R. H. Gebner, and G. T. Goldfuss, "Heat Transfer Experiments through Beds of UO_2 in Boiling Sodium," Trans. Amer. Nucl. Soc., 14, 2, 725 (November 1971).
2. J. D. Gabor, J. C. Hesson, L. Baker, Jr., and J. C. Cassulo, "Simulation Experiments on Heat Transfer From Fast Reactor Fuel Debris," Trans. Amer. Nucl. Soc., 15, 2, 836 (November 1972).
3. J. D. Gabor, E. S. Sowa, L. Baker, Jr., and J. C. Cassulo, "Studies and Experiments on Heat Removal for Fuel Debris in Sodium," Proc. of ANS Fast Reactor Safety Meeting, Beverly Hills, CA, April 1974, CONF-740401, 823-844 (April 1974).
4. R. S. Keowin, Dryout of a Fluidized Particle Bed With Internal Heat Generation, M.S. Thesis, University of California, Los Angeles, CA (June 1974).
5. V. K. Dhir and I. Catton, "Prediction of Dryout Heat Fluxes in Bed of Volumetrically Heated Particles," Proc. of Int. Mtg. on Fast Reactor Safety and Related Physics, Chicago, IL, October 5-8, 1976, CONF-761001, 2026-2035 (October 1976).
6. E. S. Sowa, J. D. Gabor, L. Baker, Jr., J. R. Pavlik, J. C. Cassulo, and W. Holloway, "Studies of the Formation and Cooling of Particulate Fuel Debris Beds in Sodium," Proc. of Int. Mtg. on Fast Reactor Safety and Related Physics, Chicago, IL, October 5-8, 1976, CONF-761001, 2036-2044 (October 1976).
7. V. K. Dhir and I. Catton, Study of Dryout Fluxes in Beds on Inductively Heated Particles, NUREG-0252 USNRC, Los Angeles, CA (June 1977).
8. H. C. Hardee and R. H. Nilson, "Natural Convection in Porous Media With Heat Generation," Nuclear Science and Engineering, 63, 119-132 (July 1977).
9. J. B. Rivard, "Preliminary Results From Initial In-Pile Debris Experiments," Proc. of Third PAHR Mtg., ANL-78-10, Argonne Nat. Lab (November 1977).

10. J. B. Rivard, Debris Bed Studies and Experiments at Sandia Laboratories, SAND78-0299, Sandia National Laboratories, Albuquerque, NM (July 1978).
11. C. LeRigoleur, "Particle Bed Dryout in Sodium," Proc. of the Fourth PAHR Info. Exchange Mtg., October 10-12, 1978, Varese, Italy, published in Europ. Appl. Res. Rept. - Nucl. Sci. Technol., 1, 6, 1381-1398 (October 1978).
12. J. B. Rivard, Post-Accident Heat Removal: Debris Bed Experiments D-2 and D-3, SAND78-1238, NUREG/CR-0421, Sandia National Laboratories, Albuquerque, NM (November 1978).
13. R. W. Ostensen, memo to J. B. Rivard, February 12, 1979, Sandia National Laboratories, Albuquerque, NM (February 1979).
14. L. Biasi, L. Castellano, A. Colombo, H. Hohmann, H. Holtbecker, R. Nijsing, H. Shins, and D. Schwalm, "Status and Development of PAHR Research at J.R.C. - Ispra," Proc. of Int. Mtg. on Fast Reactor Safety Tech., Seattle, WA, August 19-23, 1979, Vol. 2, 370-380 (August 1979).
15. J. B. Rivard and R. L. Coats, "Post-Accident Heat Removal: An Overview of Some In-Vessel Safety Considerations," Proc. of the Int. Mtg. on Fast Reactor Safety Tech., Seattle, WA, August 19-23, 1979, Vol. 2, 709-720 (August 1979).
16. R. J. Lipinski and J. B. Rivard, "Debris Bed Heat Removal Models: Boiling and Dryout With Top and Bottom Cooling," Proc. of the Int. Mtg. on Fast Reactor Safety Tech., Seattle, WA, August 19-23, 1979, Vol. 2, 757-769 (November 1979).
17. V. K. Dhir, "Dryout Heat Fluxes in Debris Beds Containing Particles of Different Size Distributions," Proc. of the Int. Mtg. on Fast Reactor Safety Tech., Seattle, WA, August 19-23, 1979, Vol. 2, 770-780 (August 1979).
18. J. B. Rivard, "In-Reactor Experiments on the Cooling of Fast Reactor Debris," Nuclear Technology, 46, 344-349 (December 1979).

19. V. K. Dhir and I. Catton, "Dryout Heat Fluxes in Debris Beds Cooled at the Bottom and Having Sub-cooled Liquid at the Top," Nucl. Tech., 46, 2, 356-361 (December 1979).
20. G. L. Shires and G. F. Stevens, Dryout During Boiling in Heated Particulate Beds, AEEW-M1779, UKAEA, Winfrith, England (April 1980).
21. D. Squarer and J. A. Peoples, "Dryout in Inductively-Heated Bed With and Without Forced Flow," Trans. Amer. Nucl. Soc., 34, 535-537 (June 1980).
22. A. Naik, D. Le, and V. K. Dhir, "Forced Flow Evaporative Cooling of a Volumetrically Heated Porous Layer," Trans. Amer. Nucl. Soc., 34, 537-538 (June 1980).
23. L. Barleon and H. Werle. "Debris Bed Investigations With Adiabatic and Cooled Bottom" Ninth Mtg. of the Liquid Metal Boiling Working Group, Rome, Italy (June 1980).
24. R. Trenberth and G. F. Stevens, An Experimental Study of Boiling Heat Transfer and Dryout in Heated Particle Beds, AEEW-R1342, UKAEA, Winfrith, UK (July 1980).
25. In Report of the Zion/Indian Point Study: Vol. I, Chap. VI, NUREG/CR-1410 or SAND80-0617/1, Sandia National Laboratories, Albuquerque, NM (August 1980).
26. J. D. Gabor, M. Epstein, S. W. Jones, and J. C. Cassulo, Status Report on Limiting Heat Fluxes in Debris Beds, ANL/RAS80-21, Argonne National Laboratory, Argonne, IL (September 1980).
27. R. J. Lipinski, "A Particle Bed Dryout Model With Upward and Downward Boiling," Trans. Amer. Nucl. Soc., 35, 358-360 (November 1980).
28. V. K. Dhir and I. Catton, "Dryout Heat Fluxes in Very Deep Debris Beds," Trans. Amer. Nucl. Soc., 35, 360-361 (November 1980).

29. S. W. Jones, M. Epstein, J. D. Gabor, J. C. Cassulo, and S. G. Bankoff, "Investigation of Limiting Boiling Heat Fluxes From Debris Beds," Trans. Amer. Nucl. Soc., 35, 361-363 (November 1980).
30. J. E. Gronager, M. Schwarz, and R. J. Lipinski, PAHR Debris Bed Experiment D-4, SAND80-2146 NUREG/CR-1809, Sandia National Laboratories, Albuquerque, NM (January 1981).
31. S. W. Jones and L. Baker, Jr., "A Theory for Prediction of Channel Depths," reported in J. D. Gabor et al., Status Report on Debris Accommodation Technology for LBRs, ANL/RAS 81-19, Argonne National Laboratory, Argonne, IL, 5-33 (May 1981).
32. J. D. Gabor and J. C. Cassulo, "Induction Heated-Simulant Materials," reported in J. D. Gabor et al., Status Report on Debris Accommodation Technology for LBRs, ANL/RAS 81-19, Argonne National Laboratory, 34-59 (May 1981).
33. L. Barleon and H. Werle, "Dependence of Dryout Heat Flux on Particle Diameter," Trans. Amer. Nucl. Soc., 38, 382-383 (June 1981); L. Barleon and H. Werle, "Dependence of Dryout Heat Flux on Particle Diameter for Volume- and Bottom-Heated Debris Beds," Primärbericht, No. 01.02.15.PXX, KfK (April 1981).
34. D. H. Cho, L. J. Stachyra, and G. A. Lambert, "Fluidization Considerations in Debris Bed Heat Removal," Trans. Amer. Nucl. Soc., 38, 383-385, (June 1981).
35. V. K. Dhir and L. Barleon, "Dryout Heat Flux in a Bottom-Heated Porous Layer," Trans. Amer. Nucl. Soc., 38, 385-386 (June 1981).
36. R. J. Lipinski, "A One-Dimensional Particle Bed Dryout Model," Trans. Amer. Nucl. Soc., 38, 386-387 (June 1981).
37. D. Squarer, A. T. Pieczynski, and L. E. Hochreiter, "Dryout in Large Particle, Deep Debris Beds," Trans. Amer. Nucl. Soc., 38, 444-445 (June 1981).
38. T. G. Theofanous and M. Saito, An Assessment of Class 9 (Core-Melt) Accidents for PWR Dry-Containment Systems, PNE-81-148, Purdue University, West Lafayette, IN (June 1981).

39. A. S. Naik and V. K. Dhir, "Forced Flow Cooling of a Volumetrically Heated Porous Layer," ASME81-HT-46, 20th Joint ASME/AICHE Nat. Heat Transfer Conf., Milwaukee, WI, August 2-5, 1981 (August 1981).
40. R. E. Henry and H. K. Fauske, "Core Melt Progression and the Attainment of a Permanently Coolable State," Meeting on Light Water Reactor Safety, Sun Valley, ID (August 1981).
41. R. W. Ostensen and R. J. Lipinski, "A Particle Bed Dryout Model Based on Flooding," Nuclear Science and Eng., 79, 110-113 (September 1981).
42. R. Nijssing and A. Schwalm, "A One-Dimensional Computation Method for Predicting the Asymptotic Heat Transfer Behavior of Sodium-Saturated Fuel Particle Beds With Top and Bottom Cooling," Nucl. Eng. and Des., 66, 151-170 (September 1981).
43. D. Schwalm and R. Nijssing, "The Influence of Sub-cooling on Dryout Inception in Sodium-Saturated Fuel Particle Beds With Top Cooling and Adiabatic Bottom," Tech. Note No. 1.06.01.81.118, Joint Res. Center, Ispra, Italy (October 1981).
44. C. Somerton, I. Catton, and L. Thompson, "An Experimental Investigation in Deep Debris Beds," LWR Safety Information Exchange, Gathersburg, MD, October 26-31, 1981 (October 1981).
45. L. Barleon and H. Werle, Dependance of Dryout Heat Flux on Particle Diameter for Volume- and Bottom-Heated Debris Beds, KfK-3138, Kernforschungszentrum, Karlsruhe (November 1981).
46. J. D. Gabor, J. C. Cassulo, S. W. Jones, and D. R. Pedersen, "Studies on Heat Removal From Fuel Debris," Trans. Amer. Nucl. Soc., 39, 642-643 (November 1981).
47. G. W. Mitchell, R. J. Lipinski, and M. Schwarz, "Heat Removal From a Stratified UO₂-Sodium Particle Bed," Trans. Amer. Nucl. Soc., 39, 643-644 (November 1981).
48. D. Squarer, "The Limiting Dryout Flux in a Large Particle Heat Generating Debris Bed," Trans. Amer. Nucl. Soc., 39, 1049-1050 (November 1981).

49. A. W. Reed, The Effect of Channeling on the Dryout of Heated Particulate Beds Immersed in a Liquid Pool, Ph.D. Thesis, Mass. Inst. of Technology, Cambridge, MA (February 1982).
50. D. Squarer, A. T. Pieczynski, and L. E. Hochreiter, "Effect of Debris Bed Pressure, Particle Size, and Distribution on Degraded Core Coolability," Nucl. Sci. and Eng., 80, 2-13 (January 1982).
51. G. M. Mitchell, R. J. Lipinski, and M. Schwarz, Heat Removal From a Stratified UO₂-Sodium Particle Bed, SAND81-1622/NUREG/CR-2412, Sandia National Laboratories, Albuquerque, NM (February 1982).
52. L. Barleon, K. Thomauske, and H. Werle, "Dependence of Dryout Heat Flux on Particle Diameter for Volume-Heated Small Particles Debris Beds," not published, KfK (1982).
53. L. Barleon, H. Werle, and R. J. Lipinski, "Heat Transfer in Particulate Beds," to be published in Proc. of Intern. Topical Mtg. on LMFBR Safety and Related Design and Operational Aspects, Lyon, France, July 19-23, 1982.
54. R. J. Lipinski, J. E. Gronager, and M. Schwarz, "Particle Bed Heat Removal With Subcooled Sodium: D-4 Results and Analysis," to be published in Nucl. Tech. (August 1982).
55. G. M. Fair and L. P. Hatch, "Fundamental Factors Governing Streamline Flow of Water Through Sand," J. Amer. Water Works, 25, 1551-1565 (1933).
56. T. K. Sherwood, G. H. Shipley, and F. A. L. Holloway, "Flooding Velocities in Packed Columns," Ind. Eng. Chem. 30, 765-769 (1938).
57. As reported in A. E. Scheidegger, The Physics of Flow Through Porous Media, University of Toronto Press, Toronto (1960).
58. N. Zuber, "Hydrodynamic Aspects of Boiling Heat Transfer," AEC Report No. AECU-4439, Physics and Mathematics (1959).

59. J. S. McDonald and T. J. Connolly, "Investigation of Natural Convection Heat Transfer in Liquid Sodium," Nucl. Sci. and Eng., 8, 369-377 (1974).
60. G. B. Wallis, One-Dimensional Two-Phase Flow, McGraw-Hill, NY, 326-329, 336-339 (1969).
61. M. C. Leverett, "Capillary Behavior in Porous Solids," Trans. AIME, 142, 152-169 (1941).
62. S. Ergun, "Fluid Flow Through Packed Columns," Chem. Eng. Prog., 48, 89-94 (1952).
63. N. T. Burdine, "Relative Permeability Calculations From Pore-Size Distribution Data," Trans. AIME, 198, 71-77 (1953).
64. A. T. Corey, "The Interrelation Between Gas and Oil Relative Permeabilities," Producers Monthly, edited by J. N. Broston, 19, 1, 38-41 (November 1954).
65. R. H. Brooks and A. T. Corey, "Properties of Porous Media Affecting Fluid Flow," J. of Irrig. and Drainage Div. Proc. of ASCE, 92, IR2, 61-89 (June 1966).
66. G. G. Brown et al., Unit Operations, J. Wiley and Sons, Inc., New York, 210-228 (1950).
67. As reported in R. B. Bird, W. E. Stewart and E. N. Lightfoot, Transport Phenomena, John Wiley and Sons, New York, p. 199 (1960).
68. As reported in J. Bear, Dynamics of Fluids in Porous Media, American Elsevier Publishing Co., New York (1968).
69. Wyckoff and Botset, as reported in Reference 57.
70. H. W. Fox, E. F. Hare, and W. A. Zisman, "Wetting Properties of Organic Liquids on High Energy Surfaces," J. Phys. Chem., 59, 1097 (1955).
71. V. G. Stepanov, L. D. Volyak, and Y. V. Tarlakov, "The Wettability of Metals by Water as a Function of Temperature," Russ. J. of Phys. Chem., 46, (9), 1371 (1972).

72. A. B. Ponter, G. A. Davies, W. Beaton, and T. K. Ross, "The Measurement of Contact Angle Under Conditions of Heat Transfer When a Liquid Film Breaks on a Vertical Surface," Int. J. Heat and Mass Transfer, 10, 1633-1636 (1967).
73. L. D. Volyak, V. G. Stepanov, and Y. V. Tarlakov, "An Experimental Study of the Temperature Variation of the Wetting Angle for Water and Deuterium Oxide on Quartz and Sapphire," Russ. J. of Phys. Chem., 49, 1729 (1975).
74. D. H. Bradhurst and A. S. Buchanan, "Surface Properties of Liquid Sodium and Sodium-Potassium Alloys in Contact With Metal Oxide Surfaces," Australian J. Chem., 14, 397-408 (1961).
75. A. W. Adamson, Physical Chemistry of Surfaces, 3rd Edition, J. Wiley and Sons, New York (1974).
76. H. Kampf and G. Karsen, "Effects of Different Types of Void Volumes on the Radial Temperature Distribution of Fuel Pins," Nucl. Appl. and Tech., 9 (1970).

APPENDIX A

PUBLISHED DRYOUT HEAT FLUX MEASUREMENTS

Table A-I. Measured Dryout Fluxes for Non-Subcooled Volume-Heated Beds at Atmospheric Pressure. All measurements from a single reference in which particle diameters (d), bed thicknesses (L), and material properties are within 15% of each other, and in which porosity (ϵ) is within 5%, have been averaged to one point. The fluids are water (W), acetone (A), methanol (M), freon-113 (F), and sodium (S). The particles are UO_2 (U), steel (S), lead (L), copper (C), and bronze (B).

Fluid- Part.	d (mm)	ϵ	L (mm)	q (kW/m ²)	Reference
W-U	.303	.39	66.	192.	GABOR, ET AL. [3]
W-U	.303	.39	88.	56.	GABOR, ET AL. [3]
W-S	.356	.45	88.	762.	KEOWIN [4,7]
W-S	.503	.45	63.	890.	KEOWIN [4,7]
W-L	.503	.43	69.	750.	KEOWIN [4,7]
W-S	.503	.45	76.	738.	KEOWIN [4,7]
W-L	.503	.43	86.	860.	KEOWIN [4,7]
W-S	.503	.45	89.	760.	KEOWIN [4,7]
W-L	.503	.43	105.	668.	KEOWIN [4,7]
W-L	.503	.43	126.	630.	KEOWIN [4,7]
W-L	.688	.41	59.	660.	KEOWIN [4,7]
W-S	.688	.44	62.	925.	KEOWIN [4,7]
W-L	.688	.41	72.	615.	KEOWIN [4,7]
W-S	.688	.44	74.	895.	KEOWIN [4,7]
W-L	.688	.41	88.	547.	KEOWIN [4,7]
W-S	.688	.44	91.	910.	KEOWIN [4,7]
W-L	.688	.41	109.	510.	KEOWIN [4,7]
W-L	.850	.41	72.	558.	KEOWIN [4,7]
W-L	.850	.41	95.	470.	KEOWIN [4,7]
W-S	.315	.40	78.	509.	SOWA, ET AL. [6]
W-S	.315	.40	103.	352.	SOWA, ET AL. [6]
W-S	.315	.40	135.	272.	SOWA, ET AL. [6]
W-S	.315	.40	171.	178.	SOWA, ET AL. [6]
W-S	.315	.40	204.	178.	SOWA, ET AL. [6]
W-S	.315	.40	243.	134.	SOWA, ET AL. [6]
W-S	.315	.40	263.	150.	SOWA, ET AL. [6]
W-S	.715	.40	55.	909.	SOWA, ET AL. [6]
W-S	.715	.40	81.	815.	SOWA, ET AL. [6]
W-S	.715	.40	106.	853.	SOWA, ET AL. [6]
W-S	.715	.40	132.	855.	SOWA, ET AL. [6]
W-S	.715	.40	158.	725.	SOWA, ET AL. [6]
W-S	.715	.40	204.	624.	SOWA, ET AL. [6]
W-S	.715	.40	261.	542.	SOWA, ET AL. [6]
W-S	.356	.42	45.	452.	DHIR-CATTON [7]

W-S	.356	.42	38.	790.	DHIR-CATTON [7]
W-S	.356	.40	76.	196.	DHIR-CATTON [7]
W-S	.503	.45	51.	789.	DHIR-CATTON [7]
W-S	.503	.45	63.	390.	DHIR-CATTON [7]
W-S	.688	.41	38.	798.	DHIR-CATTON [7]
W-L	.688	.40	51.	503.	DHIR-CATTON [7]
W-S	.688	.42	51.	670.	DHIR-CATTON [7]
W-L	.688	.40	63.	472.	DHIR-CATTON [7]
W-S	.688	.40	63.	689.	DHIR-CATTON [7]
W-L	.688	.40	76.	448.	DHIR-CATTON [7]
W-S	.688	.41	76.	625.	DHIR-CATTON [7]
W-L	.688	.40	89.	517.	DHIR-CATTON [7]
W-S	.819	.39	35.	520.	DHIR-CATTON [7]
W-S	.819	.39	30.	860.	DHIR-CATTON [7]
W-S	.650	.40	76.	480.	SQUARER-PEOPLES [21,37]
W-S	.650	.40	100.	390.	SQUARER-PEOPLES [21,37]
W-S	.650	.40	135.	280.	SQUARER-PEOPLES [21,37]
W-S	.650	.40	192.	310.	SQUARER-PEOPLES [21,37]
W-S	.650	.40	76.	380.	SQUARER-PEOPLES [21,37]
W-S	.650	.40	100.	340.	SQUARER-PEOPLES [21,37]
W-S	.650	.40	128.	320.	SQUARER-PEOPLES [21,37]
W-S	.680	.40	30.	452.	TRENBERTH-STEVENS [24]
W-S	.680	.40	35.	292.	TRENBERTH-STEVENS [24]
W-S	.680	.40	40.	196.	TRENBERTH-STEVENS [24]
W-S	.680	.40	50.	166.	TRENBERTH-STEVENS [24]
W-S	.680	.40	60.	163.	TRENBERTH-STEVENS [24]
W-S	.680	.40	70.	194.	TRENBERTH-STEVENS [24]
W-S	.680	.40	80.	198.	TRENBERTH-STEVENS [24]
W-S	.680	.40	100.	168.	TRENBERTH-STEVENS [24]
W-S	.680	.40	140.	211.	TRENBERTH-STEVENS [24]
W-S	.680	.40	155.	213.	TRENBERTH-STEVENS [24]
W-S	.680	.40	185.	216.	TRENBERTH-STEVENS [24]
W-S	1.200	.40	30.	372.	TRENBERTH-STEVENS [24]
W-S	1.200	.40	40.	335.	TRENBERTH-STEVENS [24]
W-S	1.200	.40	50.	406.	TRENBERTH-STEVENS [24]
W-S	1.200	.40	60.	387.	TRENBERTH-STEVENS [24]
W-S	1.200	.40	70.	420.	TRENBERTH-STEVENS [24]
W-S	1.200	.40	80.	439.	TRENBERTH-STEVENS [24]
W-S	1.200	.40	103.	349.	TRENBERTH-STEVENS [24]
W-S	1.200	.40	125.	459.	TRENBERTH-STEVENS [24]
W-S	1.200	.40	143.	478.	TRENBERTH-STEVENS [24]
W-S	1.200	.40	195.	439.	TRENBERTH-STEVENS [24]
W-S	2.000	.40	20.	1287.	TRENBERTH-STEVENS [24]
W-S	2.000	.40	25.	586.	TRENBERTH-STEVENS [24]
W-S	2.000	.40	30.	930.	TRENBERTH-STEVENS [24]
W-S	2.000	.40	40.	895.	TRENBERTH-STEVENS [24]
W-S	2.000	.40	52.	853.	TRENBERTH-STEVENS [24]
W-S	2.000	.40	60.	669.	TRENBERTH-STEVENS [24]
W-S	2.000	.40	75.	611.	TRENBERTH-STEVENS [24]
W-S	2.000	.40	90.	474.	TRENBERTH-STEVENS [24]
W-S	2.000	.40	105.	561.	TRENBERTH-STEVENS [24]
W-S	2.000	.40	136.	617.	TRENBERTH-STEVENS [24]

W-S	2.000	.40	150.	561.	TRENBERTH-STEVENSON [24]
W-S	2.000	.40	190.	585.	TRENBERTH-STEVENSON [24]
W-C	.385	.388	260.	140.	GABOR-CASSULO [32]
W-C	.460	.393	300.	163.	GABOR-CASSULO [32]
W-C	.546	.403	300.	188.	GABOR-CASSULO [32]
W-C	.546	.379	450.	174.	GABOR-CASSULO [32]
W-S	.655	.383	300.	133.	GABOR-CASSULO [32]
W-S	.780	.407	300.	173.	GABOR-CASSULO [32]
W-S	.780	.387	400.	196.	GABOR-CASSULO [32]
W-C	.921	.393	250.	376.	GABOR-CASSULO [32]
W-C	1.095	.406	180.	303.	GABOR-CASSULO [32]
W-S	2.000	.386	60.	1040.	BARLEON-WERLE [33]
W-S	2.000	.386	80.	840.	BARLEON-WERLE [33]
W-S	3.000	.392	60.	1330.	BARLEON-WERLE [33]
W-S	3.000	.392	80.	1080.	BARLEON-WERLE [33]
W-S	4.760	.403	60.	1390.	BARLEON-WERLE [33]
W-S	4.760	.403	85.	1470.	BARLEON-WERLE [33]
W-S	7.940	.422	60.	2500.	BARLEON-WERLE [33]
W-S	7.940	.422	85.	2460.	BARLEON-WERLE [33]
W-S	10.000	.436	90.	3090.	BARLEON-WERLE [33]
W-S	15.880	.473	90.	4340.	BARLEON-WERLE [33]
W-S	.550	.40	127.	260.	SQUARER, ET AL. [37]
W-S	.550	.40	180.	250.	SQUARER, ET AL. [37]
W-S	.550	.40	230.	250.	SQUARER, ET AL. [37]
W-S	.550	.40	280.	250.	SQUARER, ET AL. [37]
W-S	2.840	.40	125.	1020.	SQUARER, ET AL. [37]
W-S	2.840	.40	180.	950.	SQUARER, ET AL. [37]
W-S	2.840	.40	230.	860.	SQUARER, ET AL. [37]
W-S	2.840	.40	288.	830.	SQUARER, ET AL. [37]
W-S	6.350	.40	180.	1390.	SQUARER, ET AL. [37]
W-S	6.350	.40	230.	1300.	SQUARER, ET AL. [37]
W-S	6.350	.40	280.	1420.	SQUARER, ET AL. [37]
W-S	1.588	.40	100.	730.	SOMERTON, ET AL. [44]
W-S	3.175	.40	50.	1250.	SOMERTON, ET AL. [44]
W-S	3.175	.40	100.	1300.	SOMERTON, ET AL. [44]
W-S	4.763	.40	100.	1900.	SOMERTON, ET AL. [44]
W-B	.258	.373	50.	273.	BARLEON-WERLE [52]
W-B	.258	.373	75.	196.	BARLEON-WERLE [52]
W-B	.258	.373	100.	117.	BARLEON-WERLE [52]
W-B	.258	.373	130.	150.	BARLEON-WERLE [52]
W-B	.450	.379	56.	345.	BARLEON-WERLE [52]
W-B	.450	.379	80.	226.	BARLEON-WERLE [52]
W-B	.450	.379	102.	183.	BARLEON-WERLE [52]
W-B	.605	.380	35.	568.	BARLEON-WERLE [52]
W-B	.605	.380	52.	503.	BARLEON-WERLE [52]
W-B	.605	.380	80.	258.	BARLEON-WERLE [52]
W-B	.605	.380	100.	268.	BARLEON-WERLE [52]
W-B	.855	.386	30.	686.	BARLEON-WERLE [52]
W-B	.855	.386	50.	643.	BARLEON-WERLE [52]
W-B	.855	.386	85.	373.	BARLEON-WERLE [52]
W-B	.855	.386	100.	313.	BARLEON-WERLE [52]
A-S	.356	.42	25.	74.	DHIR-CATTON [7]

A-S	.356	.42	18.7	231.	DHIR-CATTON [7]
A-S	.356	.42	15.	305.	DHIR-CATTON [7]
A-S	.356	.45	38.	65.	DHIR-CATTON [7]
A-S	.503	.44	19.	134.	DHIR-CATTON [7]
A-L	.503	.40	20.	83.	DHIR-CATTON [7]
A-S	.503	.40	25.	087.	DHIR-CATTON [7]
A-S	.503	.40	38.	112.	DHIR-CATTON [7]
A-S	.688	.39	13.3	262.	DHIR-CATTON [7]
A-S	.688	.39	16.8	173.	DHIR-CATTON [7]
A-S	.688	.39	19.	110.	DHIR-CATTON [7]
A-S	.688	.39	25.	109.	DHIR-CATTON [7]
A-S	.688	.40	32.	90.	DHIR-CATTON [7]
A-L	.848	.38	40.	104.	DHIR-CATTON [7]
A-L	.848	.38	20.	112.	DHIR-CATTON [7]
A-S	.688	.40	39.	82.	DHIR-CATTON [19]
A-S	.688	.40	49.	78.	DHIR-CATTON [19]
A-S	.688	.40	59.	85.	DHIR-CATTON [19]
A-S	.688	.40	70.	67.	DHIR-CATTON [19]
A-S	.900	.40	19.1	93.	DHIR-CATTON [19]
A-S	.900	.40	29.	128.	DHIR-CATTON [19]
A-S	.900	.40	35.	117.	DHIR-CATTON [19]
A-S	.900	.40	39.	92.	DHIR-CATTON [19]
A-S	.900	.40	59.	120.	DHIR-CATTON [19]
A-S	.900	.40	72.	118.	DHIR-CATTON [19]
A-S	.688	.40	84.	69.	DHIR-CATTON [28]
A-S	.688	.40	194.	100.	DHIR-CATTON [28]
A-S	.688	.40	400.	93.	DHIR-CATTON [28]
A-C	.385	.394	260.	52.	GABOR-CASSULO [32]
A-C	.460	.389	300.	63.	GABOR-CASSULO [32]
A-C	.546	.379	300.	87.	GABOR-CASSULO [32]
A-S	.655	.375	300.	76.	GABOR-CASSULO [32]
A-S	.780	.389	300.	95.	GABOR-CASSULO [32]
A-C	.921	.403	250.	126.	GABOR-CASSULO [32]
A-C	1.095	.406	180.	146.	GABOR-CASSULO [32]
A-S	1.588	.40	50.	157.	SOMERTON, ET AL. [44]
A-S	1.588	.40	75.	170.	SOMERTON, ET AL. [44]
A-S	1.588	.40	100.	140.	SOMERTON, ET AL. [44]
A-S	1.588	.40	150.	174.	SOMERTON, ET AL. [44]
A-S	1.588	.40	200.	208.	SOMERTON, ET AL. [44]
A-S	3.175	.40	50.	275.	SOMERTON, ET AL. [44]
A-S	3.175	.40	100.	275.	SOMERTON, ET AL. [44]
A-S	3.175	.40	150.	385.	SOMERTON, ET AL. [44]
A-S	3.175	.40	295.	325.	SOMERTON, ET AL. [44]
A-S	3.175	.40	400.	325.	SOMERTON, ET AL. [44]
A-S	4.763	.40	50.	271.	SOMERTON, ET AL. [44]
A-S	4.763	.40	100.	369.	SOMERTON, ET AL. [44]
A-S	4.763	.40	200.	285.	SOMERTON, ET AL. [44]
A-S	4.763	.40	300.	275.	SOMERTON, ET AL. [44]
A-S	4.763	.40	400.	325.	SOMERTON, ET AL. [44]
M-S	.356	.44	38.	45.	DHIR-CATTON [7]
M-S	.503	.44	25.	185.	DHIR-CATTON [7]
M-S	.503	.44	38.	196.	DHIR-CATTON [7]

M-S	.503	.43	51.	105.	DHIR-CATTON [7]
M-S	.688	.39	25.	85.	DHIR-CATTON [7]
M-L	.688	.40	25.	122.	DHIR-CATTON [7]
M-S	.688	.39	32.	105.	DHIR-CATTON [7]
M-S	.688	.39	38.	130.	DHIR-CATTON [7]
M-L	.688	.40	38.	71.	DHIR-CATTON [7]
M-L	.848	.38	50.	210.	DHIR-CATTON [7]
M-L	.848	.38	60.	164.	DHIR-CATTON [7]
M-L	.848	.38	70.	134.	DHIR-CATTON [7]
M-L	.848	.38	80.	185.	DHIR-CATTON [7]
M-C	.385	.398	260.	96.	GABOR-CASSULO [32]
M-C	.460	.395	300.	109.	GABOR-CASSULO [32]
M-C	.546	.407	300.	106.	GABOR-CASSULO [32]
M-S	.655	.380	300.	97.	GABOR-CASSULO [32]
M-S	.780	.385	300.	128.	GABOR-CASSULO [32]
M-C	.921	.403	250.	187.	GABOR-CASSULO [32]
M-C	1.095	.400	180.	197.	GABOR-CASSULO [32]
F-S	2.000	.40	20.	220.	BARLEON-WERLE [23]
F-S	2.000	.40	30.	220.	BARLEON-WERLE [23]
F-S	2.000	.40	40.	220.	BARLEON-WERLE [23]
F-S	2.000	.40	50.	190.	BARLEON-WERLE [23]
F-S	2.000	.40	60.	200.	BARLEON-WERLE [23]
F-S	3.000	.42	20.	390.	BARLEON-WERLE [23]
F-S	3.000	.42	30.	350.	BARLEON-WERLE [23]
F-S	3.000	.42	40.	310.	BARLEON-WERLE [23]
F-S	3.000	.42	50.	310.	BARLEON-WERLE [23]
F-S	3.000	.42	60.	290.	BARLEON-WERLE [23]
F-C	.385	.408	260.	43.	GABOR-CASSULO [32]
F-C	.460	.384	300.	58.	GABOR-CASSULO [32]
F-C	.546	.392	300.	68.	GABOR-CASSULO [32]
F-S	.655	.385	300.	48.	GABOR-CASSULO [32]
F-S	.780	.391	300.	78.	GABOR-CASSULO [32]
F-C	.921	.391	250.	84.	GABOR-CASSULO [32]
F-C	1.095	.406	180.	106.	GABOR-CASSULO [32]
F-S	2.000	.386	80.	240.	BARLEON-WERLE [33]
F-S	3.000	.392	80.	290.	BARLEON-WERLE [33]
F-S	4.760	.403	85.	390.	BARLEON-WERLE [33]
F-S	7.940	.422	85.	690.	BARLEON-WERLE [33]
F-S	10.000	.436	90.	740.	BARLEON-WERLE [33]
F-S	15.880	.473	90.	1080.	BARLEON-WERLE [33]
F-B	.258	.373	30.	48.	BARLEON-WERLE [52]
F-B	.258	.373	60.	24.	BARLEON-WERLE [52]
F-B	.258	.373	80.	18.	BARLEON-WERLE [52]
F-B	.258	.373	100.	16.	BARLEON-WERLE [52]
F-B	.258	.373	130.	16.	BARLEON-WERLE [52]
F-B	.450	.379	31.	56.	BARLEON-WERLE [52]
F-B	.450	.379	52.	46.	BARLEON-WERLE [52]
F-B	.450	.379	80.	42.	BARLEON-WERLE [52]
F-B	.450	.379	100.	37.	BARLEON-WERLE [52]
F-B	.605	.380	30.	110.	BARLEON-WERLE [52]
F-B	.605	.380	50.	44.	BARLEON-WERLE [52]
F-B	.605	.380	80.	57.	BARLEON-WERLE [52]

F-B	.605	.380	100.	50.	BARLEON-WERLE [52]
F-B	.855	.386	35.	83.	BARLEON-WERLE [52]
F-B	.855	.386	55.	84.	BARLEON-WERLE [52]
F-B	.855	.386	80.	66.	BARLEON-WERLE [52]
F-B	.855	.386	102.	73.	BARLEON-WERLE [52]
I-C	.385	.382	260.	70.	GABOR-CASSULO [32]
I-C	.460	.395	300.	65.	GABOR-CASSULO [32]
I-C	.546	.406	300.	81.	GABOR-CASSULO [32]
I-S	.655	.379	300.	77.	GABOR-CASSULO [32]
I-S	.780	.400	300.	89.	GABOR-CASSULO [32]
I-C	.921	.389	250.	142.	GABOR-CASSULO [32]
I-C	1.095	.400	180.	116.	GABOR-CASSULO [32]
S-U	.325	.536	98.	953.	GABOR, ET AL. [3]
S-U	.325	.526	114.	640.	GABOR, ET AL. [3]
S-U	.325	.515	129.	505.	GABOR, ET AL. [3]
S-U	.325	.508	134.	322.	GABOR, ET AL. [3]
S-U	.325	.499	150.	205.	GABOR, ET AL. [3]
S-U	.325	.484	170.	153.	GABOR, ET AL. [3]

DISTRIBUTION:

US NRC Distribution Contractor (CDSI) (300 copies)
7300 Pearl Street
Bethesda, MD 20014
275 for R7
25 for NTIS

Division of Reactor Safety Research (35)
Office of Nuclear Regulatory Research
U.S. Nuclear Regulatory Commission
Washington, DC 20555
Attn: C. N. Kelber
M. Silberberg
R. W. Wright (30)
G. Marino
N. Zuber

Joint Research Center (4)
Ispra Establishment
21020 Ispra (Varese)
Italy
Attn: R. Klersy
H. Holtbecker
D. Schwalm
K. Mehr

Power Reactor & Nuclear Fuel (5)
Development Corporation (PNC)
Fast Breeder Reactor Development Project (FBR)
9-13, 1-Chome, Akasaka
Minato-Ku, Tokyo
Japan
Attn: Dr. Mochizuki
Dr. Watanabe (2)
Dr. H. Nakamura
M. Saito

Monsieur A. Schmitt
IPSN/DSN
CEN Fontenay-aux-Roses
B. P. 6
92260 Fontenay-aux-Roses
France

DISTRIBUTION: (Cont'd.)

Safety Studies Laboratory/DSN (5)
Commissariat a L'Energie Atomique
Centre d'Etudes Nucleaires de Cadarache
B. P. 1, 13115 Saint-Paul-lez-Durance
Bouches-Du-Rhone
France

Attn: M. Schwarz
M. Bailly
M. Meyer Heine
M. Penet
N. Kayser
C. LeRigoleur

Centre d'Etudes Nucleaires de Grenoble (2)
B. P. 85-Centre de Tri
38401 Grenoble Cedex
France

Attn: M. Costa/STT
D. Rousseau/Pi-SEDTI

UKAEA (4)
Safety and Reliability Directorate
Wigshaw Lane
Culcheth
Warrington, WA3 4NE
England

Attn: M. Hayns
R. S. Peckover
B. D. Turland
K. A. Moore

Atomic Energy Establishment (5)
Winfrith, Dorchester
Dorset
United Kingdom

Attn: R. V. Macbeth
R. Potter
G. L. Shires
G. F. Stevens
R. Trenberth

DISTRIBUTION: (Cont'd.)

Culham Laboratory (1)
Culham
Abingdon
Oxfordshire OX14 3DB
England
Attn: F. Briscoe

Kernforschungszentrum Karlsruhe (7)
D-75 Karlsruhe
Postfach 3640
West Germany
Attn: G. Heusener (PSB)
P. Hoffmann (PSB)
H. Werle (INR)
L. Barleon (IRB)
G. Hoffman (IRM)
K. Thomauske (IRB)
U. Muller (IRM)

University of California (4)
Energy and Kinetics Department
Rm. 5405 Bolter Hall
Los Angeles, CA 90024
Attn: I. Catton (2)
V. K. Dhir (2)

Argonne National Laboratory (5)
Reactor Analysis and Safety Division
9700 South Cass Avenue
Argonne, IL 60439
Attn: L. Baker, Jr.
J. C. Cassulo
J. D. Gabor
R. D. Pedersen
E. S. Sowa

Westinghouse Electric Corp. (1)
Power Systems
P.O. Box 355
Pittsburgh, PA 15230
Attn: L. Hochreiter

DISTRIBUTION: (Cont'd.)

Westinghouse Research and Development (1)
Center
Pittsburgh, PA 15235
Attn: A. Pieczynski

Westinghouse Hanford Co.
337 Bldg., 300 Area
P.O. Box 1970
Richland, WA 99352
Attn: G. R. Armstrong

Nuclear Safety Analysis Center (2)
3412 Hillview Avenue
P.O. Box 10412
Palo Alto, CA 94303
Attn: D. Squarev
Garry Thomas

CRBRP Project Office
P.O. Box U
Oak Ridge, TN 37380
Attn: H. B. Piper

Fauske and Associates (2)
631 Executive Dr.
Willowbrook, IL 60521
Attn: M. Epstein
R. Henry

Brookhaven National Laboratory (3)
Fast Reactor Safety
Upton, Long Island, NY 11973
Attn: J. W. Yang
T. Ginsberg (2)

Los Alamos National Laboratory
Q7, Slot K556
Los Alamos, NM
Attn: Javier Escamilla

DISTRIBUTION: (Cont'd.)

NUS Corporation
Consulting Division
4 Research Place
Rockville, MD 20850
Attn: Juan M. Nieto

EG&G, Idaho (5)
P.O. Box 1625
Idaho Falls, ID 83415
Attn: C. Allison
T. M. Howe
T. S. Hsieh
R. J. Lloyd
R. W. Miller
B. J. Buescher

Mass. Inst. of Tech. (2)
Mech. Eng. Dept.
Cambridge, MA 02139
Attn: P. Griffith
M. Kazimi

University of New Mexico
Nuclear Engineering Department
Albuquerque, NM
Attn: M. El-Genk

University of Wisconsin (2)
Department of Nuclear Engineering
Madison, Wisconsin 53706
Attn: M. Corradini
S. Abdel-Khalik

Purdue University
Department of Nuclear Engineering
West Lafayette, IN 47907
Attn: T. Theofanous

DISTRIBUTION: (Cont'd.)

1537 T. Y. Chu
9000 A. Narath
9400 A. W. Snyder
9410 D. J. McCloskey
9420 J. V. Walker (5)
9420 M. Lohr
9421 T. P. Schmidt (3)
9421 G. Fieg
9421 J. E. Gronager
9421 J. T. Hitchcock
9421 P. A. Kuenstler
9421 H. Meister
9421 G. W. Mitchell
9421 C. A. Ottinger
9421 J. B. Rivard
9421 K. Takahashi
9422 D. A. Powers
9422 J. D. Fish
9422 A. P. Taig
9422 W. Tarbell
9423 P. S. Pickard
9424 M. J. Clauser
9424 K. D. Bergeron
9424 F. W. Sciacca
9424 M. E. Senglaub
9425 W. J. Camp
9425 E. D. Bergeron
9425 W. M. Breitung
9425 P. Herter
9425 J. E. Kelly
9425 R. J. Lipinski (15)
9425 M. Pilch
9425 A. Suo-Anttila
9425 A. J. Wickett
9425 M. F. Young
9426 G. L. Cano
9440 D. A. Dahlgren
9441 M. Berman
9443 L. Bonzon
9451 K. P. Boldt
7511 A. W. Reed
7512 R. H. Nilson
3141 T. L. Werner (5)
3151 W. L. Garner (3)
For DOE/TIC (Unlimited Release)
3154-3 R. P. Campbell (25)
(for NRC distribution to NTIS)

120555078877 1 ANR7
US NRC
ADM DIV OF TIDC
POLICY & PUBLICATIONS MGT BR
PDR NUREG COPY
LA 212
WASHINGTON DC 20555

Org.	Bldg.	Name	Rec'd by	Org.	Bldg.	Name	Rec'd by